University of Leoben, Austria
Los Alamos National Laboratory, USA

Characterisation of ion irradiated ferritic/martensitic materials for nuclear application

Diploma thesis

by

Christiane Vieh

This work was performed, in part, at the Los Alamos National Laboratory in New Mexico and at the Department of Materials Physics of the University of Leoben.

Leoben, 2010

Eidesstattliche Erklärung

Ich erkläre an Eides statt, dass ich diese Arbeit selbständig verfasst, andere als die angegebenen Quellen und Hilfsmittel nicht benutzt und mich auch sonst keiner unerlaubten Hilfsmittel bedient habe.

Affidavit

I declare in lieu of oath, that I wrote this thesis and performed the associated research myself, unsing only literature cited in this volume.

Leoben, June 2010 Christiane Vieh

Acknowledgement

This research is supported by the Global Nuclear Energy Partnership (GNEP), the Los Alamos National Laboratory (LANL), USA and the Montanuniversität Leoben, Austria and my thanks are going in particular to A.o. Univ. Prof Dr. Reinhard Pippan from the Department of Materials Physics by allowing and extensive student exchange.

Special thanks to Dr. Stuart A. Maloy and Dipl. Ing. Dr. mont. Peter Hosemann for many interesting discussions and for their guidance.

For their technical support I would like to thank R. M. Dickerson, P. O. Dickerson, R. J. McCabe, D. D. Byler, J. A. Valdez, R. R. Greco, W. K. Pierce, R. F. Rockage and D. J. Williams.

This work was performed, in part, at the Center for Integrated Nanotechnologies (CINT), an US Department of Energy, Office of Basic Energy Sciences user facility. Los Alamos National Laboratory, an affirmative action equal opportunity employer, is operated by Los Alamos National Security (LLC), for the National Nuclear Security Administration of the US Department of Energy under contract DE-AC52-06NA25396.

Finally, I am very grateful to my family and friends for their support through all steps of this work.

Kurzfassung

Charakterisierung von ferritisch/martensitischen Stählen nach der Bestrahlung mit niedrig energetischen Ionen für den Einsatz im nuklearen Bereich

Für leistungsfähigere Reaktoren werden von Konstrukteuren höhere Betriebstemperaturen gefordert, wobei ein Werkstoff neben der hohen Temperatur auch der vorherrschenden Strahlung standhalten muss. Die Bestrahlung mit niedrig energetischen H oder He Ionen kann dazu verwendet werden eine Schädigung in Werkstoffen zu erzeugen, die mit der Werkstoffschädigung in Reaktoren und Spallationsquellen verglichen werden kann. Dabei wird nur ein sehr geringes Probenvolumen bestrahlt, das Material wird nicht aktiviert und es ermöglicht sowohl eine schnelle als auch kostengünstige Evaluierung von Werkstoffen.

In dieser Arbeit wurden zwei konventionelle Materialien (HT-9 im ferritischen und martensitischen Zustand) und zwei moderne Materialien (ODS-Legierungen: MA956 und MA957) unter verschiedenen Bedingungen bestrahlt und anschliessend mit Hilfe von Rasterkraftmikroskopie, Transmissionselektronenmikroskopie und Nanohärte analysiert.

Nach der Bestrahlung mit Helium bei Raumtemperatur, mit Protonen bei Raumtemperatur, 300°C und 550°C konnte bei den konventionellen Materialien eindeutig eine Änderung der Härte festgestellt werden während bei den modernen Materialen keine Änderung der Härte ermittelt werden konnte. Bei HT-9 im martensitischen Zustand wurde eine geringere Härtesteigerung festgetellt als beim HT-9 im ferritischen Zustand. Da Grenzflächen den durch Strahlung erzeugten Defekten als Rekombinationsstellen dienen, ist die geringer Härtesteigerung in der martensitischen Mikrostruktur auf eine wesentlich höhere Grenzflächendichte zurückzuführen.

Die bisher ermittelten Ergebnisse der modernen Materialien lassen auf eine ausgezeichnete Strahlungsresistenz schliessen, da selbst bei erhöhten Temperaturen keine Härtesteigerung festgestellt werden konnte. Es müssen jedoch erst neuartige Produktions- und Verarbeitungstechniken für diese ODS-Legierungen entwickelt werden, um einen zukünftigen Einsatz gewährleisten zu können.

Abstract

Characterization of ion irradiated ferritic/martensitic materials for nuclear application

In order to increase the efficiency of a next generation reactor, designers require higher reactor operation temperatures and higher fuel burn-up which leads to a higher dose on the material. Ion beam accelerator experiments using low ion energy, have the advantage of allowing relatively fast and inexpensive irradiations of materials without activating the sample but do not irradiate a large sample volume. In order to mimic reactor and spallation source environment on materials typical ions used are helium and hydrogen.
In this study, four different ferritic/martensitic steels (conventional materials e.g HT-9 with different micro structures) and Oxide Dispersion Strengthened (ODS) alloys (advanced materials: MA956 and MA957) were exposed to an ion beam and irradiated at different conditions. After ion irradiation these materials were characterized in detail using Atomic Force Microscopy, nanoindentation and Transmission Electron Microscopy.
The implantation with Helium at RT, the irradiation with protons at RT, 300 °C and 550°C showed a clear change in hardness due to the ion irradiation for the conventional materials but did not show any change in hardness for the advanced materials. An important result of the present study is that a clear difference can be seen in the HT-9 ferritic and tempered martensitic material. It appears that the fine tempered martensitic microstructure has a significant smaller effect in irradiation hardening. Therefore it should be a more radiation tolerant material. This can be explained by the fact that the martensitic microstructure has a high density of interfaces which act as recombination sites for radiation induced defects.
The advanced materials did not show an increase in nanohardness compared to the conventional materials under any of those conditions. Therefore, a need to develop techniques to produce these ODS alloys with conventional steel processing technologies as the previous results indicate superior radiation resistance at elevated temperature, exists.

Contents

1 Background and motivation of the diploma thesis

Renaissance of nuclear energy?

The challenges for the world's future will be to achieve a reduction of greenhouse gases like CO_2 while ensuring the availability of energy at the same time. In 2030, the International Energy Agency (IEA) expects an increase of CO_2 to around 42 billion tones per year instead of today's 27 billion tones, led by China with 11 billion tones and in long term we would face a rise in temperatures up to 6 degrees [1]. A nuclear power plant allows producing energy while emitting nearly no CO_2 to the atmosphere during operation. The greenhouse gas emission of a nuclear power plant is comparable with renewable energies such as wind, solar and hydro as shown in Fig. 1.

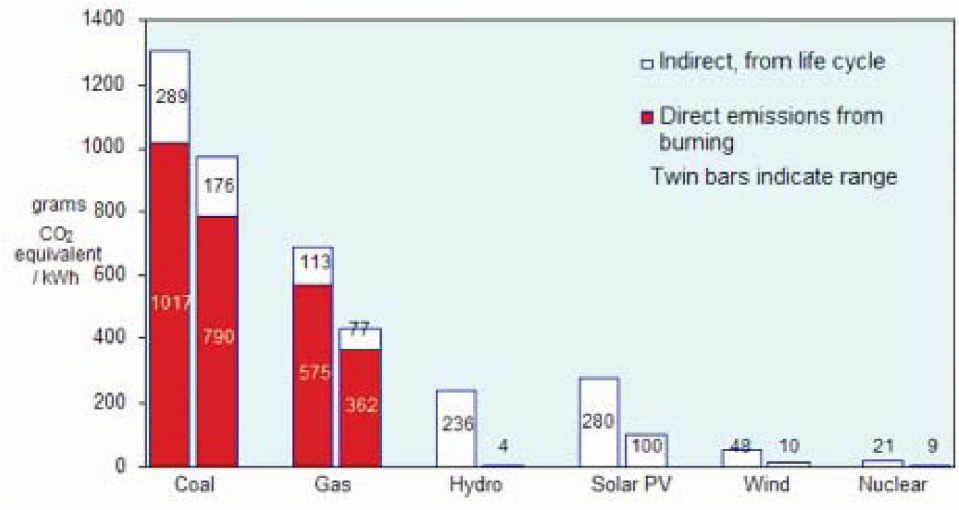

Fig. 1: Illustration of the greenhouse gas emission from electricity production [2].

Currently 443 nuclear power plants are operating worldwide supplying 16 % of the electricity consumed worldwide [3]. Additional 24 nuclear power plants to ensure a reliable energy supply are under construction mostly in China, India, Russia, Ukraine, Finland, Korea and Japan [3]. It appears that the growing demand of energy will be satisfied with a renaissance of nuclear power. While Nuclear power can provide the energy needed, it also has other problems attached including the production of toxic and radioactive waste and their unsolved disposal problem. Overall, nuclear power is not considered the perfect solution for a cleaner environment, but it is the only ready to use non CO_2 producing, large scale electricity producing alternative.

Fuel cycle options

Currently most countries do not have long-term storage capabilities for securely storing their nuclear waste. Therefore, new nuclear concepts need to be developed and applied. Fig. 2 shows the possible fuel cycle options. Every fuel cycle starts with mining and

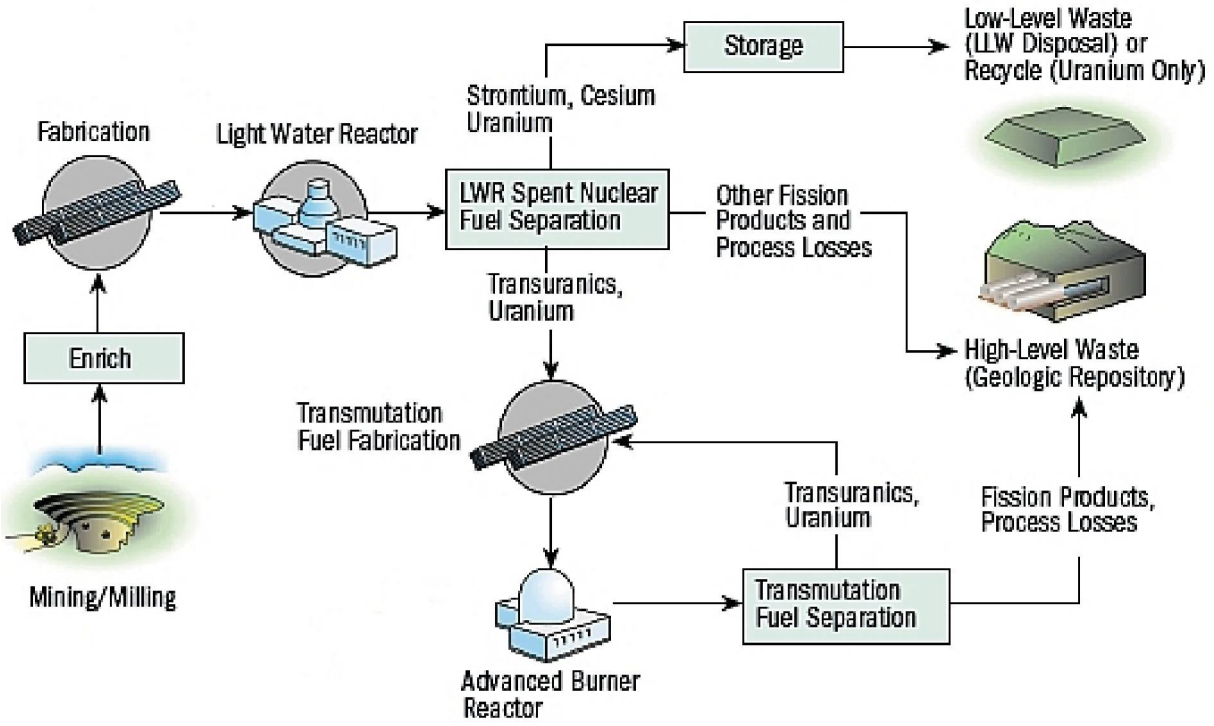

Fig. 2: Depiction of the proposed GNEP fuel cycle, showing the use of the Advanced Burner Reactor in consuming light water reactor waste and playing a major role in reducing the burden of long-term storage [4].

milling of uranium ore which contains the three uranium isotopes as found in nature (0.7 % of uranium-235, 99.3 % of uranium-238 |3|). An isotope of an element is an atom which has the same number of protons but a different number of neutrons. Their chemical properties are identically but the different isotopes have different mass numbers because the total number of nucleons is different. For example the element 92 is uranium (92 protons in its nucleus) and has several isotopes U-235 for example has 92 protons and 143 neutron reaching 235 nucleons. The raw uranium ore is refined into what is called "yellow cake" the uranium oxide (U_3O_8) |5|. The yellow cake is then converted into uranium hexafluoride gas (UF_6). The UF_6 can now be used to enrich the U-235 to about 3-5 % using either centrifuges or diffusion cascades |3|. The so enriched Uranium is then fabricated into uranium oxide (UO_2)fuel pellets |5|. The pellets are filled into long tubes (fuel rods) which, typically made of zircalloy (zirconium based metal). Hundred of these fuel rods are bundled together in a fuel assembly which is then installed in a nuclear

reactor. In a typical pressure water reactor (PWR) a fuel assembly will be replaced every 18 months [5]. The spend fuel is only partially consumed, it contains a high content of uranium and transuranic elements and waste fission products.
There are two main strategies to dispose used fuel:

- 1. "open fuel cycle": In the "throw away", "once through,", or "open fuel cycle" the spend fuel will be stored in a deep geological repository until it is decayed below the natural uranium radio toxicity level [6]. This takes in general from a few million to a few billion years. This is currently the most widely used approached (including the U.S.).

- 2. "closed fuel cycle": In the "closed fuel cycle", the spend fuel is recycled into new fuel used for fast reactors allowing to reuse most of the fissionable material [6].

To go from an open fuel cycle to a closed fuel cycle, a fast reactor is needed in order to transmute transuranics into more stable isotopes. Transuranics are those elements with a higher atomic number than uranium (neptunium (93), plutonium (94), americium (95), and curium (96)) [7]. These elements containing more energy (per mass), are long-lived, more toxic and could potentially also be used in nuclear weapons. Remaining U-235 may be used again in thermal reactors and the transuranics can be used in fast reactors or advanced burner reactors. Current reactor designs use zirconium alloys as fuel cladding as zirconium has a lower neutron absorption cross section than iron the main alloying component in steel. The neutron absorption cross section is a measure of the ability of a nucleus to absorb neutrons. Fast reactors however, accumulate high dose in a much shorter period of time. Therefore new materials are needed to withstand this harsh environment of higher dose, higher dose rate, higher temperature and corrosive environment. Therefore zirconium alloys are not feasible because of their low creep strength and high corrosion rate, which leads to the choice of various steel alloys (conventional and advanced materials).
The aim of this thesis is to compare and evaluate irradiation damage in advanced materials for nuclear application. For this purpose the response of ODS alloys and conventional materials were evaluated using ion beam irradiation at various temperature.

2 Introduction and literature review

2.1 Radiation effects in materials

Depending on the material, temperature, energy and type of irradiation various radiation effects can have a large impact on the integrity of structural parts in nuclear reactor or spallation source environments. Types of concern are mainly alpha, neutron and proton radiation. Effects of beta- and gamma- radiation as well as X-ray radiation especially in nuclear environments are relatively small compared to radiation of alpha-, neutron- or proton particles. In this chapter, the effects causing by radiation are described in the following.

2.1.1 Spallation and transmutation

Spallation is the removal of particles, when a high energy proton is accelerated and hits a target, which is made of a heavy metal like tungsten (W) or lead (Pb) as shown in Fig. 3. When a high energetic proton hits the target, the atoms of this material capture the hitting particles as well as their high energy. Then the atomic nuclei is starting to oscillate and will be disruptor. The knocked-out particles or fragments are including a number of neutrons, protons and some alpha particles. Some of these fragments are fast enough to cause further spallation so that for every proton that hits a nucleus, 20 to 30 neutrons are ejected in the end [8].

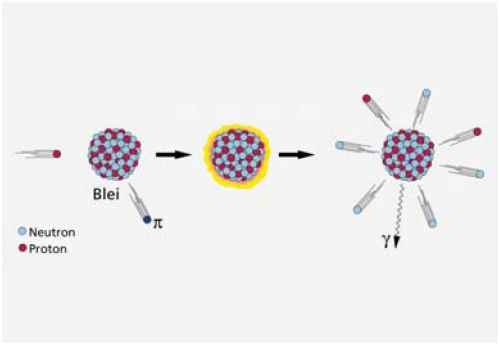

Fig. 3: Principle of spallation:a lead atom is hit by an incoming proton [9].

The spallation process can be compared to nuclear fission but spallation needs more energy than it delivers, and therefore no chain reaction takes place. In a nuclear reactor, neutrons are always needed to keep the chain reaction going. The neutron- spectrum emitted by spallation is similar to a fission spectrum as in a thermal reactor, so a moderator like water can be used to slow down the neutrons to thermal energy to obtain a neutron

source and apply it through surrounding beam lines to various materials and interfaces. Transmutation is the conversion of one isotope to another. Thereby the structure, composition, chemical properties and nuclear properties are changed |7|. It occurs through various forms of nuclear reactions. These reactions can be generated from natural interstellar radiation sources, normal decay of unstable isotopes, or synthetic production of new isotopes by irradiation of stable and unstable isotopes using high energy accelerators. These possible transmutation reactions are for example:

- Beta plus/minus ($\beta^{+/-}$)- decay
  - In β^{+}- decay [5, 7], energy is used to convert a proton into a neutron because of repulsive Coulomb forces between the protons in the nucleus it will lead to this conversion to a new stable nucleus.

    $$energy + p^{+} \rightarrow n + \beta^{+} + v \tag{1}$$

    Where p is a proton, β^{+} is a positive electron or positron and v is a neutrino.
  - In β^{-}- decay [7], a neutron converts into a proton while emitting an electron (β^{-}) and an antineutrino because of a too low mass for the nuclear charge. For example:

    $$n \rightarrow p + \beta^{-} + v^{'} \tag{2}$$

    Where p is a proton, β- is an electron and v' is an antineutrino.
  - Alpha (α)- decay In α- decay [5, 7], a nucleus emits an alpha particle (α) identical to a helium nucleus (^{4}He) and decays into an atom a mass number 4 less and an atomic number 2 less as shown in the following reaction of the isotope uranium 238 into thorium 234.

    $$^{238}U \rightarrow {}^{234}Th + {}^{4}He^{2+} \; or \; {}^{238}U \rightarrow {}^{234}Th + \alpha \tag{3}$$

    The generated nucleus itself is not stable and decays further. ^{238}U decays in 14 steps to become the stable isotope lead 206 (^{206}Pb). This kind of reaction is a form of radioactive decay.

  During α- or β- decay the nucleus is emitting gamma (γ) radiation as well.

- Spontaneous fission Spontaneous fission |7| follows the same process as nuclear fission, except that it occurs without the atom having been struck by a neutron or other particle. It is only energetically possible for atomic masses above 230 so it is a form of radioactive decay characteristic of very heavy isotopes.

Transmutation can be used to destroy long-term hazardous elements such as transuranic elements while creating energy. Therefore the total amounts of mass of the products are less than the mass of the original atom and the missing mass has been changed into energy. In a nuclear reactor transmutation is causing neutron capture and/or fission by neutron bombardment. As the experiments presented here are performed in an ion accelerator the primary event caused by protons is discussed. In steel a very common transmutation from one element to another after hit by a high energetic proton is the β^+- decay of iron (^{56}Fe):

$$^{56}Fe + p^+ \rightarrow {}^{56}Co + n \tag{4}$$

The so produced ^{56}Co isotope is radioactive and its half live is 77.3 days while emitting β- and γ- radiation during its decay back to ^{56}Fe [10]. The nuclear cross section, the amount of isotopes produced by an incoming particle in the unit barns which is defined as being 10^{-28} m^2, and corresponds approximately to the cross sectional area of a uranium nucleus [7]. At a proton energy range of 10-15 MeV a relatively high cross sectional area occurs for steels in accelerators for this important nuclear reaction. To prevent major activation of steel, it is important to know the cross sections and reactions for all major alloying elements, therefore low-activating elements as composition parts in steel are preferred for nuclear applications. These low-activating elements are: Fe, Cr, V, Ti, W, C. That indicates that the typical steel alloying elements Mo, Nb, Ni, Cu and N must be eliminated or minimized to obtain reduced activation [11]. It is known that high Si contents will have a negative effect on its mechanical properties under irradiation (lower ductility) and will not be used in nuclear facilities where the material would be exposed to high radiation. Also a high Ni content in reactor steel can activate the steel as it can cause the building of radioactive isotopes like ^{55}Fe, ^{59}Ni or ^{58}Co and others at higher energy, therefore only a low amount of Ni is alloyed [11].

2.1.2 Structural defects and swelling

A type of crystal where every single atom is in the correct position, a so called "perfect" crystal, does not exist. Defects can be divided into the following classes:

Point defects

These are lattice locations where an atom is missing or is in an irregular place in the crystal lattice structure. Point defects [12] include self interstitial atoms, substitutional atoms, interstitial impurity atoms and vacancies (see Fig. 4):

- A self interstitial atom is an extra atom located in between regular lattice sites in the crystal structure. In general self interstitial occur only in low concentrations in metals because they destroy and stress the lattice structure.

- A substitutional atom is a different element than the matrix atoms, which has replaced one of the matirx atoms in the lattice. These impurity atoms are usually close in size to the bulk atom.

- Interstitial impurity atoms are much smaller than the atoms in the bulk matrix so they fit into the open space between the bulk atoms of the lattice structure (e.g. carbon atoms in iron). Interstitial diffusion occurs mainly at elevated temperature because the interstitial impurity atoms must overcome the bond energy due to nearby atoms.

- Vacancies are empty spaces in the crystal lattice where an atom is missing. At elevated temperature the vacancy density is increased. Diffusion of atoms occurs mainly because of motion of the bulk or substitutional atoms to vacancy sites or interstitial impurities to different interstitial positions.

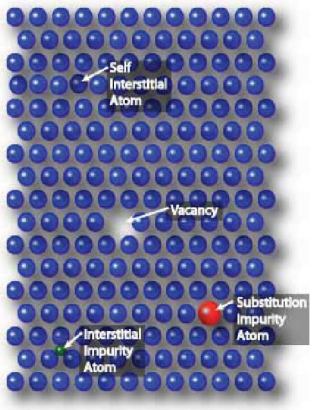

Fig. 4: The image shows the different point defects which can take place in crystals [12]

Linear defects

Commonly they are called dislocations. There are two basic types of dislocations, the edge dislocation and the screw dislocation. Plastic deformation in a material occurs in most cases due to the movement of dislocations and their movement produces additional dislocations. When dislocations cross each other it hinders their movement. This increases the force needed to move the dislocation and result in strengthen of the material [12].

- An edge dislocation is illustrated in Fig. 5(a) and can be explained as an extra half-plane of atoms inserted in a lattice.

- A screw dislocation is visualized in Fig. 5(b) as a block of metal with a shear stress applied across one end so that the metal begins to rip.

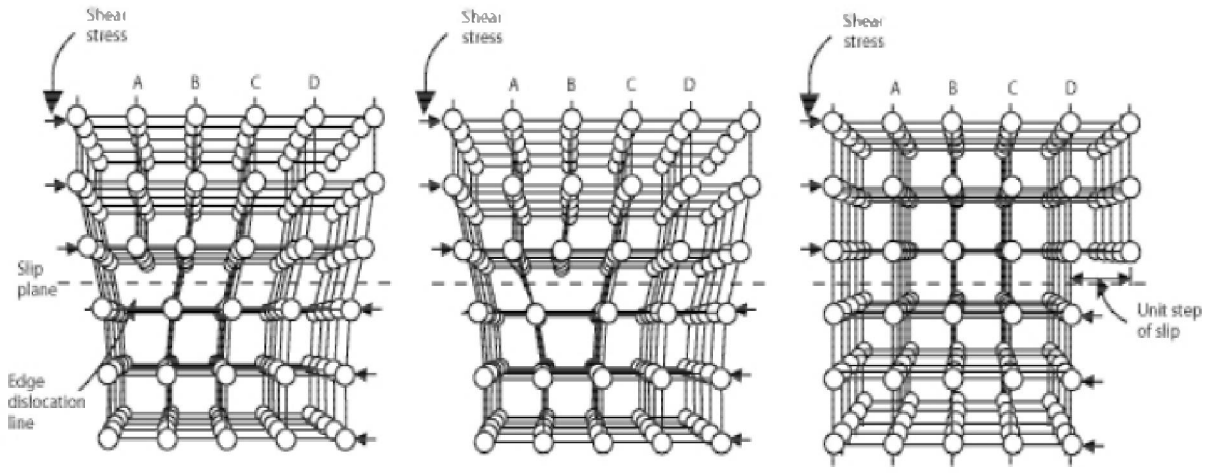

(a)

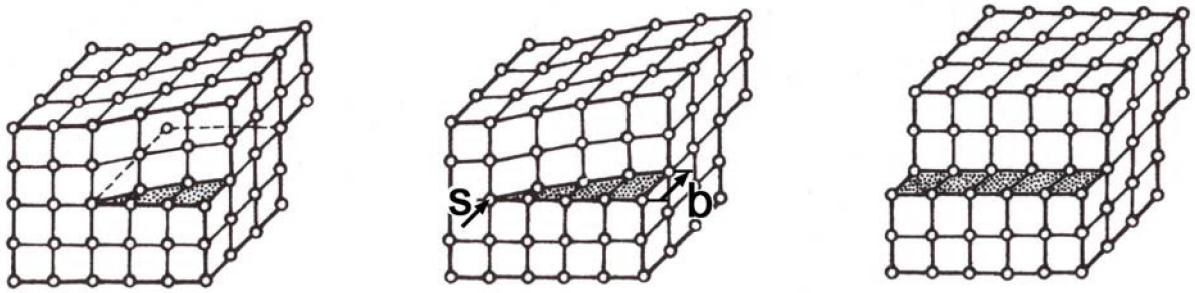

(b)

Fig. 5: A shear stress is applied to the dislocation shown in (a), atomic bonds break and reform to allow the dislocation to move through the crystal [13].Image (b) shows a srew dislocation moving through the crystal [14].

Planar defect

Planar defects [12] include grain boundaries, stacking faults and external surfaces but only grain boundaries will be explained a little bit more as the other planar defects have an inferior relevance to this work. Grain boundaries are known as the boundary surface area where one grain stops and another begins. They are limiting the lengths and motions of dislocations. Having smaller grains results in more grain boundaries what strengthens a material. Grains can range in size from nanometers to millimeters across and their orientations are usually rotated with respect to the neighbor grains. The size of the grains can be controlled by the cooling rate when the material cast or heat treated. Rapid cooling produces smaller grains whereas slow cooling result in larger grains.

3 dimensional defects

Three dimensional defects [12] are primarily closed phase boundaries which are a surface where two samples of matter with different properties are in contact like gas bubbles in

water for example. But this type of defect is of inferior relevance to this work as well, so they are listed to complete the overview of crystal defects.

Radiation induced crystal defects

An incoming ion or high energy radiation cause knock on ions in the material by displace lattice atoms. The knock on atom itself becomes a projectile in the solid, and can cause further collision events. The collision of two atoms can cause the atom to be displaced to interstitial sites while leaving a vacancy at its original position. A pair of a vacancy and an interstitial is often called a Frenkel pair [12]. Depending on irradiation temperature and /or cascade properties (ion energy, ion species) the interstitial and vacancies can recombine so the lattice is in its original shape. Some of the created defects can also migrate and form vacancy clusters (voids), or dislocation loops. In steels, loops form below 400- 450 °C [15]. Loop size increases and loop number density decreases with increasing irradiation temperature. The amount of crystallographic damage can become so large to completely amorphize the surface of the target that it can become a glass. The progressive change in microstructure with irradiation dose and temperature induce the agglomeration of vacancies and interstitials into voids and dislocation loops that cause swelling.

Swelling

Swelling [15] is a phenomenon induced through intense radiation and results in an increase of volume of the material as shown in Fig. 6. It occurs when vacancies collect into cluster or voids which grow and cause the material to expand. Materials show significant differences in their swelling resistance behavior. Swelling generally occurs between 30 and 50% of the absolute melting point. Face centered cubic (FCC) materials are more vulnerable to

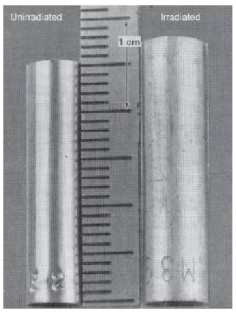

Fig. 6: Shows swelling of 316L stainless steel rods, before (left) and after (right) irradiation in the EBR-11 reactor [16].

swelling than a body centered cubic (BCC) material because the FCC crystal structure is closer packed. Together with the resulting strength reduction and embrittlement, it is a major concern for materials for nuclear applications.

Displacement per atom (dpa)

The unit which radiation damage in material is measured is displacement per atom (dpa) [17]. Dpa is the number of times that an atom in the material is initially displaced by the incoming ion for a given fluence. For example, 10 dpa means each atom in the material has been displaced from its site within the structural lattice of the material an average of 10 times (due to interactions between the atoms and the energetic ions irradiating the material). It considers only the initiated displaced atoms and not the recombination mechanism.

2.1.3 Strengthening mechanism

As discussed in section 2.1.2 the ability of a crystalline material to plastically deform depends on the ability for dislocation to move within a material. Restrickting the movement of dislocations will result in a strengthening of the material. There are a number of ways also called hardening mechanism [12] to avoid dislocation movement:

- Controlling the grain size: Within a material the size of a grain has an effect on the strength of the material. The boundary between grains acts as a barrier for dislocations to move and the resulting slip because adjacent grains have different orientations. The smaller the grains the shorter the distance atoms can move along a slip plane. Therefore, smaller grains improve the strength of a material.

- Strain hardening: also called work-hardening or cold-working is the process of making a metal harder and stronger through plastic deformation. When a metal is plastically deformed, dislocations move and additional dislocations are generated. The more dislocations within a material, the more they will interact and become pinned or tangled. This will result in a decrease in the mobility of the dislocations and a strengthening of the material. This type of strengthening is called cold-working because the plastic deformation must occur at a temperature low enough that atoms cannot rearrange themselves. When a metal is deformed at higher temperatures it is then called hot-working and the dislocations can rearrange and little strengthening is achieved.

- Alloying: introducing point defects and more grains to pin dislocation.

- Creating point defects through irradiation for example: Cascades produce point defects that form dislocation loops [39]. They can unify with the existing dislocation network.

2.2 Investigated materials

The thermal efficiency of a nuclear reactor correlates with the temperature, as higher as better the efficiency. The temperature window of use of structural materials is mainly limited by their structural integrity under irradiation and activation. Candidate structural materials have a chemical composition that is based on low-activating elements: Fe, Cr, V, Ti, W, C to prevent major activation of the material. Since Ni, Co and Si cannot be used as explained in more detail in the previous pages the main candidate materials for use in radioactive environments are ferritic/ martensitic (F/M) materials. Based on these issues, the selected materials for this study are roughly divided into two groups, conventional and advanced materials and their chemical composition are listed in Table 1 [18].

Table 1: Nominal composition of the tested materials in wt%

Material	Fe	C	Cr	Mo	Ni	Mn	Al	Si	others/remarks
HT-9*	bal.	0.20	12.1	1.04	0.51	0.57	-	0.17	2 different heats
MA956	bal.	0.019	19.1	-	0.19	0.09	4.2	-	Y_2O_3:0.48, Ti:0.34
MA957	bal.	0.01	13.8	0.26	-	-	-	-	Y_2O_3:0.26, Ti:0.90

*HT-9 ferritic tempered to HT-9 martensitic

2.2.1 Conventional materials

HT-9 ferritic and HT-9 tempered martensitic

HT-9 ferritic steel was developed in Europe in the 1960s primarily for the nuclear industry. Because of the large amount of information generated on HT-9 for the Clinch River Breeder Reactor (CRBR) project in the US during the 1970s, it was the first choice of material for applications for the US program on next-generation reactors [19]. Similar steels to HT-9 with maximum operating temperature in conventional fossil-fired power plants of 550 °C were chosen in Europe and Japan: EM-12, FV448, DIN 1.4914, and JFMS were chosen in France, United Kingdom, Germany, and Japan [19]. For comparison purposes in this thesis, HT-9 will be used as representative of these steels. HT-9 is a type of F/M stainless steel (12Cr-1MoVW) with a superior resistance to irradiation damage, compared to austenitic stainless steels. It shows low activation, low swelling, high resistance to Helium- bubble formation and adequate mechanical properties like low embrittlement at elevated temperatures. To achieve a change in grain size of HT-9 ferritic to evaluate the micro structural changes after irradiation of a ferritic to tempered martensitic HT-9 steel, a 1 mm hot rolled sheet of HT-9 ferritic was normalized and tempered

(1060 ℃ in Argon for 1 hour, then an air quench, followed by 730 ℃ for 2 hours and a final air quench) to obtain a HT-9 tempered martensitic structure. The microstructure of the HT-9 ferritic steel and HT-9 tempered martensitic steel are shown in Fig. 7. Both images are taken at Mag 1000 x with an optical microscope (OM) (Olympus DP50) after etching with a V2A solution for about 30 seconds. In Fig. 7 the ferrite matrix (a) is shown which appears mostly white but also black and grey depending on the orientation whereas the carbides are small black and white dots they are distributed in the ferrite matrix and mainly located at the grain boundaries. In Fig. 8 are images of the investigated materials shown at Mag 3000 x taken with a Gemini scanning electron microscopy (SEM) with an InLens detector at a target voltage of 15 kV.

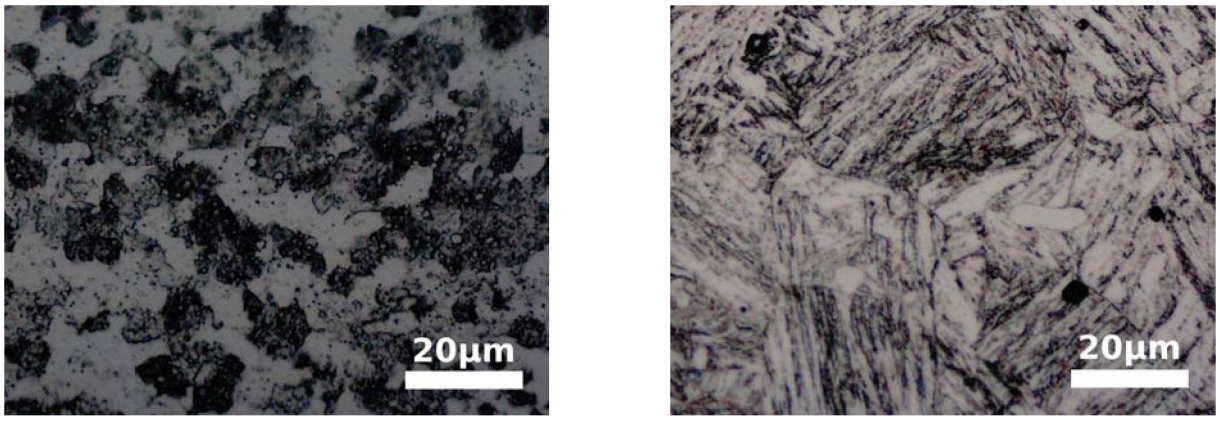

(a) (b)

Fig. 7: The OM image in (a) shows the microstructure of the pre-irradiated HT-9 ferritic steel at Mag 1000 x,and (b) shows and overview of the martensite structure of HT-9 after the tempering process.

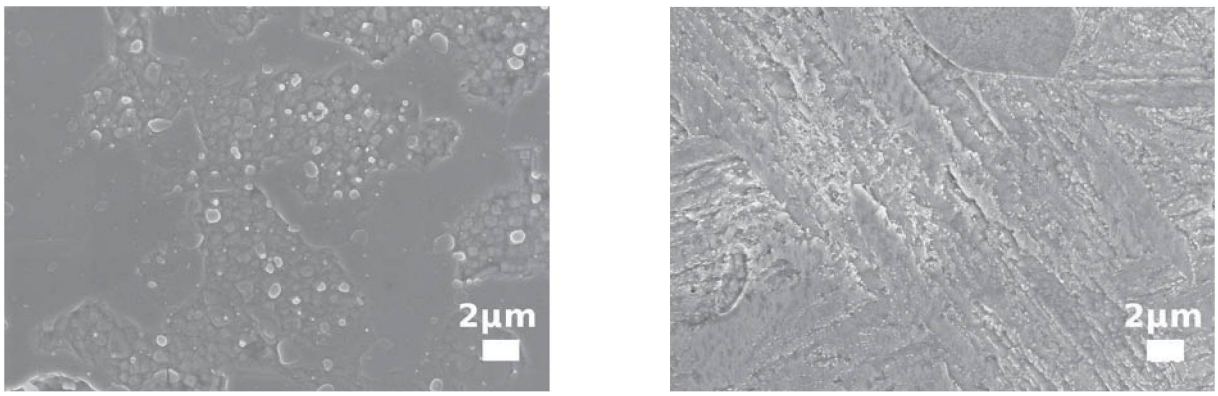

(a) (b)

Fig. 8: (a) shows a SEM image of the pre-irradiated HT-9 ferritic taken at Mag 3000 x. The SEM image in (b) illustrates the pre-irradiated HT-9 tempered martensitic structure which is taken at Mag 3000 x.

2.2.2 Advanced materials

Oxide dispersed strengthened (ODS) alloys (MA956, MA957)

ODS steels, which are strengthened by small oxide particles, are produced by complicated and expensive mechanical alloying, powder metallurgy techniques (milling, pressing, sintering and extrusion) instead of conventional processing techniques. The mechanical alloying (MA) process was invented in the middle of the 1960s by John S. Benjamin at the Paul D. Merica Research Laboratory (PDMRL) [20]. The initial attempt was to develop a material by combining oxide dispersion strengthening with gamma prime precipitation hardening in a nickel- based superalloy for gas turbine applications. It is an alternative technique for producing metallic and ceramic powder particles in the solid state and provides a means to overcome the drawback of formation of new alloys using a starting mixture of low and high melting temperature elements. Iron based ODS alloys such as MA956 an MA957, have a composition and microstructure to allow creep and oxidation resistance in components operating at elevated temperatures($T = 0,9T_{\text{melting}}$)as these homogenously distributed, incoherent nano-dispersoids act as thermodynamically stable obstacles to dislocation movement [21, 22]. The microstructure of those ODS alloys are shown in Fig. 9 taken at Mag 1000 x with an optical microscope (Olympus DP50) after etching with a V2A solution for about 30 seconds. In Fig. 10 SEM images of both ODS alloys are shown taken at Mag 3000 x. Their creep resistance is achieved from a combination of factors including the dispersion of these small oxide particles 20-50 nm in diameter, primarily Yttrium oxide (Y_2O_3) particles [23].

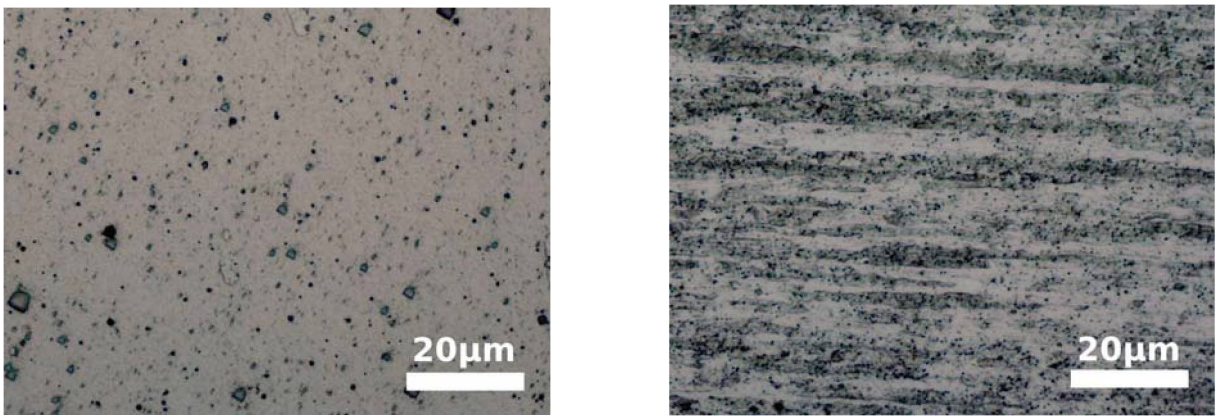

(a) (b)

Fig. 9: The OM image in (a) shows the microstructure of the pre-irradiated MA956 at Mag 1000 x,and (b) shows and overview of the pre-irradiated MA956 structure taken at Mag 1000 x.

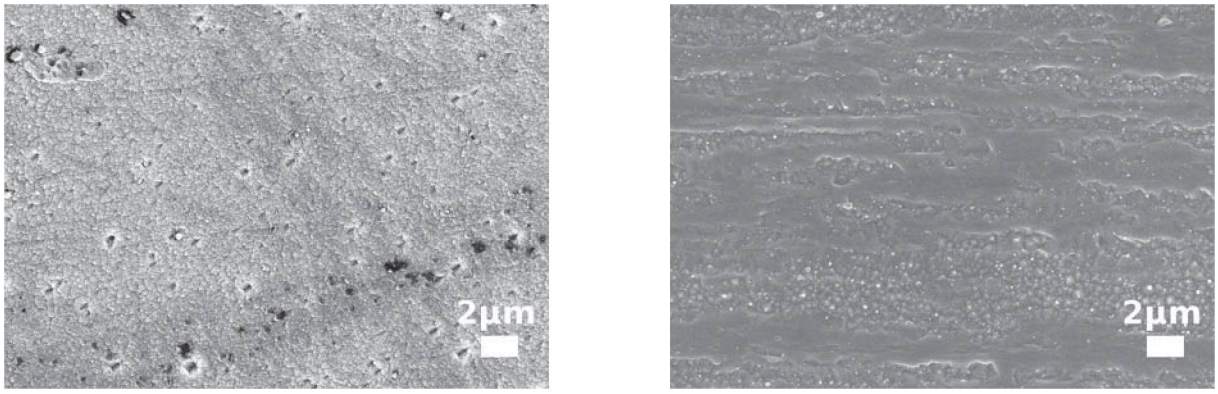

(a) (b)

Fig. 10: (a) shows a SEM image of the pre-irradiated MA956 taken at Mag 3000 x. The SEM image in (b),taken at Mag 3000 x illustrates the pre-irradiated structure of MA957.

A drawback of ODS steels are their anisotropy in mechanical properties caused by the processing, low ductility at room temperature, difficult machining and virtually no welding ability. Therefore, a need exists to develop techniques to produce these ODS alloys with conventional steel processing techniques. Although these steels are still in the development stage the preliminary results indicate superior radiation resistance at elevated temperature. For increased efficiency of a next generation reactor, designers require higher operating temperatures. ODS materials for structure application would allow increasing the operating temperature to approximately 650 °C [21].

3 Experimental

Specimen preparation for the implantation/irradiation

All four main candidate materials (HT-9 ferritic, HT-9 tempered martensitic, MA956 and MA967) were prepared for the irradiation and pre irradiation studies the same way:

- Firstly, cut the samples with a diamond metal bonded low speed cutting saw in pieces of around 5 mm x 10 mm x 3 mm from the bulk material.
- Secondly, fixate the so cut samples using a low melting point mounting wax(crystal bound) on a steel bloc and grinde with a 180, 320, 600, 800, 1200 and 2400 grit on both sides to a thickness of around 1-2 mm.
- Thirdly, polishing on both sides with a polishing cloth and a 6 μm diamond paste and end with a 1 μm polishing suspension.

Calculation of parameters for the irradiation with SRIM 2006

In material science research, ion beams are used to modify samples by injecting ions to change the phyisical properties of the target for example a change in chemical and electronic properties. The ion beam also causes damage to solid targets by atom displacement. The incoming ion hits a target atom(Primary knock on PKA) and transfers parts of its kinetic energy. This process knocks the target atom from its original lattice site and causes further knock on atoms. The ion species determines the dimension of the cascades produced [15]. The dose unit for this type of defect is measured in dpa (displacement per atom) and is calculated with Monte Carlo methods for example SRIM (The Stopping and Range of Ions in Matter) [17]. Necessary information to perform a calculation with SRIM 2006 are:

- the composition(stoichiometry) of the target material
- the displacement energy of each element in each layer for every material
- the density of each layer of material
- the incident ion type and energy
- the beam current

The composition of the target material and the kinetic energy of the incident ions determine the depth of penetration of the ions in the target. The incident ions are produced in an ion source(eg.:source of negative ions by Cesium sputtering SNICS) and these ions

are extracted out of the source and accelerated to a high energy. The amount of ions implanted can be determined by measuring the beam current (in Ampere or Coulomb/sec) the charge state and the time the sample is exposed to the beam.

$$I = \rho \; A = C/s \tag{5}$$

where I is the beam current,
ρ is the sample density and
A is the area of the sample.
The SRIM code allows to calculate the vacancies produced per incoming ion in a detailed calculation with full damage cascades as shown in Fig. 3. From the vacancy file gained from the SRIM calculation the total vacancies from all element types has to be added which leads to the equation:

$$D = \frac{vacancies}{ions * Angstrom} \tag{6}$$

where D is the damage rate to the sample from SRIM calculation.

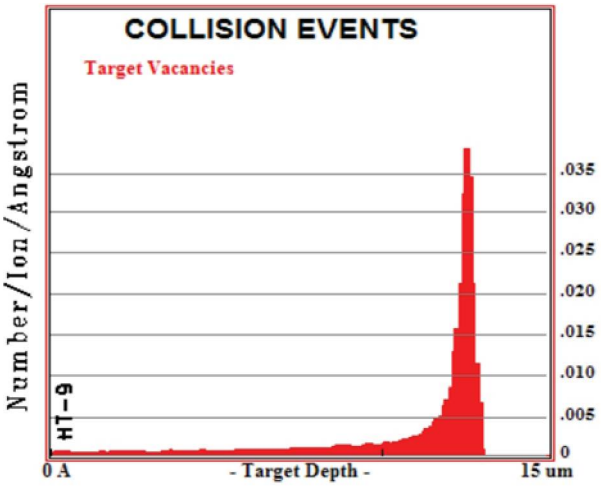

Fig. 11: Calculated 3.5 MeV helium damage profile (generated vacancies/ion and thickness(Angstrom)) using SRIM code by producing a relatively uniform damage profile over the first 10 μm of the helium's full range at 12 μm.

The $\mathrm{dpa_{rate}}$ calculated by

$$dpa_{\mathrm{rate}} = \frac{D\phi}{N} \tag{7}$$

where ϕ is the fluence

$$\phi = \frac{ions}{q * A} \tag{8}$$

q is the ion charge.
N is the defect number density

$$N = \frac{\rho \; A}{M} \tag{9}$$

and M is the mass number of the sample which leads to the total dose in dpa.

$$dpa_{\text{total}} = \frac{dpa_{\text{rate}} * total\ vacancies}{N}. \tag{10}$$

For this study the following parameters for the implantation/irradiation were defined by calculating a certain dose with SRIM and listed in Table 2. As shown in Table 2 the

Table 2: Irradiation experiments test matrix

Material	Ion [C/s]	Energy [keV]	Current [nA]	Dose [dpa]	Depth [μm]	Temperature [°C]	Area [mm^2]	Time [hours]
Conventional	H^+	750	2000	1-1.5	~ 6	RT, 300, 550	1x1	25-30
materials	He^+	3500	150	3	~ 6	RT	2x2	36
Advanced	H^+	750	2000	1-1.5	~ 6	RT, 300, 550	1x1	25-30
materials	He^+	3500	150	3	~ 6	RT	2x2	36

helium implantation was performed at a beam energy of 3500 keV and at a current of 150 nA to produce a near-uniform helium distribution from the surface 6 μm deep into the material to reach a dose of 3 dpa at room temperature in 36 hours. For the proton irradiation at room temperature an irradiation time of 30 hours was necessary to reach a dose of 1.5 dpa at a beam energy of 600 keV and a current of 2 μA. The high temperature experiments at 300 and 550 °C were performed at a higher beam current of 750 keV at the same current of 2 μA to induce a damage in an area of 1 by 1 mm on each sample corner and a uniform hydrogen distribution from the surface 6 μm into the material in 25 hours.

3.1 Helium implantation and proton irradiation

The radiation experiments were performed at the Ion Beam Material Laboratory (IBML) at the Los Alamos National Laboratory (LANL) using a tandem accelerator with a 6 MV terminal voltage allowing to accelerate a 6 MeV proton (H^+) beam and/or a 12 MeV Helium (He^+) beam [24]. This beam can be used to induce radiation effects in the candidate materials. The laboratory's core is a 3.2 MV tandem ion accelerator and a 200 kV ion implanter together with several beam lines as shown in Fig. 12. For all implantation or irradiation experiments the size of the sample(HT-9 ferritic, HT-9 tempered martensitic, MA956 and MA957) was 5 mm x 10 mm x 2 mm. Always four samples, from each material one piece, were irradiated simultaneously and the irradiated area on the samples was 1 mm x 1 mm and located on each sample corner which were covered by the beam during

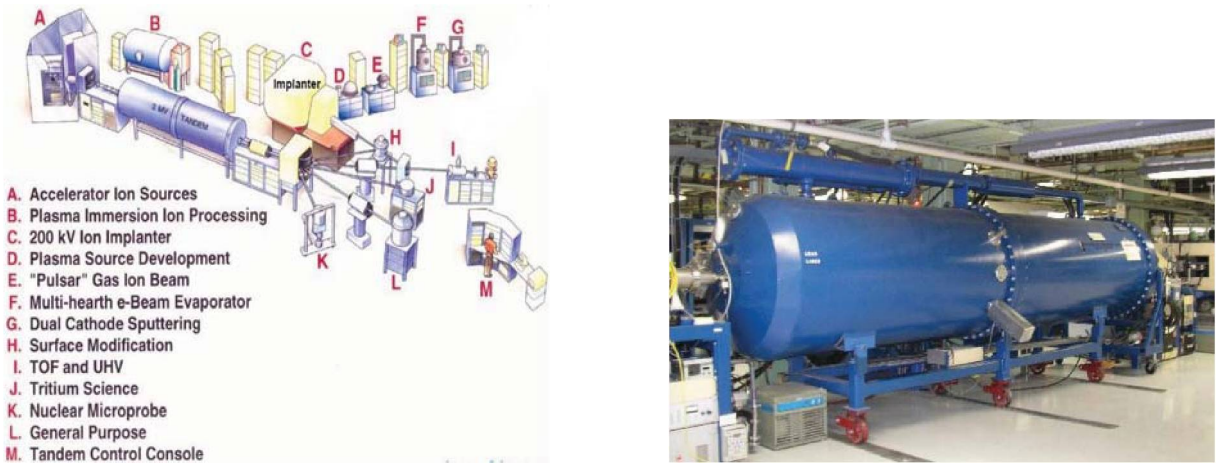

(a) (b)

Fig. 12: (a)Ion Beam Material Laboratory with a tandem ion accelerator, an ion implanter and several beam lines attached [24]. (b)Image of the tandem ion accelerator at the IBML [24].

the implantation/irradiation experiment.

3.1.1 The room temperature experiments

Helium implantation

The Helium implantation at room temperature was performed by using an air cooled copper sample holder with a diameter of 20 cm and 10 mm in thickness on which the samples were mounted on the copper block by using silver paste and carbon tape to ensure good adhesion and thermal conductivity at the same time.

The temperature was measured with a thermocouple which was located underneath the samples. On top of the four samples two scintillators were mounted with a carbon tape 2 mm appart from each other to localize and adjust the beam. During the room temperature experiments the beam current was monitored continuously by measuring the current induced on the samples.

Proton irradiation

Fig. 13(a) shows the sample holder for the proton irradiation at room temperature with a diameter of 8 cm and 10 mm in thickness on which the samples were mounted on the steel block by using silver paste and carbon tape to ensure good adhesion and thermal conductivity at the same time. The chamber where the irradiation took place is shown in Fig. 13(b),Fig. 14(a) and (b).

(a) (b)

Fig. 13: (a)Illustrate the sample holder used for the room temperature experiment with four samples in a rectangular wiring. (b)Shows the chamber of the beam line for the room temperature experiment.

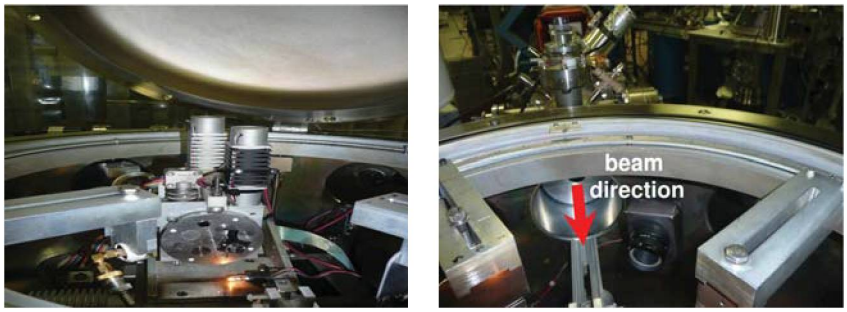

(a) (b)

Fig. 14: (a)Sample holder adjusted in the chamber for the room temperature experiment. (b)The arrow mark the direction of the beam within the chamber.

The temperature was measured with a thermocouple which was located underneath the samples. On top of the four samples two scintillators were mounted with a carbon tape 2 mm appart from each other to localize and adjust the beam. During the room temperature experiments the beam current was monitored continuously by measuring the current induced on the samples on the sample holder.

3.1.2 The high temperature experiments

Proton irradiation at 300 °C and 550 °C

Fig. 15 (a) shows the boron nitride(BN) heating stage. It has a highest capable temperature of 1500 °C in vacuum. The samples were arranged and fixed in a sample holder Fig. 16(a) and clamped with boron nitride scews on the heating stage to keep it in place. On top of the sample holder two scintillators were clamped with boron nitride screws 2 mm appart from each other for the beam adjustment Fig. 16(b). During the setup of the heating stage an insulating problem occured because the electrical resistivity of

(a) (b)

Fig. 15: (a)The boron nitride heating stage which was used for the high temperature experiments. (b)Shows the samples arranged and fixed in a sample holder like a sandwich.

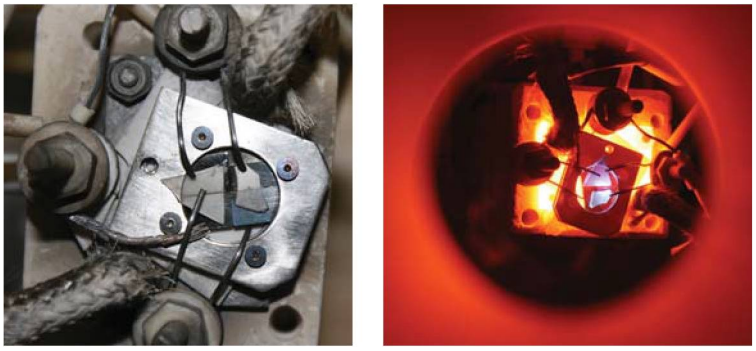

(a) (b)

Fig. 16: (a)Boron nitride heating stage used for the high temperature experiments. (b)Image of the beam during the irradiation.

the insulator (BN) decreased with increasing temperature and did not allow to measure continously the beam current. In the absence of a grounding connection it is the leackage current that could flow from any conductive part or the surface of non-conductive parts to the ground if a conductive path is available therefor a piece of Al_2O_3 a seperate layer of insulation was used to reduce the insulation problem but it was not possible to completely overcome this problem. Thus the beam current was measured every hour within 5 seconds by turning off the power of the heating stage to minimize the drop in temperature $\leqslant 5$ °C. Both high temperature irradiation experiments took around 25 hours to ensure a dose of 1 dpa by an average beam current of 750 nA.

3.2 Characterisation techniques

3.2.1 Nanoindentation

After irradiation the samples were mounted in an tilting angle of 10-20 ° towards the surface, as shown in Fig. 17, in epoxy cold mount to increase the analysing area by a factor

of 2-3 what will lead to an increase of hardness vs. depth resolution |25|.. The mounted

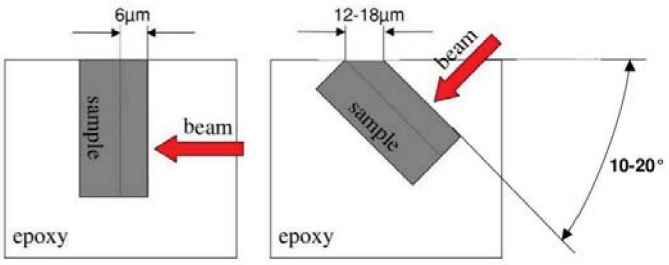

Fig. 17: left:Shows the sample regularly mounted in epoxy. right:The sample mounted in an tilt angle to increase the area [25].

sample has to be polished with a 1200, 2400 and 4000 grit to remove the corner of the sample(see Fig. 17 right). Afterwards polished with a 0.1 μm colloidal silica on a Buehler vibromet polisher to ensure a flat and smooth surface as required for nanoindentation.
The nanoindentation measurements were performed at LANL using a Hysitron Tribo indenter equipped with a multi-range nanoprobe, an optical microscope, and an AFM. A Berkovich diamond indenter tip was used to perform the nanoindentation measurements |25|. The basic idea of nanoindentation is based on the macro hardness measurements where a rigid body is driven into a material to form an imprint. The ratio between maximum load and projected contact area of the indenter and the sample material leads to a value called hardness with the dimension of a pressure. For macro hardness the imprint is measured by optical methods, for nanoindentation a depth sensing technique is applied to determine the contact area. Beside the load, the displacement of the indenter is recorded during the test thus measurments gives the load-displacement curves which are used to calculate the contact area at maximum load based on the procedure proposed by Oliver, Pharr |26| where hardness H is defined as

$$H = \frac{P}{A(h_c)} \tag{11}$$

where P is the indentation load and A is the projected area of the contact between the indenter and the specimen as a function of the contact depth (h_c) |27|.
The indentation was performed on the edge with an array of 10-14 rows with 8-10 indents in each row as shown in Fig. 18 taken by an optical microscope at 1000x after the indentation. Each row of indents was parallel to the edge and the indents itself were placed 4 μm apart from each other and resulting in an array of over 100 indents for each specimen condition. Before and after performing the array of indents an regular AFM, using a silicon tip in contact mode, was used to ensure the location of the indents.

To ensure constant indentation depth the system was operated in displacement mode

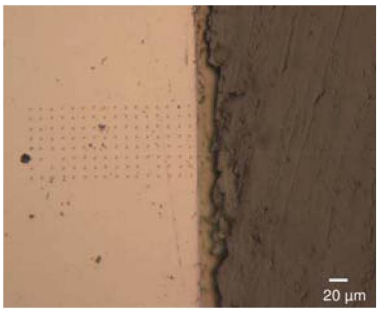

Fig. 18: An optical microscope image(Mag 1000x) shows the position where the nano indentation was performed.

for all indents as well as to eliminate the influence of the indentation size effect [28] which shows higher hardness as the indents gets smaller within one array of indents. The displacement was set at 200 nm, the loading rate was 10 nm/sec, the holding time was 10 seconds, and the unloading rate was 10 nm/sec [25]. To compare the results from the nanohardness measurments with micro hardness data the indentation depth vs. hardness curves for the unirradiated materials were obtained by using a high load Hysitron indentation head which allows a maximum force of 2 N. A Berkovich indenter tip was used to perform indents up to a depth of 3 μm in an unirradiated area of the sample. 7 different indentation depths (200 nm, 300 nm, 450 nm, 675 nm, 1500 nm, 2250 nm, and 3000 nm) and 7 indents of each depth were performed [25]. The resultant curve (hardness vs. depth) was then used with the Nix and Gao [28] model in order to extrapolate the nano hardness data to micro hardness

3.2.2 Atomic Force Microscopy (AFM)

An AFM, measures the force between the surface of a sample and a very sharp tip mounted on a cantilever. The cantilever with the mounted tip is scanning across the topography of the surface by a piezoelectric motor as it is illustrated in Fig. 19. Thereby the tip interacts with the surface and causes a deflection of the cantilever what is sensed by a laser beam which is reflected and detected by a photodiode [29–31]. The detected signal is converted into a z(x,y) information. Therefore the topography of the sufrace can be obtained by determining the force as a function of the sample position. The detection is made optically by beam deflection. With AFM conducting and insulating materials can be analyzed. On the irradiated samples mounted in an angle of 10-20 ° towards the surface AFM characterization of the structure was performed at LANL using a Park Scientific Autoprobe M5. The tip used was a commercial silicon contact mode cantilever and tip. The scan rate was generally 0.7 Hz for a 40 μm x 40 μm scan area and adjusted to a lower frequency ($\leq$ 0.7 Hz) for images at a higher magnification.

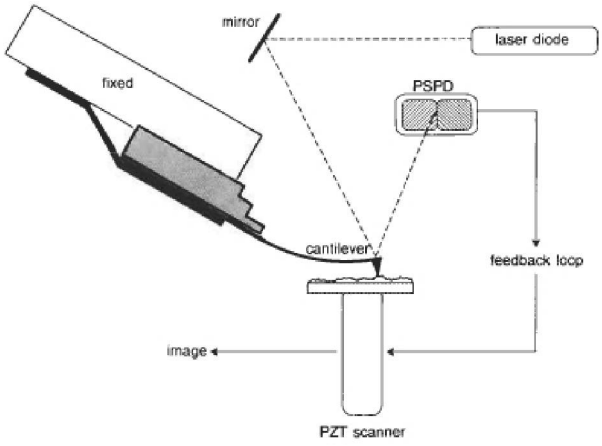

Fig. 19: Shows the principle layout of an AFM [32].

3.2.3 Transmission Electron Microscopy (TEM)

Specimen preparation for TEM

To determine the changes through irradiation of the irradiated samples pre- irradiated TEM foils had to be prepered by using a preperation technique were no damage similar to ion implantation or irradiation occures. Therfore samples with a size 10 by 10 mm and about 350 μm in thickness were cut with a diamond metal bonded low speed cutting saw from the precast material and mechanically thinned with a 1200, 2400 and 4000 grit to a thickness of around 150 μm on both sides. From these thin plates, discs of 3 mm in diameter were punched out with a press after removing the flash by using the 4000 grit on both sides again.

There are different methods of specimen preparation for TEM, two of them are used and described for this thesis:

- 1.Electro polishing: The former thinned discs were electro-polished in a twin-jet electronic device under different conditions listed in Table 3 to obtain a thin part in the specimen that the light is running through.

- 2.Focused ion beam (FIB) milling: As the area after irradiation of each sample is only 1 mm by 1 mm and the irradiation goes about 6 μm deep into the material, a conventional technique as described in point 1 is not applicable. By using a gallium (Ga^+) ion beam of an accelerating voltage of 10 keV a thin foil was milled out of the irradiated area of the samples and welded on a copper holder to provide a good handling for furter observation in TEM. During FIB milling, the thin foils receive additional irradiation and gallium ion deposition within the subsurface layers. In several studies |33–36| the damage induced by FIB processing has been evaluated and found that the thickness of the subsurface layer (3-20 nm) linearly increases

with an increase in FIB acceleration voltage from 5 to 30 keV |33|. Furthermore it depends on the material and device geometry. As the irradiation experiments causes a severe damage in a larger area of the material than subsurfaces changes caused by FIB processing this preperation technique was used for the irradiated samples.

Table 3: Electro polish conditions for the investigated materials

Material	Electrolyte solution	Voltage |V|	Ampere |mA|	Temperature |°C|	Time |sec.|
Conventional materials	10 % ($HClO_4$) 90 % (CH_3CH_2OH)	24	85	RT	100-150
Advanced materials	20 % (H_2SO_4) 80 % (CH_3CH_2OH)	22.5	45-50	-20 and RT	100-150

TEM operation

A Philips CM30 instrument located at LANL was used to perform TEM characterisation on either conventional(electro polished) prepared samples as well as on FIB-foils. This instrument is equipped with a LaB_6 filament and allows sample tilt up to $\pm$ 45 °. The acceleration voltage used was 300 kV. The wavelength, λ, of a 100 keV electron is for example 0.0037 nm and for an 300 keV electron even smaller (0.00197 nm), much smaller than that of light, Xrays, or neutrons used in other analytical techniques |37|. In TEM an electron beam is emitted from an electron gun and focused by several magnetic lenses at and below the sample as shown in Fig. 20. The gun emits highly monoenergetic electrons of an exceedingly small wavelength which penetrate the thin (less than 200 μm) sample and obtaine a signal from undeflected and deflected electrons. The signal goes to a detector usually a fluorescent screen. For obtaining images a film plate(camera box) or a video camera is attached. The CM30 instrument used at LANL was equipped with a camera box loaded with 36 film plates. After each session the film plates were scanned with a scanning device and transfered into a digital format for further analysis.
A typical microscope session starts with the following basic steps |38|.

- Load the sample in the sample holder, it is important not to touch the holder with the bare hands in order to ensure a short pumping time.
- Insert the holder into the column. Thereby the specimen holder is first partially inserted in a position in an airlock mechanism until a pumpdown time is required before the specimen holder can be fully inserted into the column.

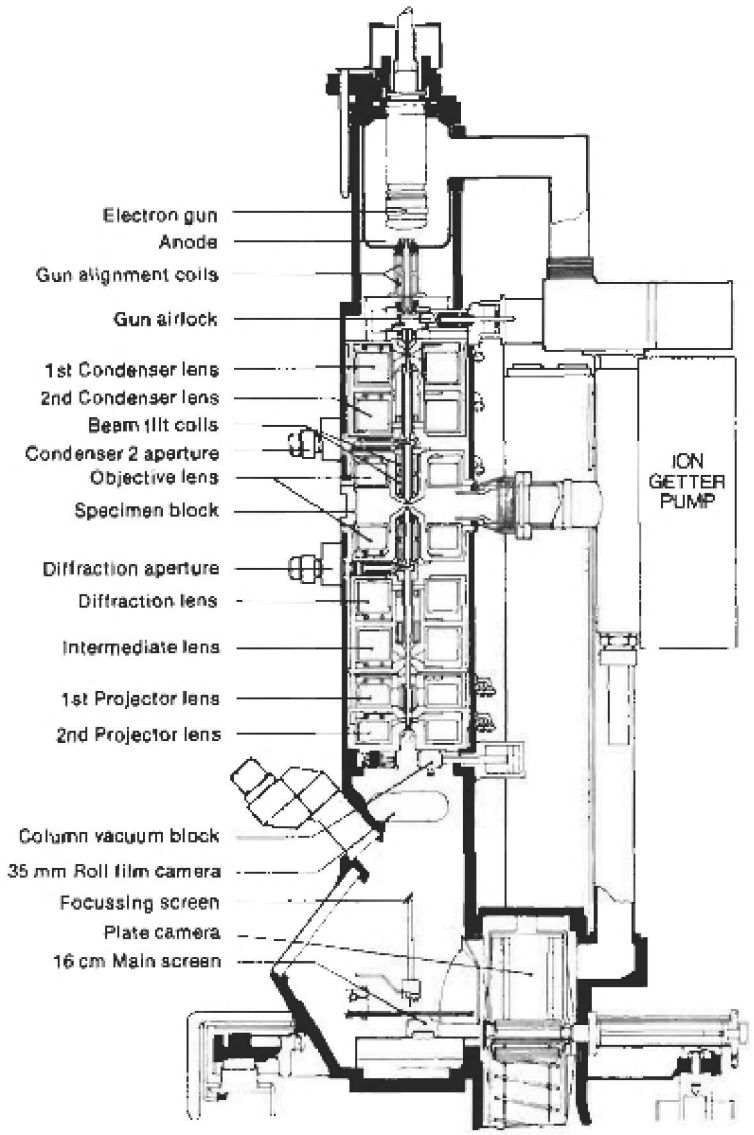

Fig. 20: Shows the cross section of a conventional TEM [32].

- Turn on the acceleration voltage in steps of 50 kV up to the maximum acceleration voltage of 300 kV.
- Turn on the current of the filament in a period of a few minutes to extend their lifetime.
- Use the specimen translation controls to bring either the edge of the hole or any other feature to the center of the screen and set the magnification to somewhere between 5000x and 10000x.
- Remove both diffraction and selected area apertures from the column before adjusting the sample eucentricity(the height of the sample with the z-control). Tilt the sample back and forth around the primary tilt axis(is a fixed axis with respect

to the microscope column) to minimize the lateral movement of the sample during tilting.

In case the beam is not proper aligned several alignment steps need to be performed.

- A gun alignment [38]: Use the gun tilt controls to obtain a symmetric filament image for a LaB_6 source. If no undersaturated image can be obtained, then the gun tilt controls should be adjusted so that maximum brightness is observed on the viewing screen.

- Condensor aperture alignment [38]: The electron beam should expand and contract concentrically when the second condensor lens current is changed. If the center of the beam moves upon changing this current, then the condensor aperture should be transuated until no further movement occurs for wide range of beam diameters. An application which needs a high beam current should use a large- diameter condensor aperture, wheras observations which need a high beam coherence should sacrifice some current by selecting a smaller diameter aperture.

- Condensor astigmatism correction [38]: The incident electron beam should have a circular cross-section for all settings of the second condensor lens. Condensor lens astigmatism can be recognized read ily as an elliptical disortion of the beam, which changes major axis when the second condensor lens current goes from an under-focus to an over focus condition. The condensor stigmator coils must be used to correct the beam shape. Condensor astigmatism can also be corrected in the in-focus condition (smallest beam diameter) by ensuring that the filament tip produces the sharpest possible image(under- saturated condition).

- Filament saturation [38]: Adjust the filament saturation by turning down the saturation a few steps and align it with the multifunction controls that an inner cicle is surounded by an outer circle.

- Pivot x and y: Using the multifunction controls x and y to bring the possible two beam spots togehter and afterwards center the beam spot with the shift controls x and y.

- Rot center: Find a feature on the specimen for the wobble procedure and try to stop wobbling as good as possible by using the multifunction controls x and y.

When the alignment procedure has been completed the methods of specimen observation are possible. In this work bright field, dark field and diffraction mode was used to investigate the radiation damage on the sample.

Obtaining a bright field(BF) image [38]

A bright filed (BF) image is obtained by inserting the diffraction aperture that the signal comes from electrons of the transmitted beam (see Fig. 21), these are electrons which are leaving the sample in the same direction as they entered it. The interaction of electrons with heavy atoms is stronger than with light atoms so if the thickness is homogeneous, areas in which heavy atoms are concentrated appear with a darker contrast than such with light atoms this is known as the mass contrast. In a conventional prepared TEM foils the thickness gradually increase from the hole which occured through the preperation so more electrons are scattered in thick than in thin areas so that thick areas appear dark this is known as the thickness contrast. Independent of the reason of scattering, all scattered electron beams are deflected away from the optical axis and blocked by the objective aperture so that these areas appear dark in the BF-image(see figure).

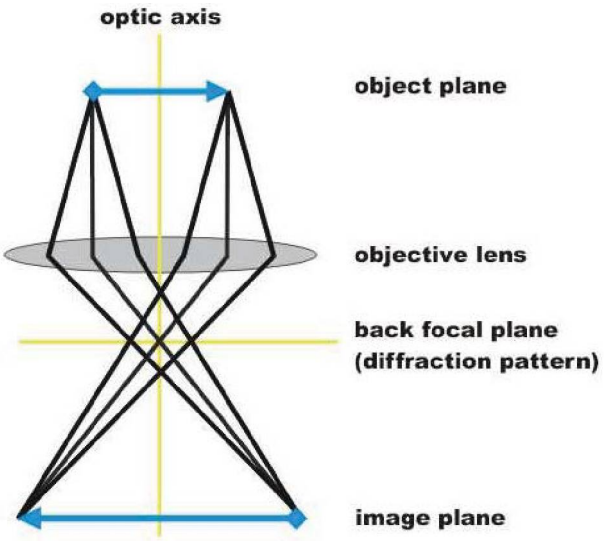

Fig. 21: Illustration of the course of the beam to obtain a BF image [39].

Obtaining electron diffraction(ED) pattern [32]

In a crystalline material many electrons are (nearly elastically) scattered and can be described as a reflection of the beams at planes of atoms (lattice planes) as it illustrated in Fig. 22. The interference is constructive when the phase shift is a multiple of 2 π, this condition leads to a simple equation known as Bragg's law which gives the relation between the interplanar distance d and the diffraction angle θ [14]:

$$n\,\lambda \;=\; 2d\,\sin\,\theta. \tag{12}$$

In electron diffraction(ED) the scattering angles are rather small: $0 \leqslant \theta \leqslant 2\,^{\circ}$. Therefore interplanar distances can be calculated from ED patterns since the wavelength λ of the

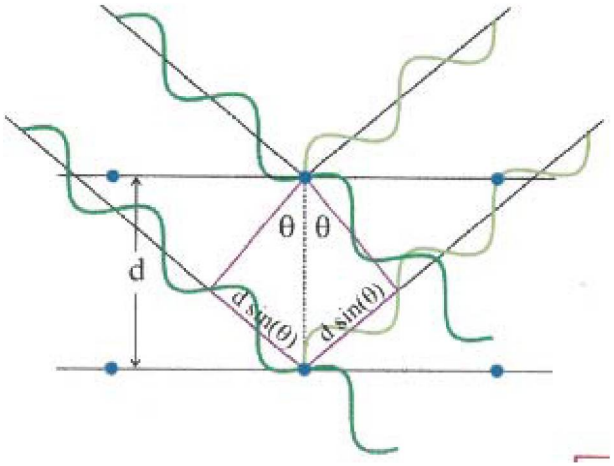

Fig. 22: A beam (with a wavelength λ) strikes a crystal surface in which the layers of atoms or ions are separated by a distance d, the maximum intensity of the reflection of the beam occurs when sin θ = n λ/2d, where the Bragg angle θ is the complement of the angle of incidence and n is an integer [40].

electrons is known.

$$\theta = \frac{\lambda}{Ld} \tag{13}$$

$$\theta = \frac{\lambda}{Ld} \Rightarrow \frac{\frac{R}{2}}{L} \Rightarrow \lambda\, L = Rd = const \tag{14}$$

where R is the camera length(distance between diffraction spot and central spot from the transmitted beam).
Going from image to diffraction mode by insert the selected area aperture and select an aperture size that covers the area of interest in the sample that has to be centered first on the screen. In diffraction mode, an ED pattern is obtained on the screen from the sample area illuminated by the electron beam [38]. An ED pattern of a single crystal will produce a spot pattern, a polycrystal will produce a powder or ring pattern and a glassy or amorphous material will produce a series of diffuse halos on the screen [39].
Further often used modes of imaging are:

- Kickuchi lines are parallel pairs of dark and bright lines they often appear on ED pattern and only exist in thick samples. An example of a two beam ED pattern with a number of Kickuchi lines.

- The term two beam denotes that the straight through beam (transmitted beam , 000, and one diffraction spot are both diffracting very strong in comparison to all other spots.

Idenxing of a ED pattern [38]

When the orientation of the electron beam is unknown:

One approach is to consult tables of angles and distance ratios for the low index reflections for the structure of the crystal we are imaging for example a fcc crystal. When making such tables spots which are forbidden by the lattice type they should be excluded which for a fcc lattice are those with hkl all even or all odd. Now we pick two spots on the diffraction pattern and measure the angle between them and the ratio of their distance (x/y) from the 000 spot as shown in Fig. 23 and see if they correspond to any of the values in the tables. Further spots can be indexed by vector addition when we know for sure what two of the non-collinear dots are.

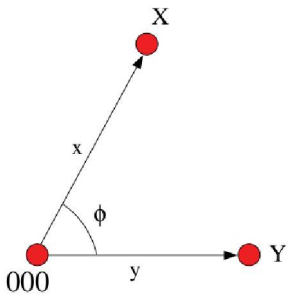

Fig. 23: Indexing a ED pattern by measuringing the angle between two spots and the ratio of their distance (x/y) from the 000 spot.

Obtaining a dark field(DF) image [37]

To obtain a DF image insert the aperture to block the transmitted beam and most of the diffraction pattern while selected scattered electrons are allowed to pass the objective aperture to form the image (see Fig. 24). Information like planar defects or particle size can be collected by obtaining DF images.

Obtaining thickness measurements of the foil from dislocation lengths [41]

- 1.Find a region of interest or a feature of interest e.g., dislocation(s).
- 2.Tilt to a two beam condition so that the dislocation is visible in BF image.
- 3.Take the BF image $^{\#}1$ of the dislocation and note the tilting position.
- 4.Tilt in BF mode not to loose the region of interest as long as the same dislocation is visible in the BF image again than take the BF image $^{\#}2$ and note the new tilting position.
- 5.Using an imaging program (for example: ImageJ) to measure the different lenght of the same dislocation appearing in the BF image $^{\#}1(x_L)$ and $^{\#}2(x_R)$ and by using

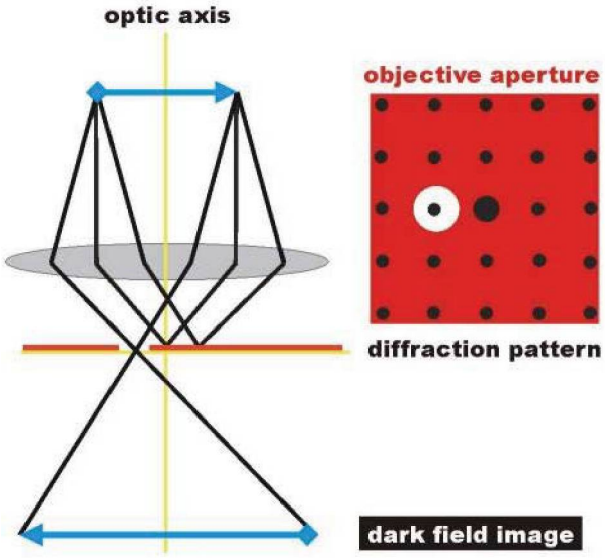

Fig. 24: Shows the course of the beam to obtain a DF image [39].

the following equation to calculate the thickness Z of the foil:

$$Z = \frac{x_{\mathrm{R}} - x_{\mathrm{L}}}{2 \sin\left(\frac{\theta}{2}\right)}. \tag{15}$$

Where θ is the difference of the tilting angle from image $^{\#}1$ to image $^{\#}2$,
x_R is the length of the dislocation from image $^{\#}1$ and
x_L is the length of the dislocation from image $^{\#}2$.

Obtaining the determintation of dislocation density in TEM foils

- Metode by Bailey and Hirsch(1960): They measure the total projected lenght R_p of dislocation line in a given area A on typical micrograph. Then, on the assumption that the dislocation segments are randomly orientated with respect to the plane of the film, the dislocation density is |42, 43|:

$$\rho = \frac{(4\ \pi) R_{\mathrm{p}}}{At}. \tag{16}$$

- Methode by Smith and Guttman(1953): A set of random lines with the total length L is marked on an area A, and the number of intersections N which dislocations make with the grid lines is measured and t is the thickness of the foil, then the total projected length R_p is |43|:

$$R_{\mathrm{p}} = \frac{\pi\ NA}{2L} \Rightarrow \rho = \frac{2N}{Lt}. \tag{17}$$

- Methode by Ham: A set of five lines drawn in random directions on a plate taken at a magnification at 20 000 gave enough intersections(about 50), and it was not necessary to enlarge the micrographs as it was for the direct measurement of R_p. The new method proved to be about 10-20 times faster in measuring alone [43].

4 Results and Discussion

After the implantation/irradiation at room temperature was completed by using the parameters listed in Table 2 all candidate materials were characterised by using nanoindentation and AFM as described in chapter three.
Characterisation by using TEM was performed on all pre irradiated samples as well as on all proton irradiated samples at room temperature. From the high temperature experiments only a few FIB foils were prepared and from the set of samples of the Helium implantation no FIB foil was prepared. In Table 4 are all materials listed from which FIB foils were prepared and a characterisation with TEM was performed.
All properties were obtained from the conventional materials (HT-9 ferritic- and HT-9 tempered martensitic steel) before and after the irradiation and compared with data obtained of the advanced materials (MA956 and MA957).

Table 4: FIB foil test matrix before and after the implantation/irradiation

material	pre irradiation	He RT	Proton RT	Proton 300°C	Proton 550°C
HT-9 ferritic	X		X	X	
HT-9 tempered martensitic	X		X		X
MA956	X		X		
MA957	X		X	X	

4.1 HT-9 ferritic and HT-9 tempered martensitic steels

4.1.1 Pre Irradiation

Results obtained by microhardness measurement

The microhardness measurement was performed only on the pre irradiated samples by using a Buehler Micromet 5100 series (version 2.10) together with the Buehler OmniMet MHT software which measures the Vickers imprint optically. A series of 5 indents, each with a force of 200 g, 500 g and 1000 g on each material, was taken and measured at Mag 500 x to determine the microhardess of HV0.2, HV0.5 and HV1. The given values are the avarage of 5 indents and for the pre-irradiated HT-9 ferritic steel they are between

198- 203 as shown in Table 5.

Table 5: Microhardness of HT-9 ferritic steel

force	1.result	2.result	3.result	4.result	5.result	average value
200g	200,8	204,1	199,5	203,4	198,0	HV0.2 = 202,8
500g	196,5	197,5	199,4	198,9	199,4	HV0.5 = 198,3
1000g	200,8	201,6	198,2	200,8	200,8	HV1 = 200,4

The microhardness data of the pre-irradiated HT-9 tempered martensitic steel was evaluated in the same way as of the pre irradiated HT-9 ferritic steel, the average values of 5 indents are between 255- 259 as listed in Table 6.

Table 6: Microhardness of HT-9 tempered martensitic steel

force	1.result	2.result	3.result	4.result	5.result	average value
200g	258,6	258,6	263,2	257,5	258,6	HV0.2 = 255,1
500g	257,6	258,3	258,3	261,1	259,7	HV0.5 = 259,0
1000g	255,7	256,7	252,7	256,7	253,7	HV1 = 259,3

Results obtained by TEM of the pre irradiated HT-9 ferritic steel

The pre irradiated TEM samples were prepared as described in Subsection 3.2.3 by using a technique to electro-polish 3 mm discs at conditions listed in Table 3 and the examination was performed with a CM 30 instrument at various magnifications by using different imaging techniques to characterise the features of the materials. The bright field (BF) images shown in Fig 25 are taken at a low magnification and do show the microstructure of the pre-irradiated HT-9 ferritic steel, where carbides are randomly distributed and embedded in the ferritic matrix.

The images shown in Fig 26 are of the pre irradiated HT-9 ferritic steel taken at Mag 21 kx. The left image in Fig 26 is taken in bright field (BF) mode and the right image is taken in dark field (DF) mode of a certain spot in the diffraction pattern which corresponds to the carbides shown in this area of the foil therefore they appear bright in the DF image.

The determination of the thickness of the foil is shown in Fig 27 and Fig 28 where the length of a dislocation was measured at various tilting angels. Afterwards the different

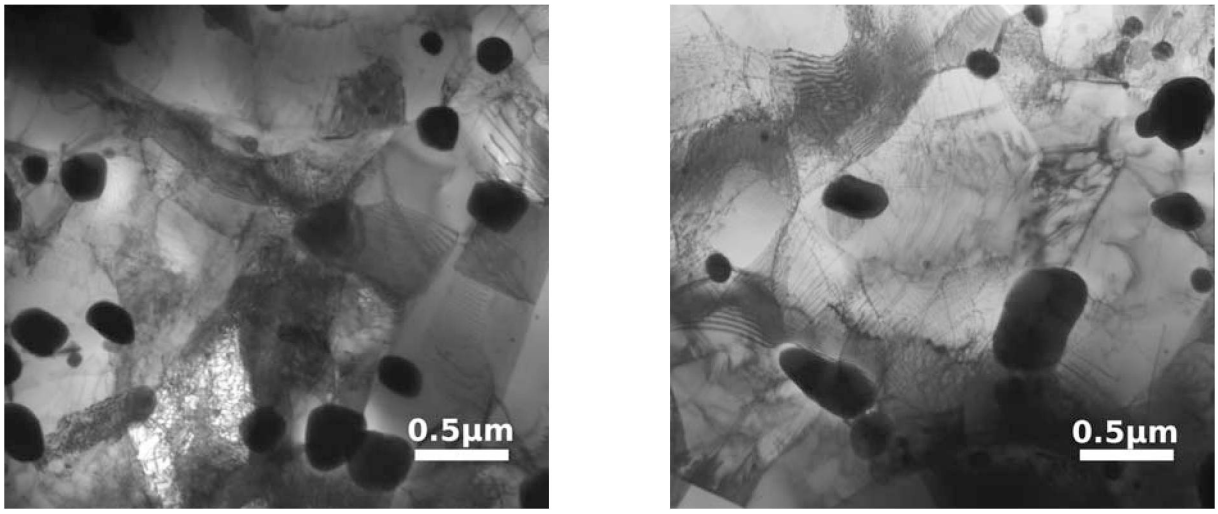

(a) (b)

Fig. 25: The BF images (a) and (b) are overview images of the microstructure of the pre irradiated HT-9 ferritic steel at Mag 13,5 kx.

lenghts of the dislocations were measured by using ImageJ software (Version 1.43r) to calculate the thickness Z according to the equation (15) specified in chapter 3 [44].

The calculated thickness of the pre irradiated HT-9 ferritic foil of Fig 27 is 192 nm and of Fig 28 is 198 nm.

The dislocation density was evelutated by using the methode by Ham as described in chapter 3. The image shown in Fig 29 is taken at a magnification of 52 kx and therefor the total projected length R_p is 2,45 * 10^{-5} m resulting in a dislocation densitiy ρ of 2,37 * 10^{14} m^{-2}.

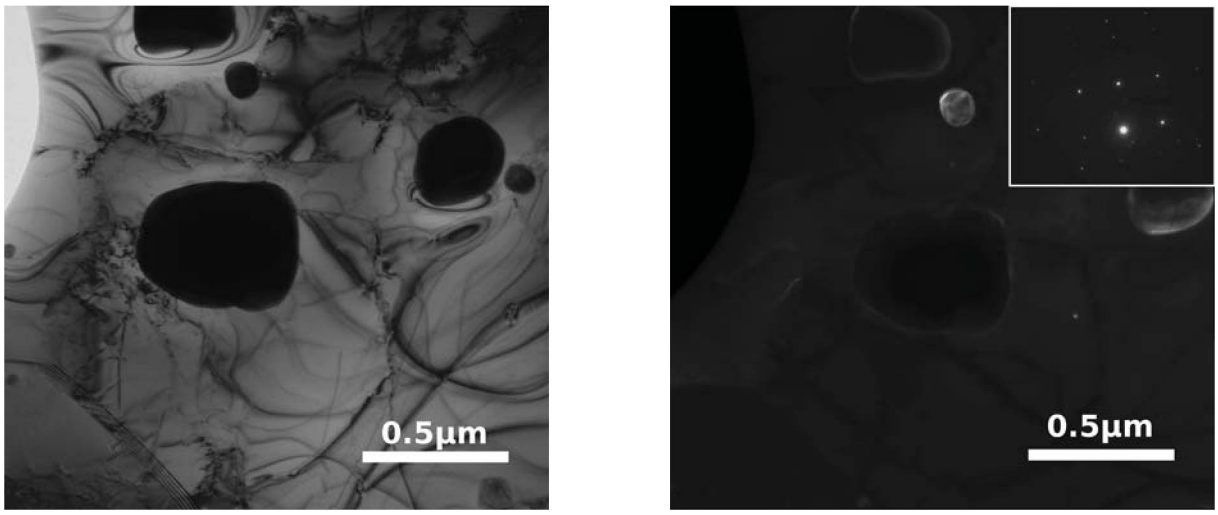

(a) (b)

Fig. 26: (a) showes a BF image of the pre-irradiated HT-9 ferritic steel taken at Mag 21 kx and in (b) is the DF image togehter with the ED-pattern where the reflex which is pointed on is coming from the carbides.

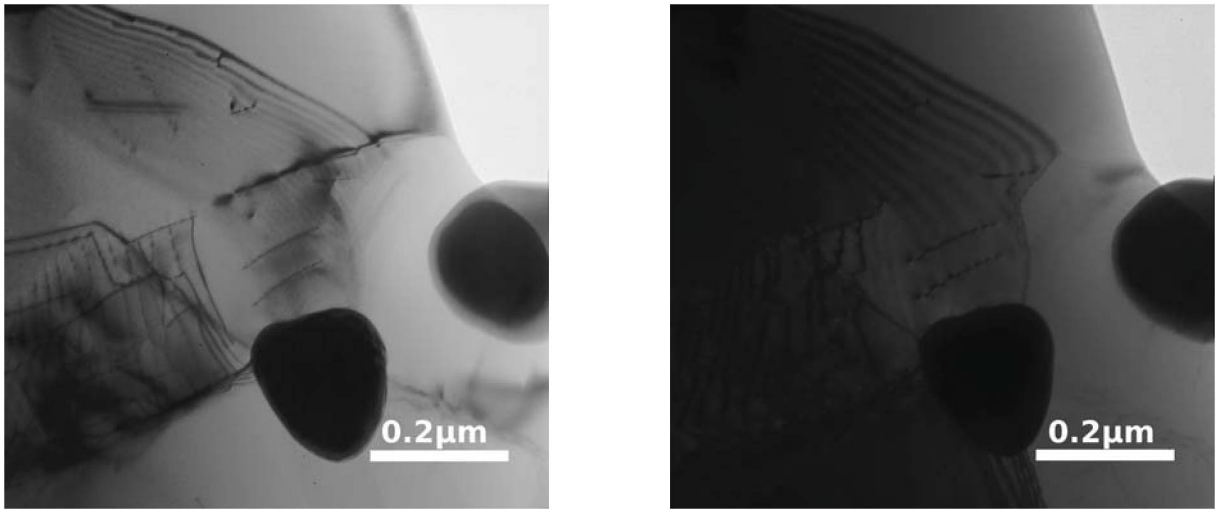

(a) (b)

Fig. 27: Both BF images are of the pre irradiated HT-9 ferritic steel and taken at Mag 52 kx at different tilting angles to determine the thickness of the foil. In (a) the tilting angel was 0° and in (b) the image was taken at an tilting angel of +13°.

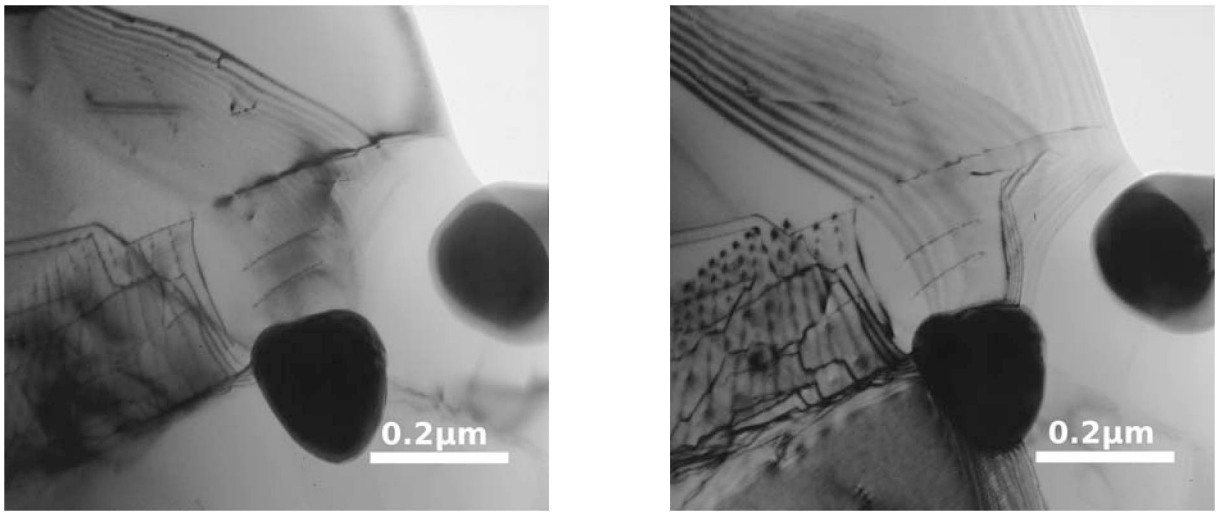

(a) (b)

Fig. 28: Both images are of the pre irradiated HT-9 ferritic steel, taken at Mag 52 kx but at different tilting angles to determine the thickness of the foil. In (a) the tilting angel was 0° and in (b) the images was taken at +2°.

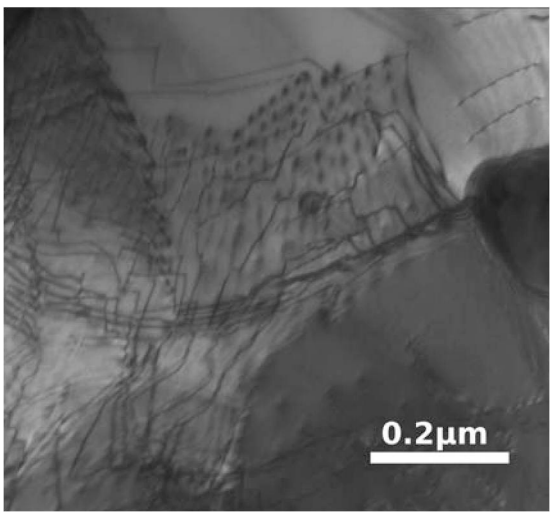

(a)

Fig. 29: Illustration of dislocations in two beam condition of the pre irradiated HT-9 ferritic steel taken at Mag 52 kx. From this micrograph the dislocation density was eveluated.

Results obtained by TEM of the pre irradiated HT-9 tempered martensitic steel.

In Fig 30 and Fig 31 the tempered martensitic structure is shown where between the martensite lath the carbides are elongated after the tempering process. At the thin areas of the foil the carbides were falling out due to the electro-polishing.

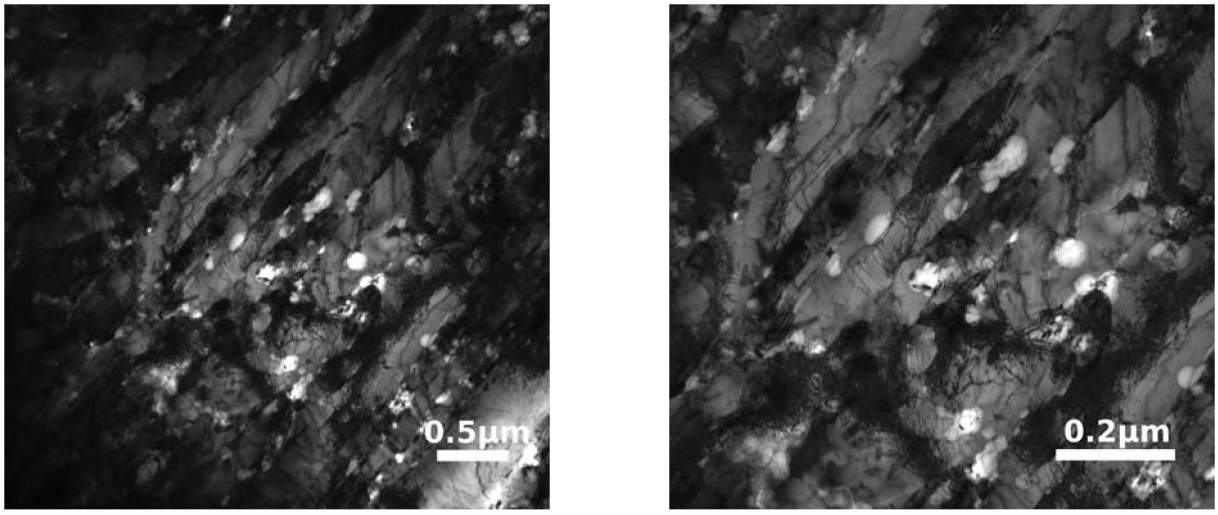

(a) (b)

Fig. 30: The BF images (a) and (b) are illustrating an overview of the microstructure of the pre irradiated HT-9 tempered martensitic steel at (a) Mag 10,5 kx and (b) Mag 17 kx.

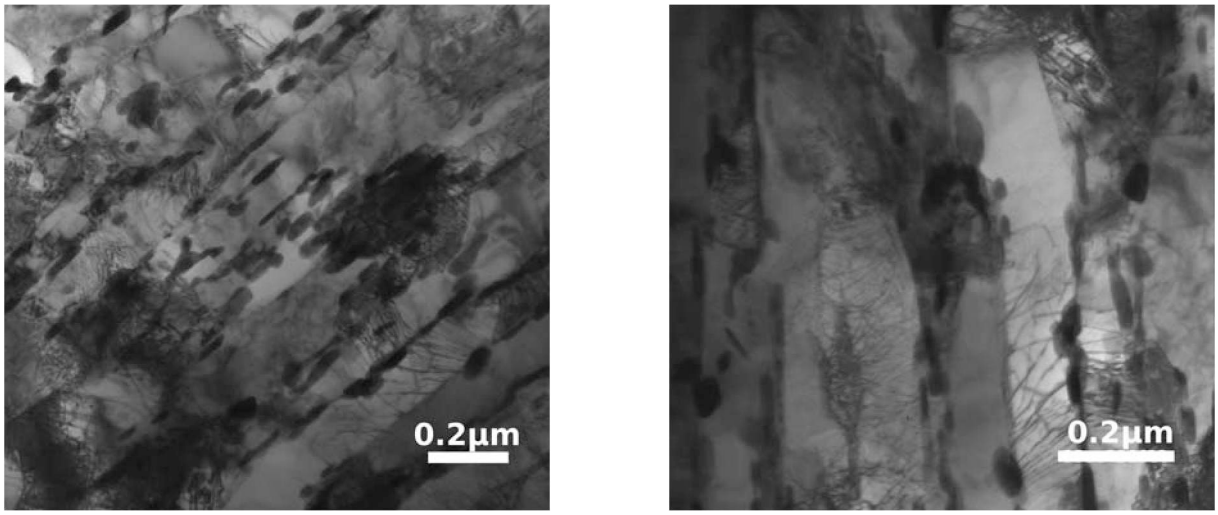

(a) (b)

Fig. 31: Both images show an overview of the microstructure of the pre irradiated HT-9 tempered martensitic steel taken at Mag 31 kx.

In Fig 32 the left image is taken in BF mode at Mag 42 kx and the right image is taken in DF mode at Mag 42 kx of a certain spot in the diffraction pattern which corresponds to the elongated carbides seen in this area of the foil so that they appear bright in the DF image.

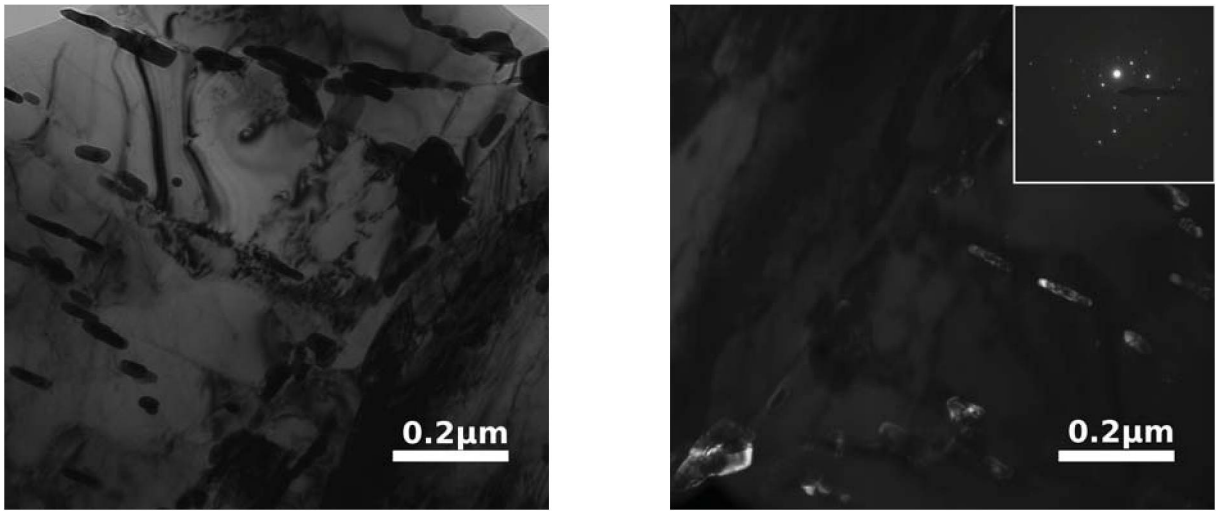

(a) (b)

Fig. 32: The pre irradiated HT-9 tempered martensitic steel is shown in image (a) in BF mode and in (b) is the DF image togehter with the ED-pattern where some reflexes are coming from the bright elongated carbides between the martensite lath. Both images were taken at Mag 42 kx.

Images of the pre irradiated HT-9 tempered martensitic steel of the same dislocation at various tilting angels are shown in Fig 33. The different lenght of the dislocations measured by ImageJ leads to a thickness of 205 nm of the foil of the pre irradiated HT-9 tempered martensitic steel.

The image of the pre irradiated HT-9 tempered martensitic steel shown in Fig 34 was taken to evaluate the dislocation density with the methode by Ham. After measuring the amount of intersections of the dislocations with the randomly set lines a total projected length R_p of 4,14 * 10^{-5} m was calculated and therefor the dislocation density ρ for the pre irradiated HT-9 tempered martensitic sample is approximatily 2,87 * 10^{14} m^{-2}.

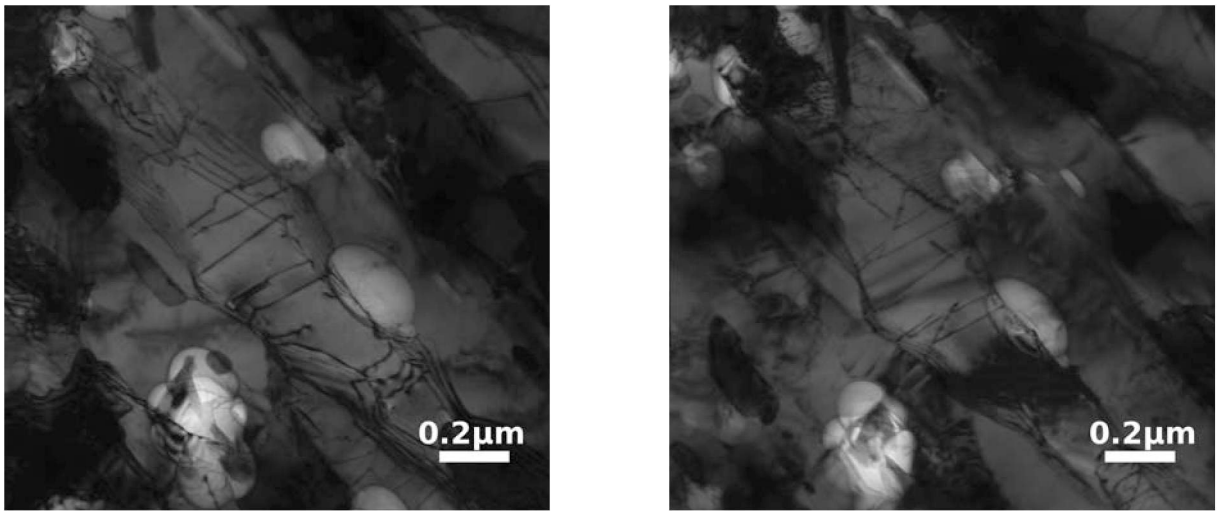

(a) (b)

Fig. 33: Both images of the pre irradiated HT-9 tempered martensitic steel were taken at Mag 52 kx but at different tilting angles to determine the thickness of the foil. In (a) the tilting angel was 0° and in the image shown in (b) the tilting angle was +4°.

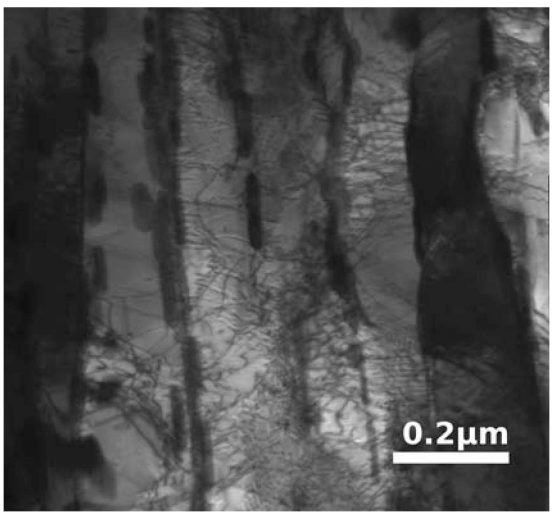

(a)

Fig. 34: The image of the pre irradiated HT-9 tempered martensitic steel shows dislocations in two beam condition at Mag 42 kx from which the dislocation density was eveluated.

4.1.2 Discussion of the pre irradiated conventional materials

TEM characterisation of the pre irradiated steels showed the microstructural change from HT-9 ferritic to HT-9 tempered martensitic. In the pre irradiated HT-9 ferritic steel the carbides are randomly arranged at the grain boundaries as shown in image (a) and (b) in Fig 25 but after the tempering process these carbides were enlongated due to the transformation to a HT-9 tempered martensitic structure and arranged along the martensite lath as illustrated in Fig 31 which results in an increase in microhardness from HV0.2 = 198 in HT-9 ferritic steel to HV0.2 = 255 in HT-9 tempered martensitic steel. The increase in hardness due to the fine microstructure correlates with an increase in dislocation density ρ from 2,37 * 10^{14} m^{-2} in HT-9 ferritic steel to 2,87 * 10^{14} m^{-2} in HT-9 tempered martensitic steel. The implantation with Helium at room temperature (RT) and the irradiation with protons at RT, 300 °C and 550 °C will reveal if an additional increase in hardness and dislocation densitiy due to the radiation damage will occur.

4.1.3 Helium implantation at room temperature

After the Helium implantation on the conventional materials was completed, the nanoindentation was performed as shown in Fig. 35. It was found that due to the high He content both samples showed strong cracking as it is illustrated in Fig. 36. Additional AFM analysis after indentation was performed to exemplify that these cracks are corresponding with the stopping region of He as they are going parallel to the sample surface. Also no pile-up surrounding of the indents was found at the row of the stopping region of He and the indents appear more shallow compared to the rest. The nanoindentation measurements were performed at areas with no cracks.

The fundamental properties affecting pile-up behavior are the ratio of the effective modulus to yield stress E_{eff}/Y and the work hardening rates [45]. In general, pile-up occurs in materials with large E_{eff}/Y and little or no capacity for work hardening rate. In order to determine the absence of a pile-up which correspond to the He stopping peak a depth profile (as shown in Fig. 37(c) and Fig. 38(c)) through three indents of three rows (as shown in Fig. 37(a) and Fig. 38(a)) within the nanoindent array was determined from an isometric projection as it is illustrated in Fig. 37(b) and Fig. 38(b) by using the AFM imaging software Gwyddion [46].

Fig. 39 presents the hardness data gained from nanoindentation after the He implantation to 3 dpa. The 3 dpa region of the samples did show some hardening (10-15 %). The He stopping peak resulted in a significant increase in hardness of 25-30 % while the 3 dpa

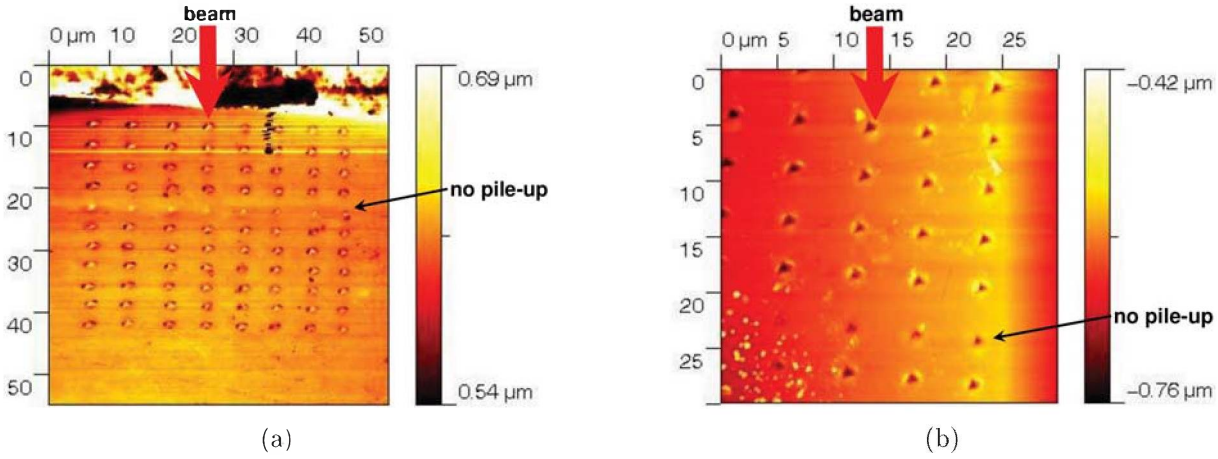

(a) (b)

Fig. 35: (a) The AFM image of a nanoindent array performed on the Helium implanted HT-9 ferritic steel in which one row shows no pile-up.(b) Overview of the nanoindent array performend on the Helium implanted HT-9 tempered martensitic steel where a row of indents shows no pile-up.

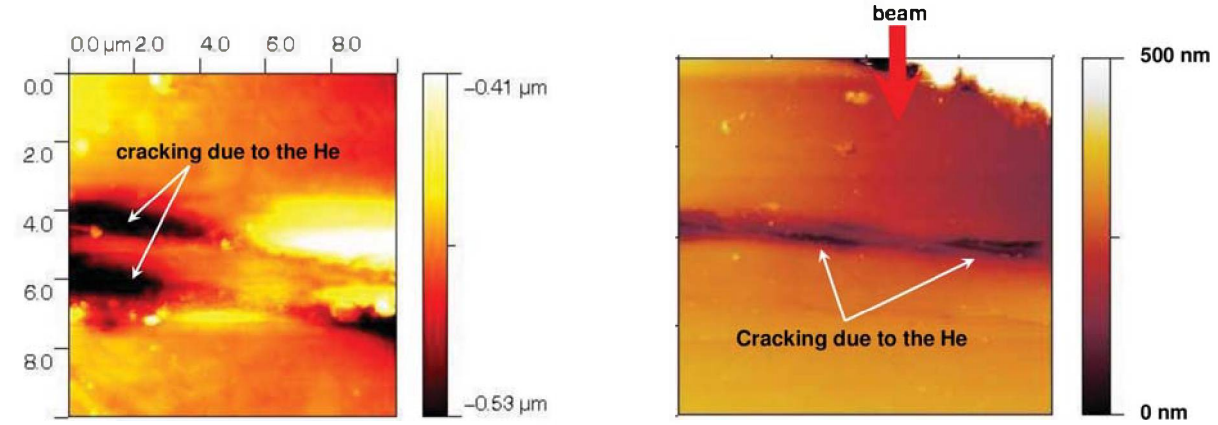

(a) (b)

Fig. 36: (a) The AFM image illustrates the occurance of cracking due to the high He content in HT-9 ferritic steel. (b) shows a similar behavior in the HT-9 tempered martensitic steel.

irradiation region only showed a 3 % hardness increase for HT-9 tempered martensitic steel and 7 % for the HT-9 ferritic steel as shown in Fig. 40.

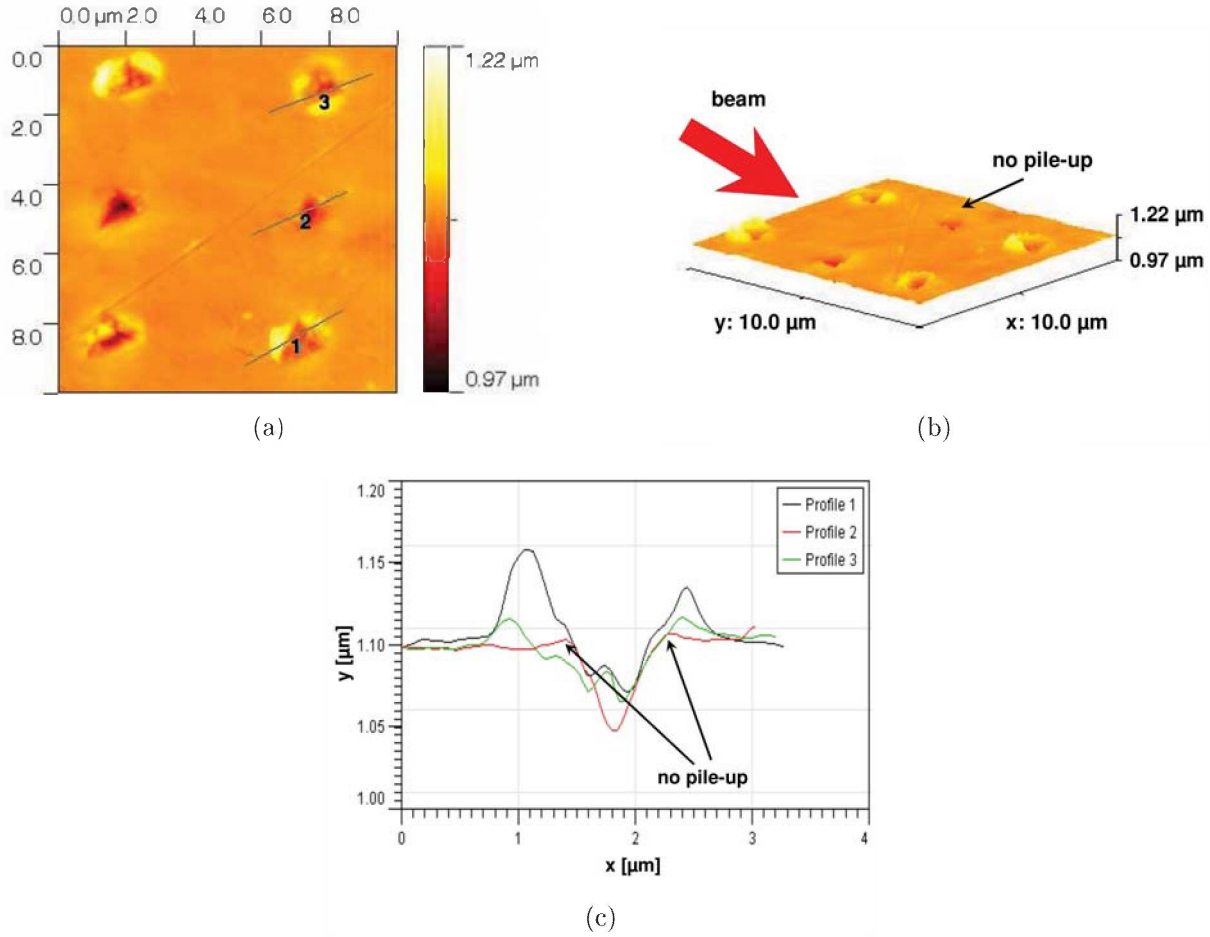

Fig. 37: In image (a) an array of three nanoindents performed on the Helium implanted HT-9 ferritic steel is shown. (b) The isometric projection developed from the array in image (a) shows that there is no pile-up for the selected indents. (c) Depth profils of indents can be determined from the AFM image in (a).

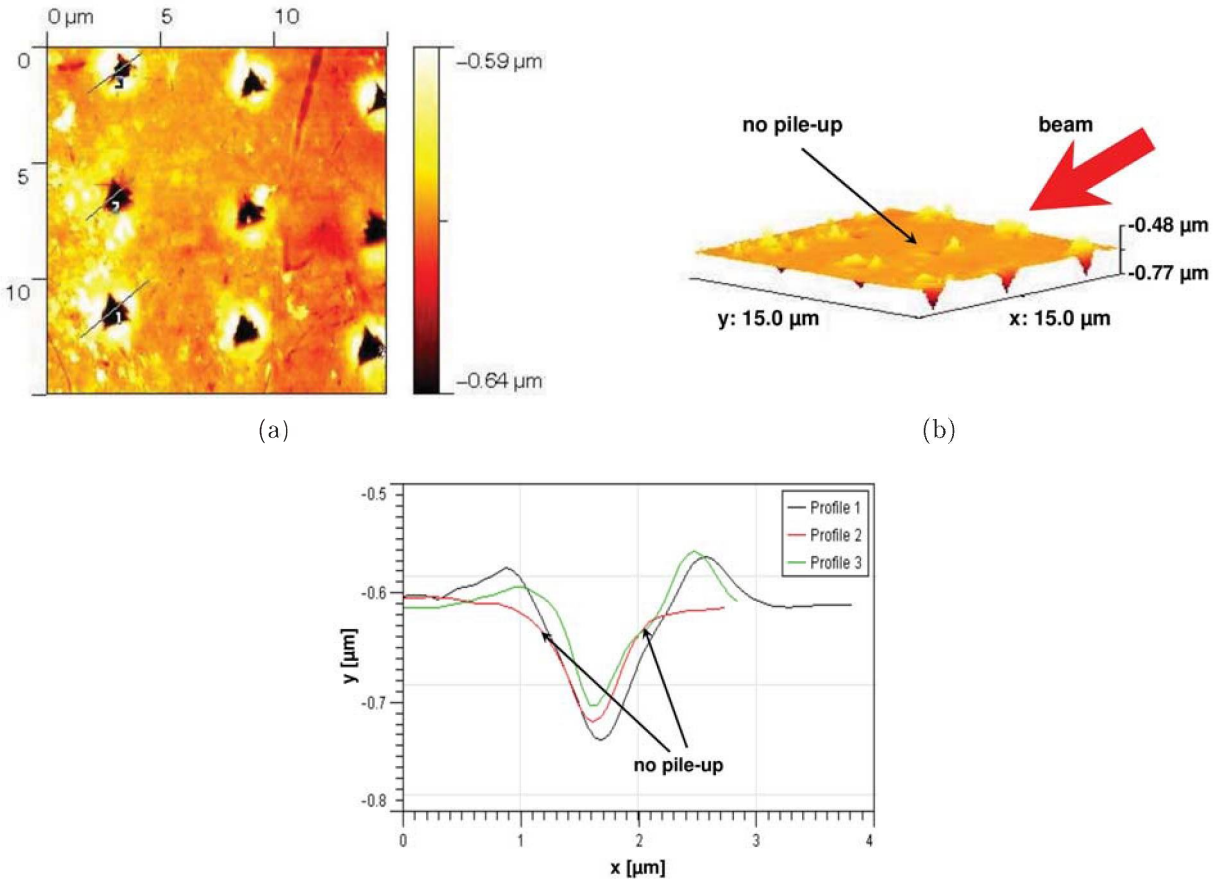

Fig. 38: In image (a) an array of three nanoindents performed on HT-9 tempered martensitic is shown. (b) The 3D image developed from the array in image (a). (c) Depth profil of the indents determined from the isometric projection in (a).

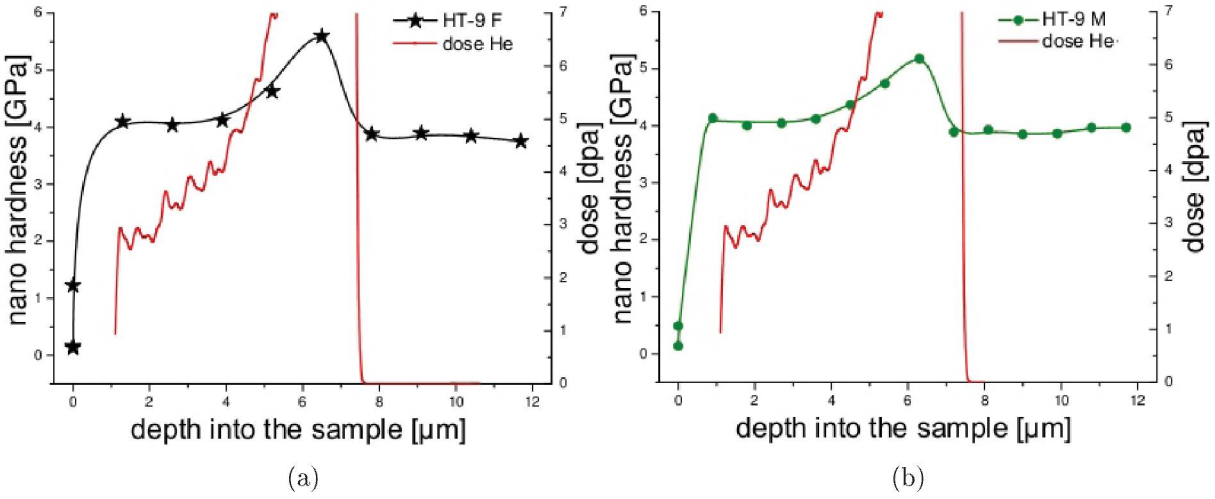

Fig. 39: (a) The hardness increase due to the He implantation of HT-9 ferritic steel is shown.(b) Hardness vs depth graph of the HT-9 tempered martensitic steel shows an increase in hardness due to the He implantation.

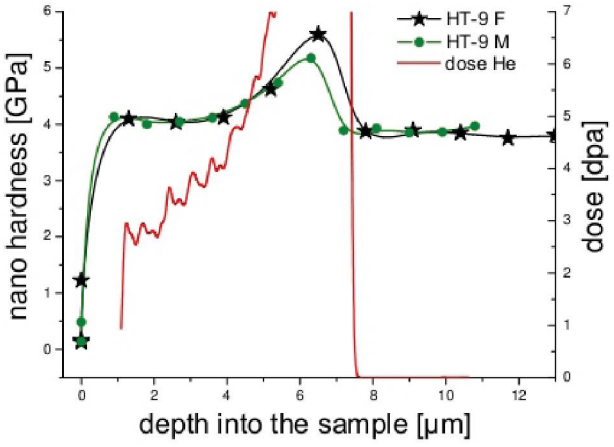

(a)

Fig. 40: Comparison of hardness vs depth of the Helium implanted HT-9 ferritic- and HT-9 tempered martensitic steel and the associated dose profile of Helium.

4.1.4 Discussion of the Helium implanted conventional materials

After the Helium implantation was completed only a characterisation by using nanoindentation and AFM was performed, therefore no results from TEM are available to discuss. The implantation of HT-9 ferritic- and HT-9 tempered martensitic steel with Helium ions showed a distinct increase in hardenss of 25-30 % measured by using nanoindentation as shown in Fig. 39 while the 3 dpa irradiation region only showed a 3 % hardness increase for the HT-9 tempered martensitic steel and a 7 % increase for the HT-9 ferritic steel. During the investigation by using AFM cracks occurred in the material at the depth where the He+ stopping region is expected. It was found that the nano indents placed in that region (in a non cracked area) showed no pile-up surrounding. It is assumed that the Helium ions remain in the stopping region of the sample which increases the number of defects in the region while the protons are small enough to diffuse out of the material so that only the dpa effect in that region remains. The irradiation with protons will reveal if the cracking and the absence of pile-up surrounding at the indents is due to the Helium or the radiation damage.

4.1.5 Proton irradiation at room temperature

After the room temperature (RT) irradiation with protons on HT-9 ferritic- and HT-9 tempered martensitic steel was completed and the nanoindentation on those samples was performed as shown in Fig. 41 (a) and (b) no cracking in the stopping region was found as due to the He implantation. In the AFM analysis it was found that all indents even the row of indents set in the stopping region showed pile-up. The sink effect as determind from AFM measurments on the He implanted samples could not be found again on the proton samples. In Fig. 42 and Fig. 43 the depths of the indents were evaluated with Gwyddion by gathering an isometric projection to receive a depth profile where more clearly the missing of a pile up at the stopping peak of the protons could not be observed. So the post indentation AFM revealed that no difference in pile up could be detected between the stopping region and the bulk material contrary to the results gained from the He implanted samples.

Fig. 44 presents the hardness results gained from nanoindentation after the proton irradiation at RT. The stopping peak region shows a clear hardness increase of 24 % for the HT-9-ferritic steel and an increase of 12 % for the HT-9-tempered matensitic steel. The ion stopping region shows a clear increase in hardness for both materials of about 25-30 % relative to the surrounding area.

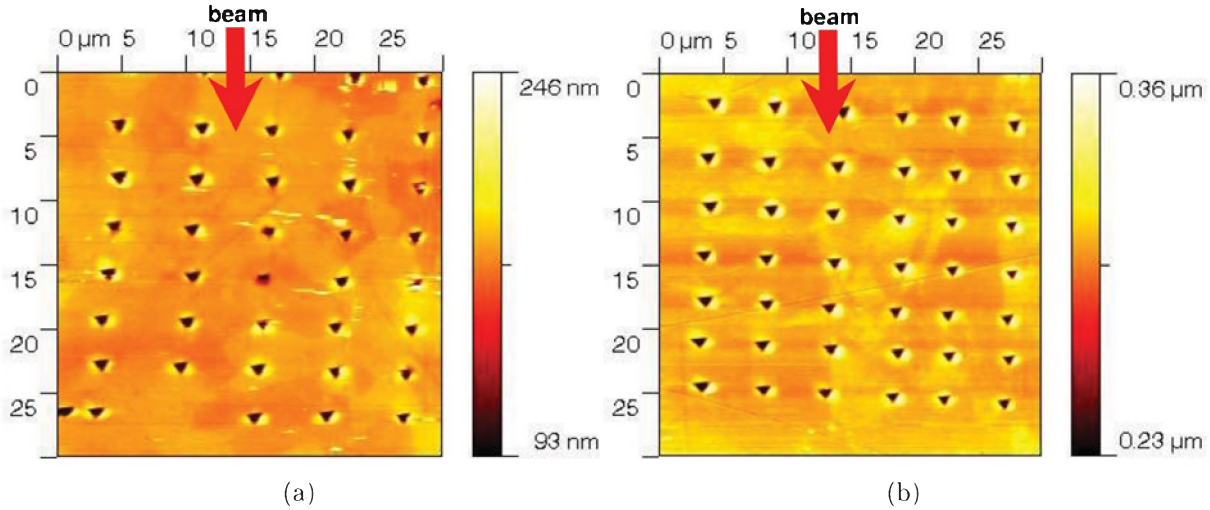

(a) (b)

Fig. 41: (a) The image illustrates the array of indents performed on HT-9 ferritic steel after the RT irradiation with protons. (b) Nanohardness performed on the with protons at RT irradiated HT-9 tempered martensitic steel.

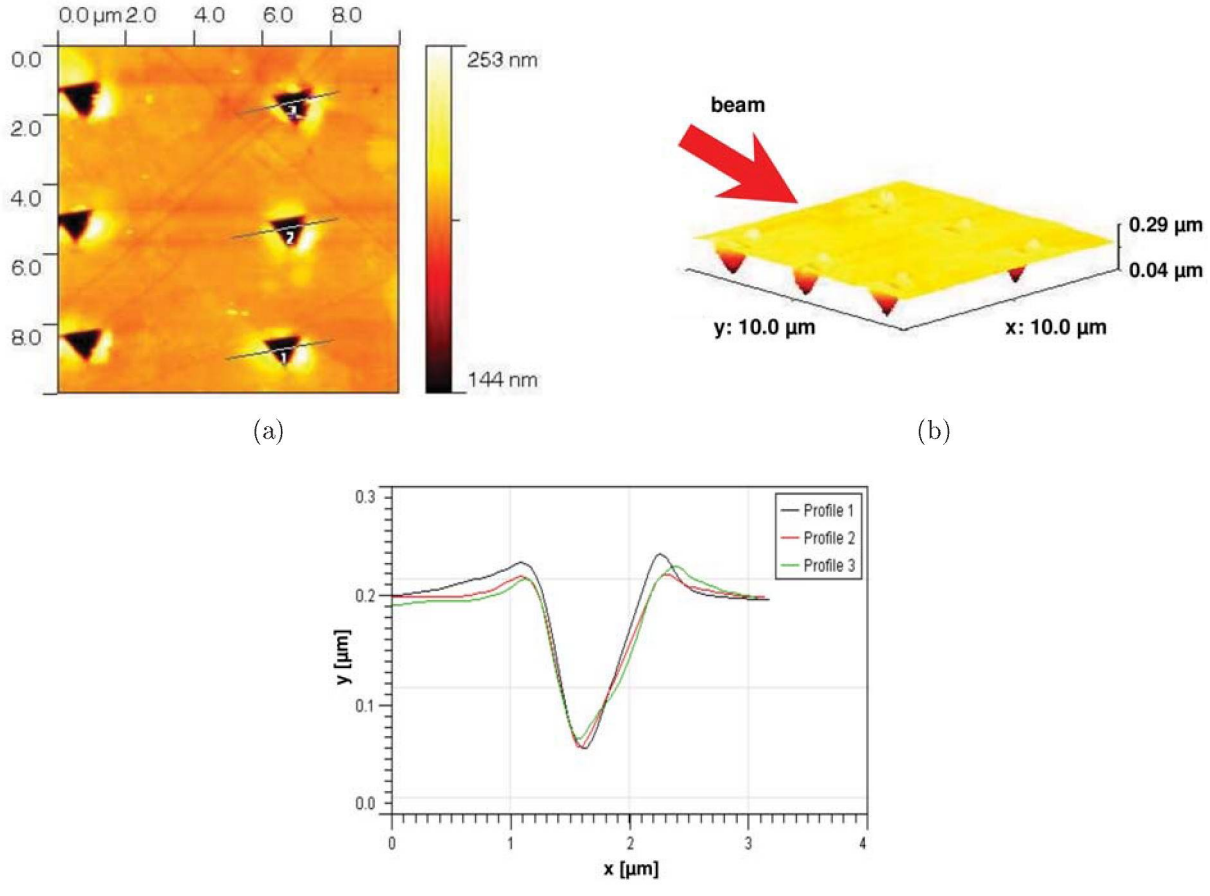

(a) (b)

(c)

Fig. 42: In image (a) an array of three nanoindents performed on HT-9 tempered martensitic steel after the RT irradiation with protons is shown. (b) The isometric projection developed from the array in image (a). (c) Depth profil of the indents determined from AFM image (a).

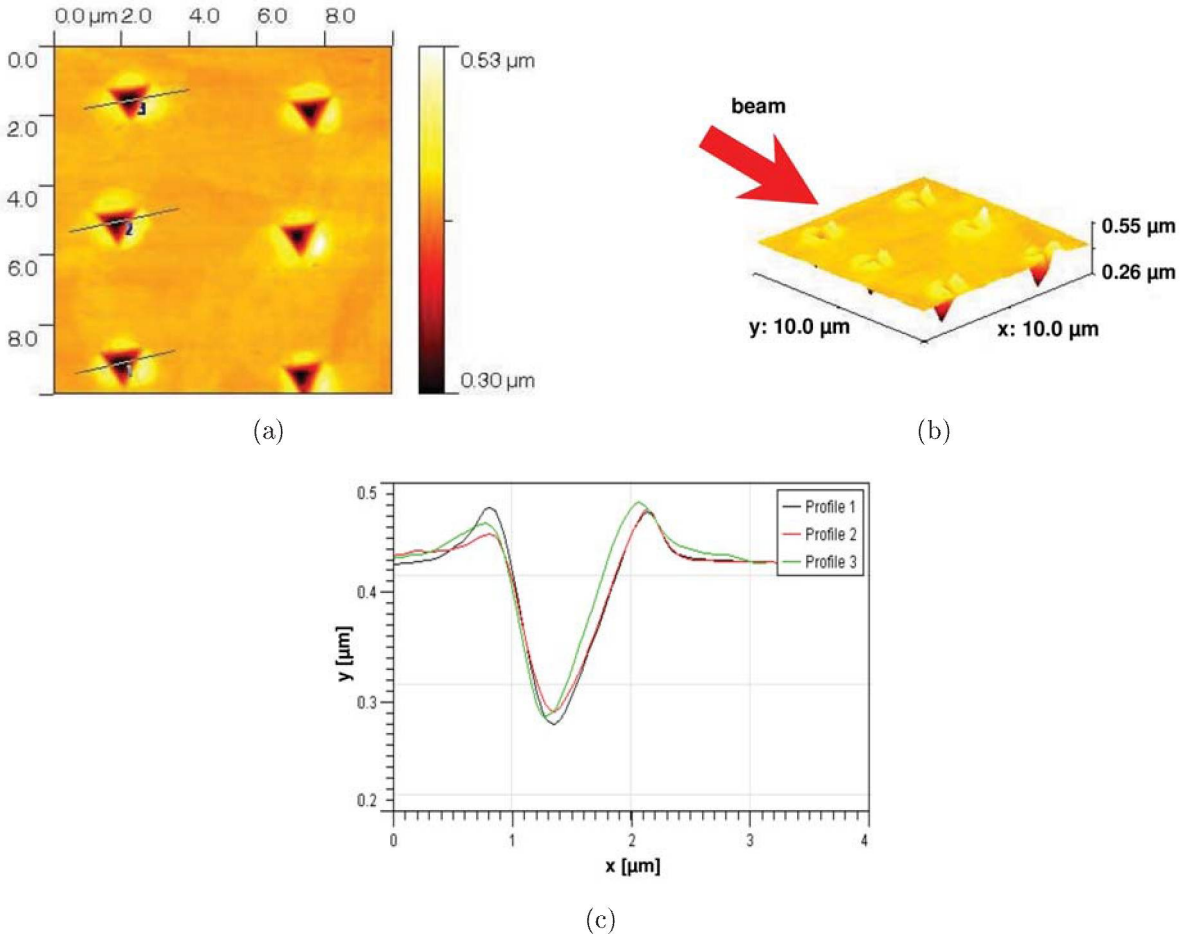

Fig. 43: In image (a) an array of three nanoindents performed on HT-9 tempered martensitic steel after the RT irradiation with protons is shown. (b) The isometric projection developed from the array in image (a). (c) Depth profil of the indents determined from the AFM image (a).

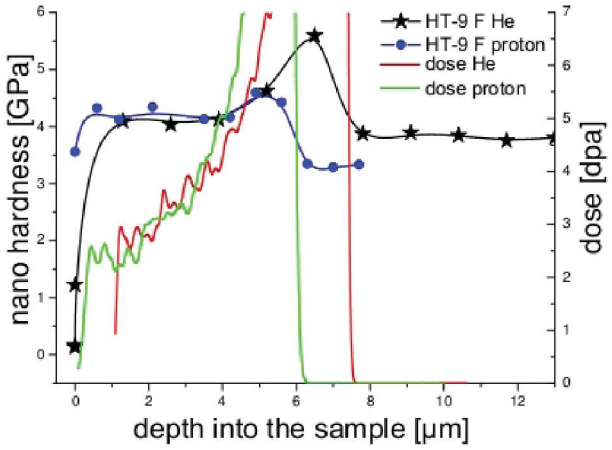

(a)

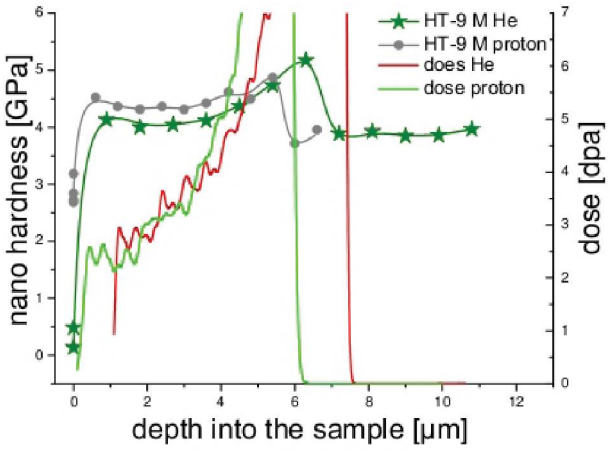

(b)

Fig. 44: Hardness versus depth graph of HT-9 ferritic steel (a) and HT- tempered martensitic steel (b) after the RT irradiation with protons in comparison to the data obtained from the He implantation.

Results obtained by TEM after the RT irradiation of HT-9 ferritic steel. The TEM image depict in Fig. 45 is giving an overview of the FIB foil of HT-9 ferritic which was prepared after the proton irradiation at RT was completed. It shows some damage similar to black spot damage in a depth of about 6 μm where the most damage caused by irradiation should has taken place. Due to the irradiation vacancies will be induced which can collapse to dislocation loops and this effect is referred to as black spot damage. The depth of about 6 μm is about the stopping range of the ions.

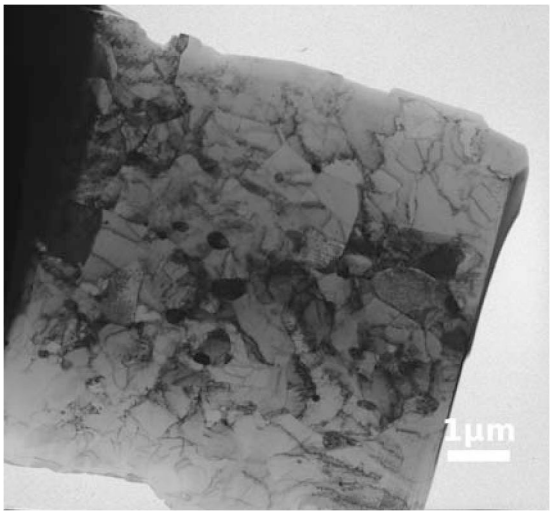

(a)

Fig. 45: An overview of the FIB foil of HT-9 ferritic after the irradiation with protons at RT taken at Mag 4400 x.

After tilting at various angels the images always showed a region in about 6 μm depth where black spot damage appeared as it is clearly seen in the following images in Fig. 46 and Fig. 47.

In Fig 48 the left image is taken in BF mode at Mag 10,5 kx and the right image is taken in DF mode at Mag 10,5 kx of a certain spot in the diffraction pattern which corresponds to the carbides seen in this area of the foil so that they appear bright in the DF image.

To determine the thickness of a foil, of the HT-9 ferritic steel after the room temperature irradiation, the lenght of the same dislocations appering at different tilting angels was measured. This leads to a thickness of the foil of 176 nm after two different measurments, first the pair at 0° and +4°as shown in Fig 49 and second the pair 0° and +2° in Fig 49.

The image shown in Fig 51 leads to a total projected length R_p of 3,29 * 10^{-5} m which results in a dislocation densitiy ρ for the HT-9 ferritic sample after the irradiation with protons at RT of approximately 2,65 * 10^{14} m^{-2}.

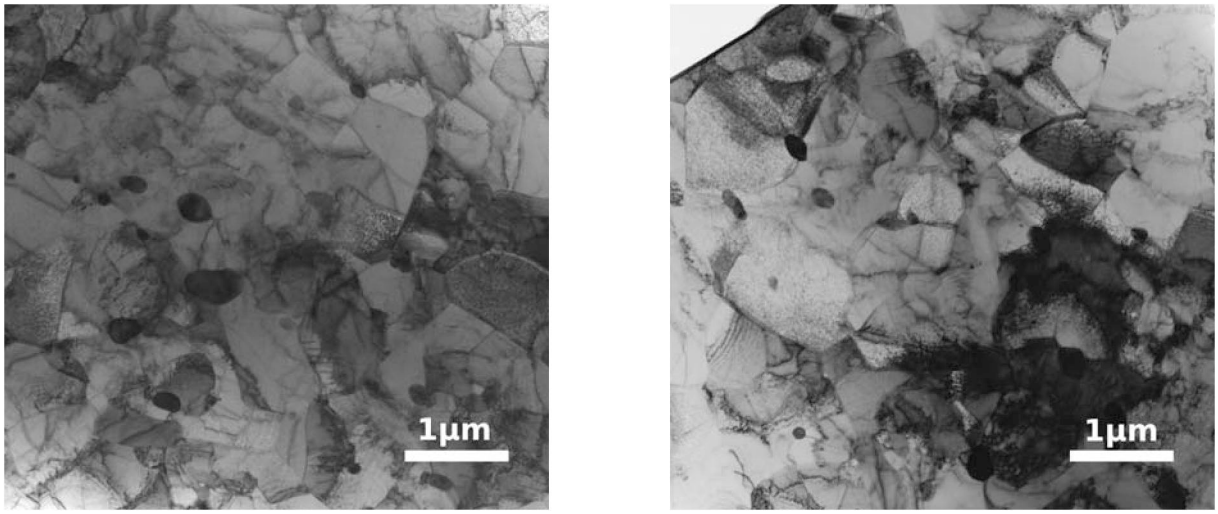

(a) (b)

Fig. 46: The BF images (a) and (b) show an overview of the microstructure and some black spot damage occurring in HT-9 ferritic after the irradiation with protons at RT, taken at Mag 7400 x.

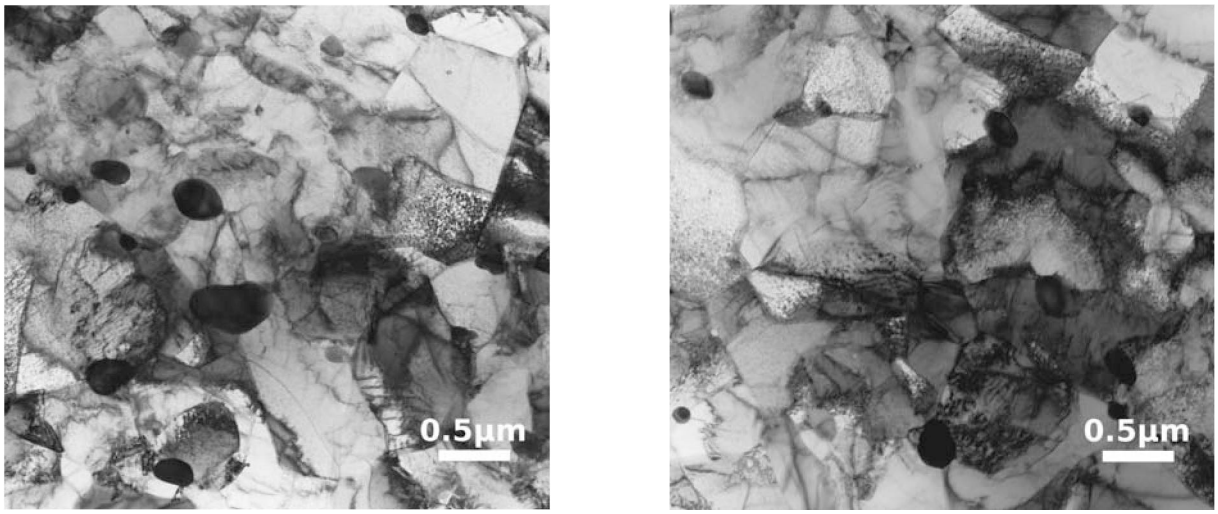

(a) (b)

Fig. 47: The BF images (a) and (b) illustrate the microstructure of HT-9 ferritic after irradiation at RT with protons at Mag 10,5 kx. In a depth of about 6 μm some black spot damage occurred.

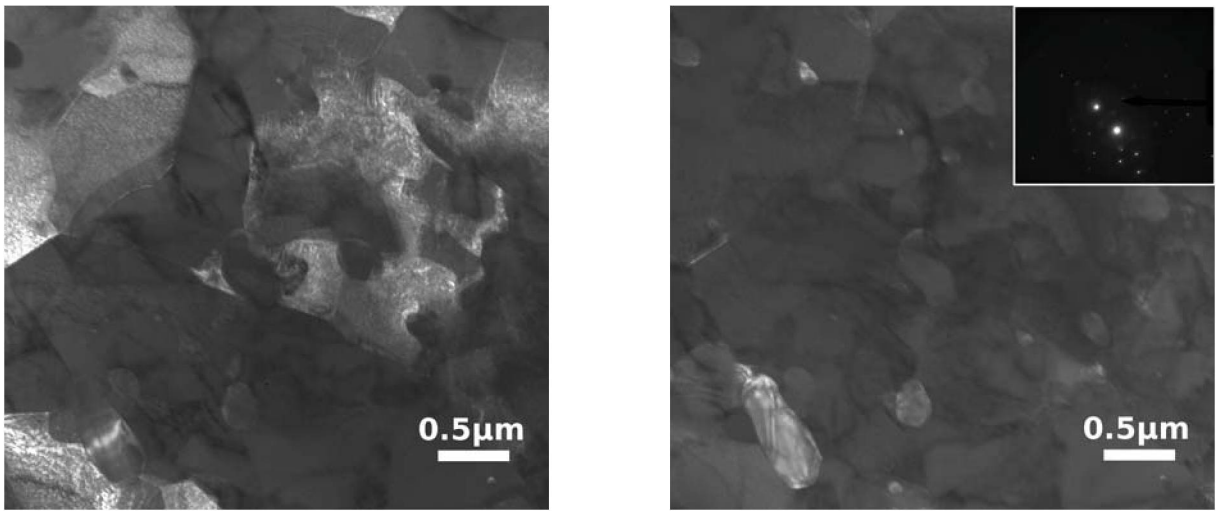

(a) (b)

Fig. 48: In (a) is the BF image of HT-9 ferritic after the proton irradiation at RT at Mag 10,5 kx shown. In (b) is a DF image of the ED-pattern taken where the reflex which is pointed on are corresponding to the carbides occurring bright in the DF image at Mag 10,5 kx.

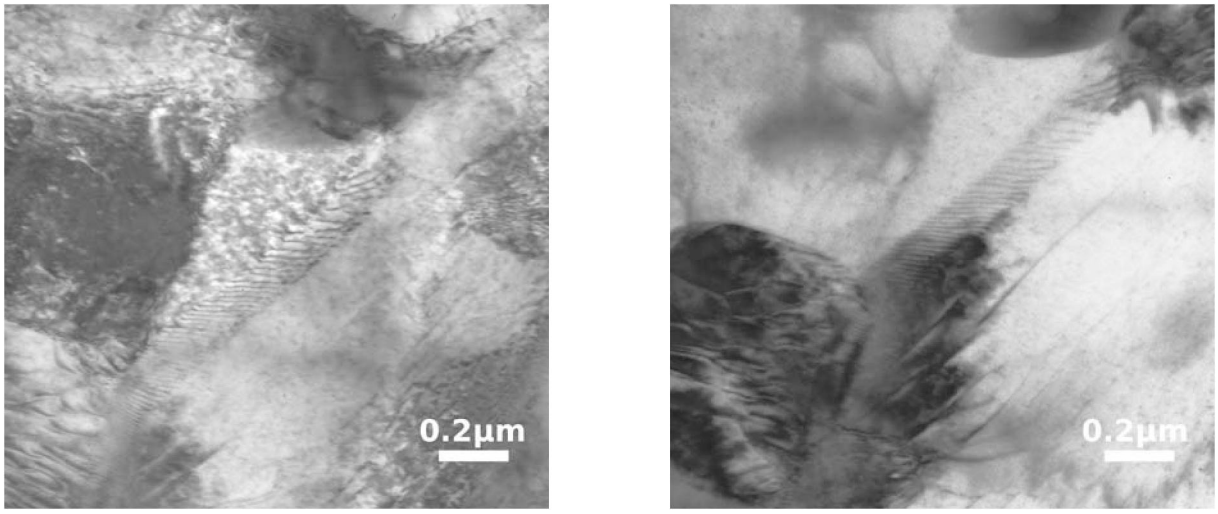

(a) (b)

Fig. 49: Both images were taken at Mag 52 kx but at different tilting angles to determine the thickness of the foil of the HT-9 ferritic steel after the RT irradiation. In (a) the tilting angel was 0° and in (b) the image was taken at +4°.

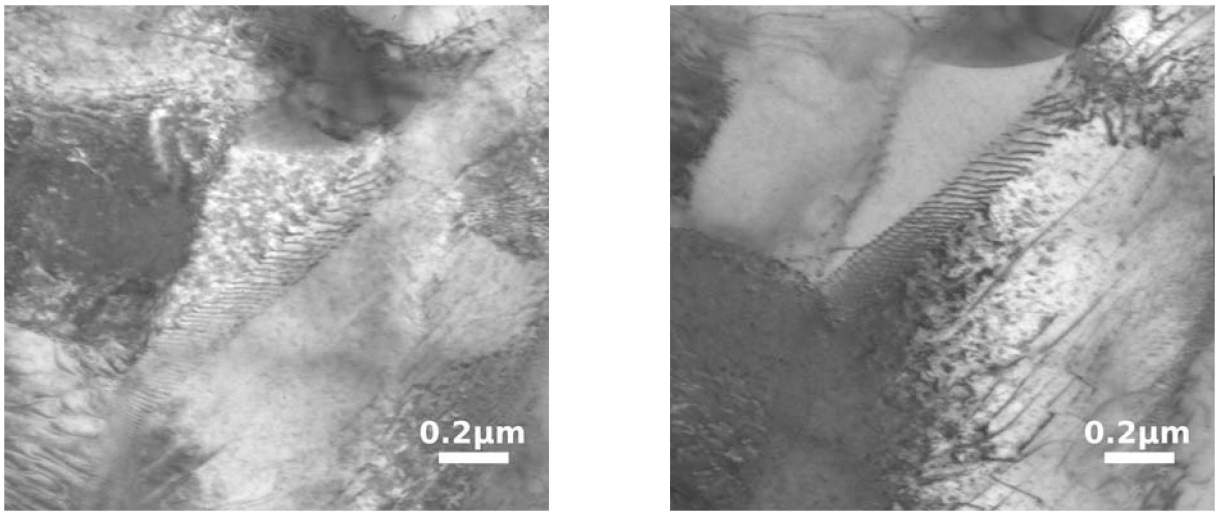

(a) (b)

Fig. 50: Both images were taken at Mag 52 kx but at different tilting angles to determine the thickness of the foil of the HT-9 ferritic steel after the RT irradiation. In (a) the tilting angel was 0° and in (b) the images was taken at +2°.

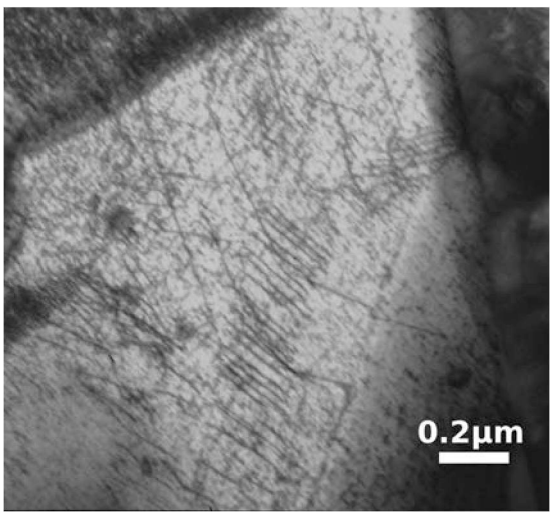

(a)

Fig. 51: Shows the BF image of HT-9 ferritic after the RT irradiation taken at Mag 52 kx from which the dislocation density was evaluated.

Results obtained by TEM after the RT irradiation of HT-9 tempered martensitic steel.

The images in Fig 52, Fig 53 and Fig 54 show the HT-9 martensite structure after the irradiation. Some black spot damage occurred due to the irradiation with protons at RT.

(a)

Fig. 52: Overview of the FIB foil taken at Mag 4400 x, from the HT-9 tempered martensitic steel after the irradiation with protons at RT.

The thickness of the HT-9 tempered martensitic foil after the RT irradiation was measured from the images shown in Fig 55 and lead to a thickness of about 182 nm after evaluating of the lenght of the dislocations at 0° and +4°.

In the images illustrated in Fig 56 it can be seen that there are black spot damage occured caused by the irradiation at room temperature.

From the image shown in Fig 57 the dislocation density of HT-9 tempered martensitic after the RT irradiation was evaluated. The image was taken at a magnification of Mag 52 kx which leads to a total projected length R_p of 3,89 * 10^{-5} m that results in a dislocation densitiy ρ of approximatily 3.04 * 10^{14} m^{-2}.

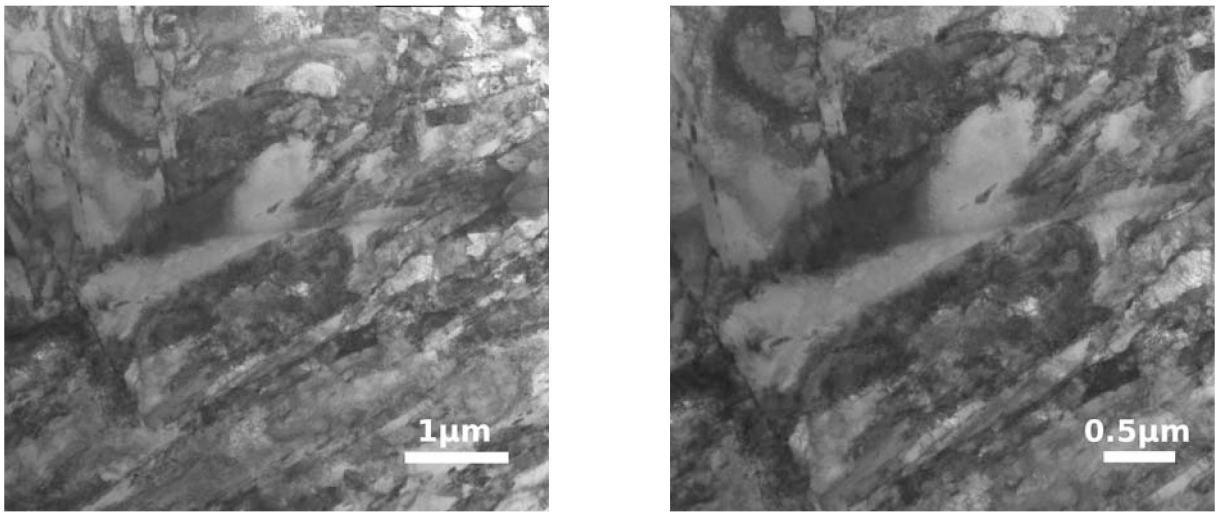

(a) (b)

Fig. 53: The BF images (a) and (b) give an overview of the microstructure of HT-9 tempered martensitic steel after the proton irradiation at RT at (a) Mag 7400 x and (b) Mag 10,5 kx.

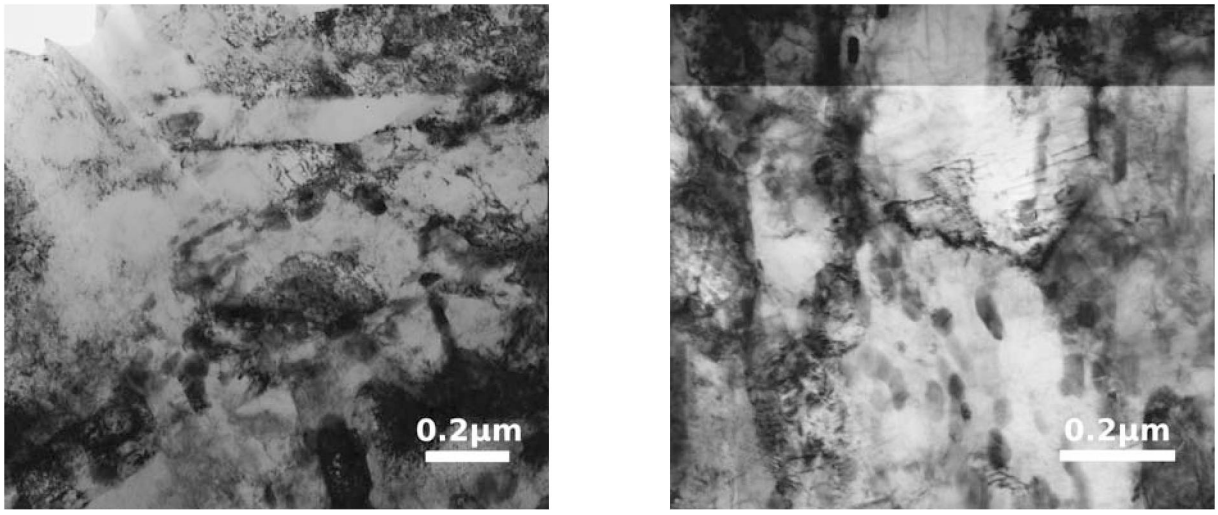

(a) (b)

Fig. 54: The BF images (a) and (b) give an overview of the microstructure of HT-9 tempered martensitic steel after the irradiation with protons at room temperature at. Image (a) is taken at Mag 31 kx and (b) at Mag 42 kx.

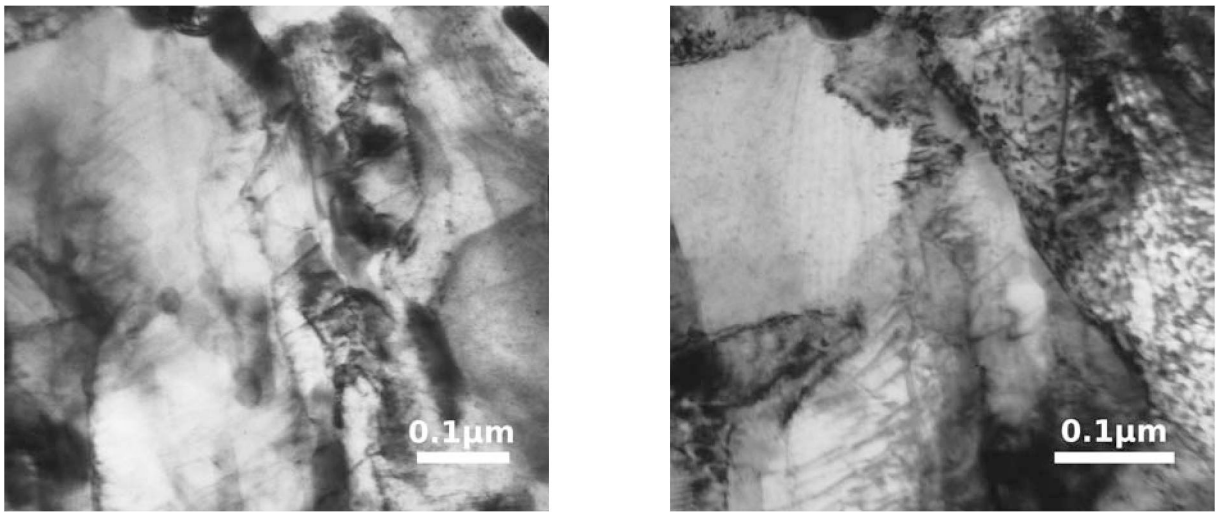

(a) (b)

Fig. 55: Both TEM images, from with protons at RT irradiated HT-9 tempered martensitic steel, were taken at Mag 89 kx but at different tilting angles to determine the thickness of the foil. In (a) the tilting angel was 0° and in (b) the images was taken at +4°.

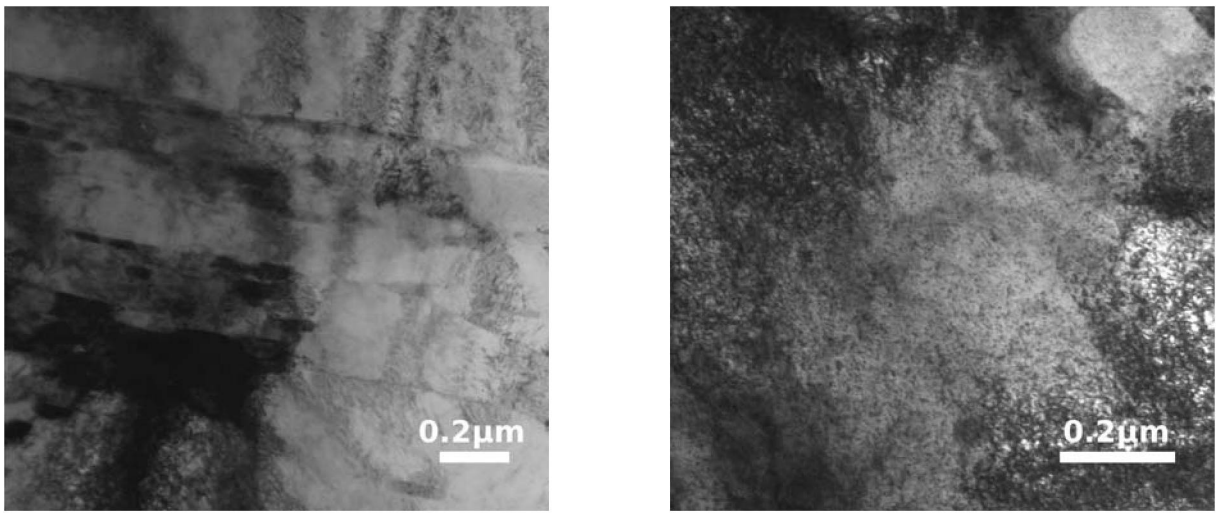

(a) (b)

Fig. 56: The BF images taken at (a) Mag 31 kx and (b) Mag 42 kx show the black spot damage on the HT-9 tempered martensitic caused by the RT irradiation with protons.

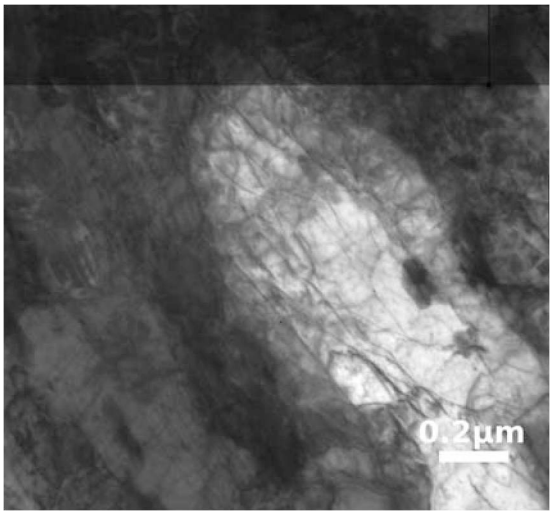

(a)

Fig. 57: Shows an BF image at Mag 52 kx of the HT-9 tempered martensitic steel after the irradiation with protons at RT from which the dislocation density was evaluated.

4.1.6 Discussion of the proton irradiation at RT of the conventional materials

The post indentation AFM revealed that no difference in pile up could be detected between the stopping region and the bulk material. After the He implantation it was found that in the region where the He ions stop significant cracking occurred and no pile up around the nano indents in that particular row of indenst was found while the region around the proton stopping region shows neither. The 1.5 dpa region shows a clear hardness increase of 12 % for the HT-9 tempered martensitic steel and 24 % for the HT-9 ferritic steel after the irradiation with protons at RT. The ion stopping region shows a clear increase in hardness of about 25-30 % for both materials relative to the surrounding area. Due to the TEM examination it was found that damage similar to black spot damage occurred in HT-9 ferritic steel as well as in HT-9 tempered martensitic steel in a depth of about 6 μm where the stopping region of the protons is expected. The evaluation of the dislocation density of HT-9 ferritic steel after the irradiation with protons at RT(ρ = 2,65 * 10^{14} m^{-2}) showed an slight increase in dislocation density compared to the dislocation densitiy evaluated from the pre irradiated sample(ρ = 2,37 * 10^{14} m^{-2}). For HT-9 tempered martensitic steel the evaluated dislocation density was ρ = 3.04 * 10^{14} m^{-2} which showed an increase compared to the pre irradiated sample of HT-9 tempered martensitic steel as the value was ρ = 2.87 * 10^{14} m^{-2}. However it should be pointed out that the difference is in the order of accuracy to determine ρ. As the evaluation of the dislocation density of each material only was performed on one image always close to the area where the thickness of the foil was measured, it is possible that further measurements had to be done to affirm the result of the dislocation density as a variance in the evaluated value can not be excluded. For the RT irradiation with protons it was found that the increase in hardness measured by nanoindentation correlates with an increase in dislocation density for both conventional materials.

4.1.7 Proton irradiation at 300 °C

After the 300 °C irradiation with protons on HT-9 ferritic steel and HT-9 tempered martensitic was completed and nanoindentation on those samples was performed as shown in Fig 58 (a) and (b) as well as after the RT irradiation with protons no cracking was found as due to the Helium implantation at RT. The measurement shown in Fig 61 revealed that the hardness increase in both materials after the irradiation with protons at 300 °C is lower than what was measured in the proton RT experiment. The hardness increased 17 % for the HT-9 ferritic steel and 7 % for the HT-9 tempered martensitic steel . Again the stopping peak region shows a hardness increase of 25-30 % while no difference in pile up formation around the nano indents in the stopping peak region was found.

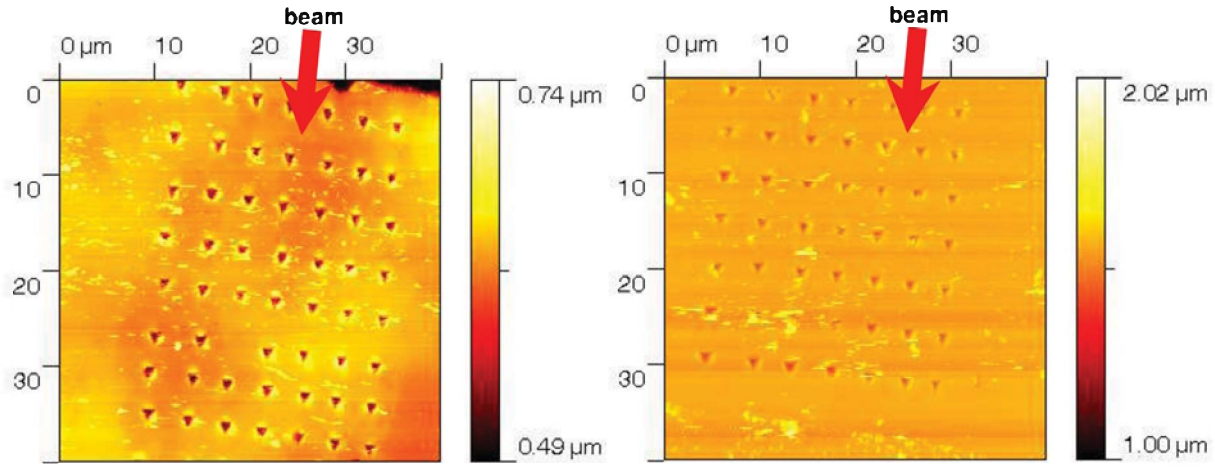

(a) (b)

Fig. 58: (a) The AFM image illustrates the array of indents performed on HT-9 ferritic steel and (b) HT-9 tempered martensitic steel after the irradiation at 300 ℃ with protons.

Fig. 61 presents the hardness data gained from nano indentation after the irradiation up to 300 ℃ in comparison to the hardness data from the He implantation.

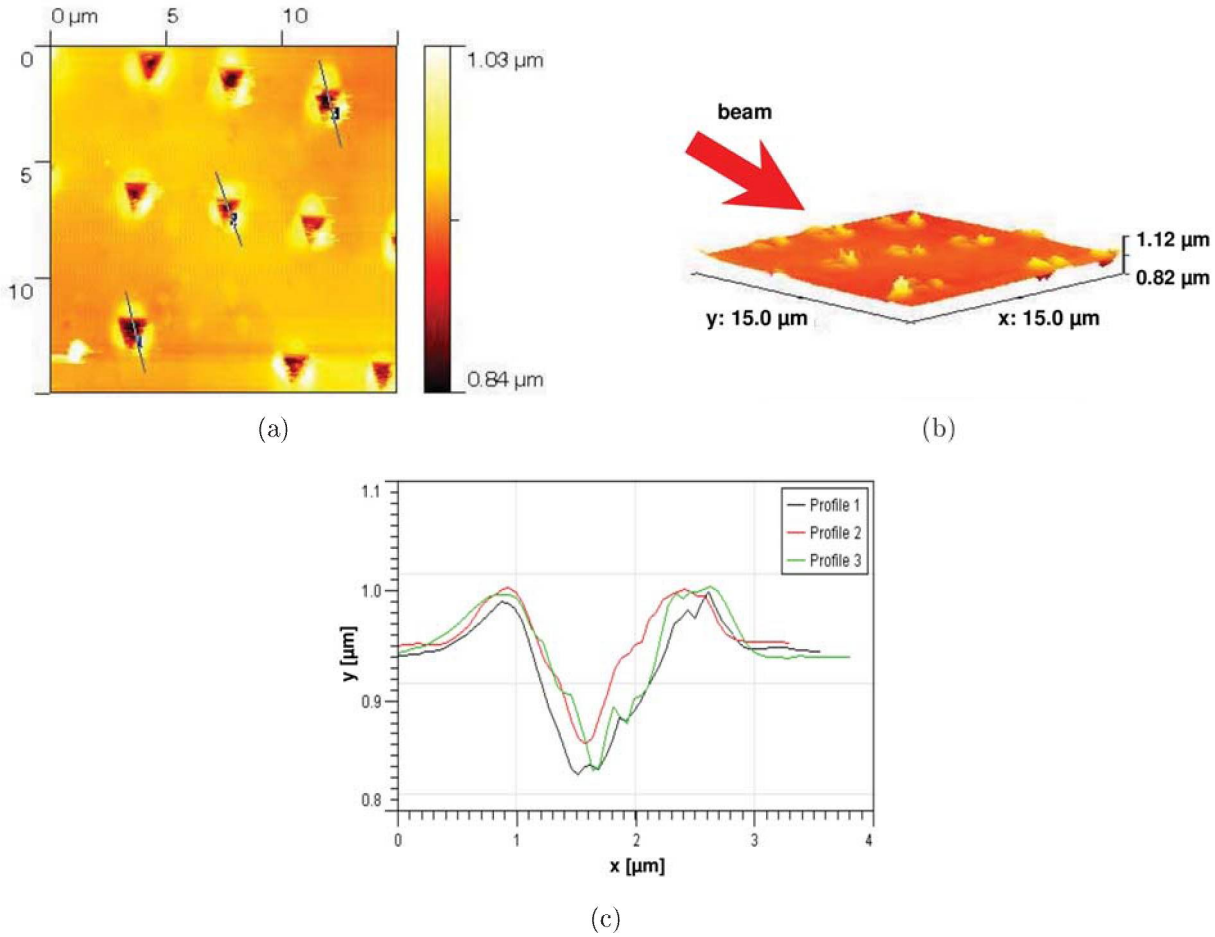

Fig. 59: In AFM image (a) an array of three nanoindents performed on HT-9 ferritic steel after the irradiation at 300 °C with protons is shown. (b) The isometric projection developed from the array in image (a). (c) Depth profil of the indents determined from the AFM image in (a).

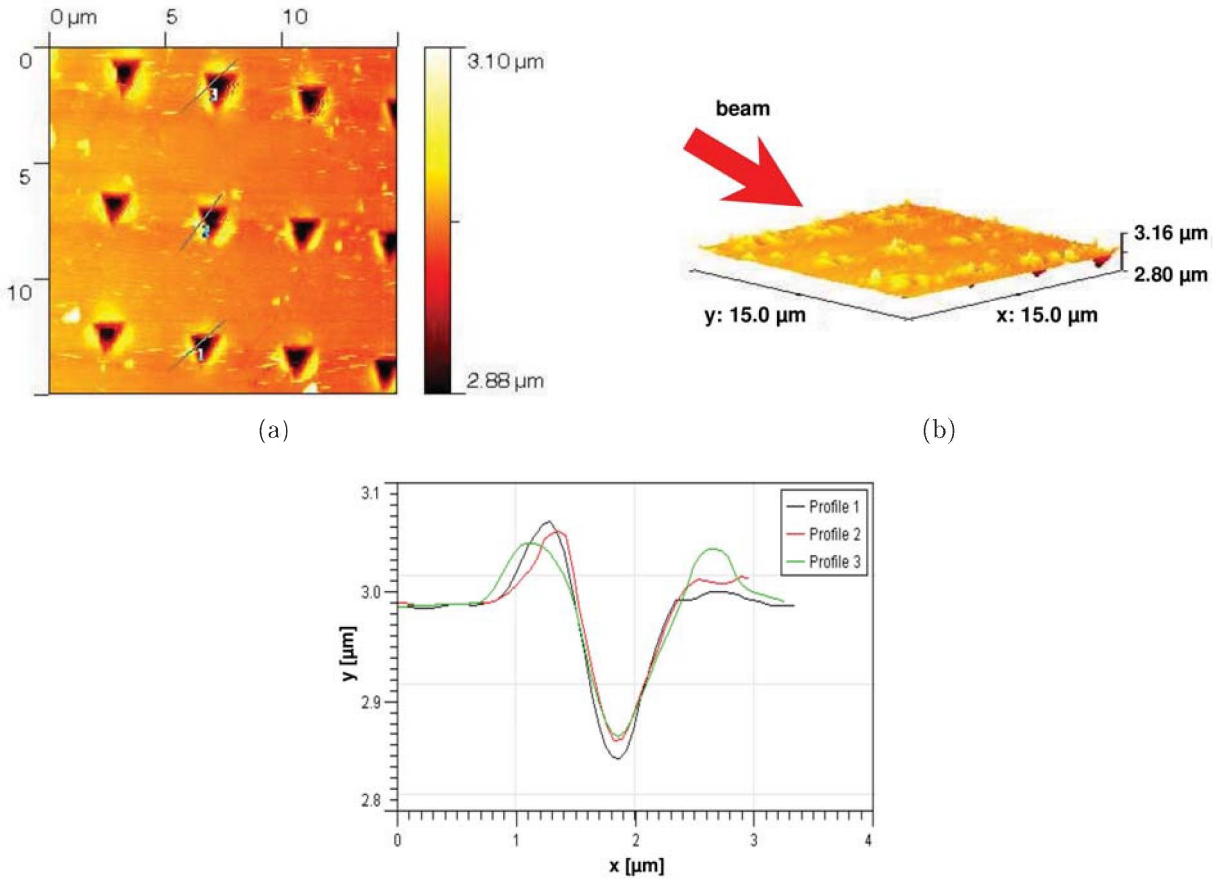

(a) (b)

(c)

Fig. 60: In the AFM image (a) an array of three nanoindents performed on HT-9 tempered martensitic after the irradiation at 300 °C with protons is shown. (b) The isometric projection developed from the array in image (a). (c) Depth profil of the indents determined from the AFM image in (a).

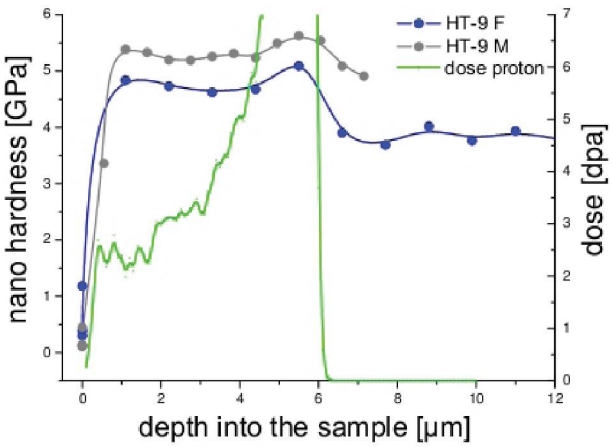

(a)

Fig. 61: Hardness versus depth profile of HT-9 ferritic- and HT- tempered martensitic steel after the irradiation at 300 °C.

Results obtained by TEM after the irradiation at 300 °C of HT-9 ferritic steel.

After the irradiation at 300 °C was completed only on a FIB foil of HT-9 ferritic a characterisation by using TEM was performed. In the overview images shown in Fig 62 and Fig 63 there are black spot damage visible in a depth of about 6 μm where the most irradiation damage is expected.

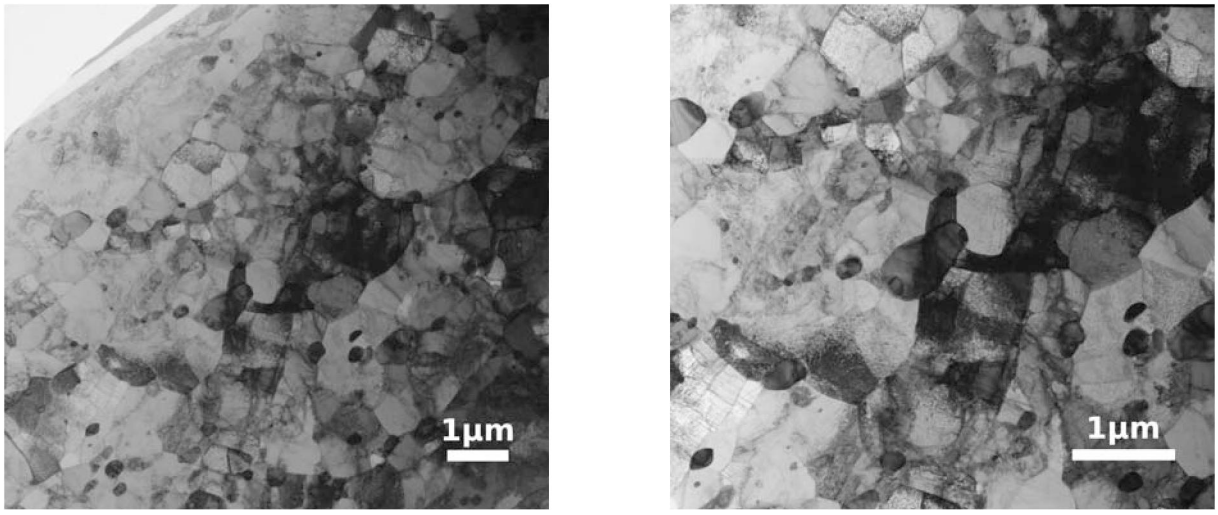

(a) (b)

Fig. 62: The BF images (a) and (b) show an overview of the microstructure of HT-9 ferritic steel at 300 °C at (a) Mag 4400 x and (b) Mag 7400 x.

In Fig 64 the left image is taken in BF mode at Mag 31 kx and the right image is taken in DF mode at Mag 31 kx of a certain spot in the diffraction pattern which corresponds to the carbides shown in the area of the foil so that they appear bright in the DF image.

The images in Fig 65 of the FIB foil of HT-9 ferritic steel after the irradiation with 300 °C leads to a thickness of around 200 nm. Beside the thickness evaluation both images are showing black spot damage caused by irradiation. From both images shown in Fig 65 the dislocation density of the HT-9 ferritic foil after the irradiation at 300 °C was evaluated. The image was taken at a magnification of Mag 31 kx which leads to a total projected length R_p of 3,929 * 10^{-6} m that results in a dislocation densitiy R_p of approximatily 1.79 * 10^{14} m^{-2}.

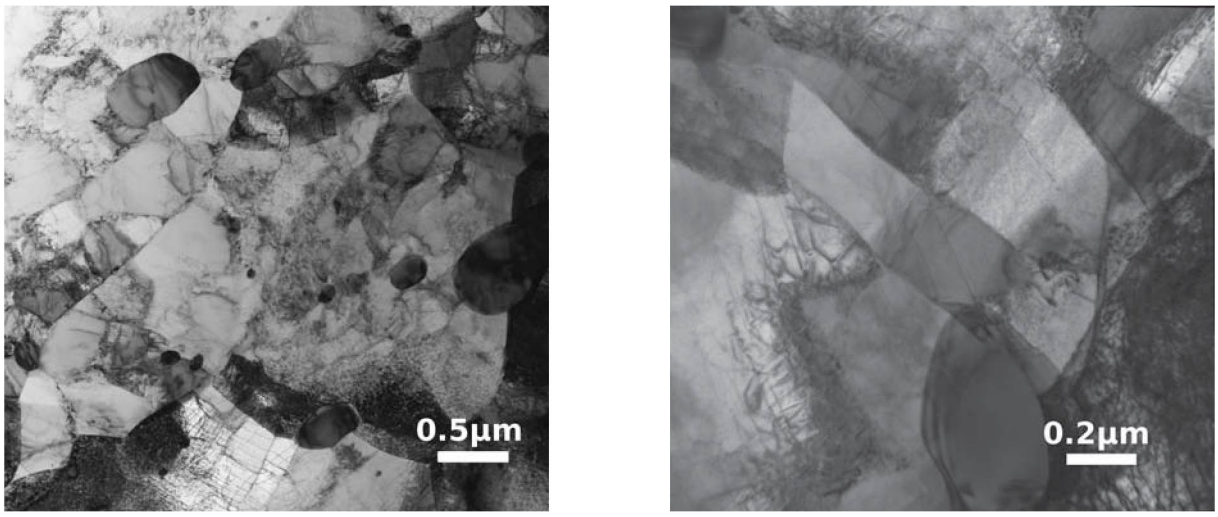

(a) (b)

Fig. 63: The BF images (a) and (b) show an overview of the microstructure of HT-9 ferritic steel at 300 ℃ at (a) Mag 10,5 kx and (b) Mag 52 kx.

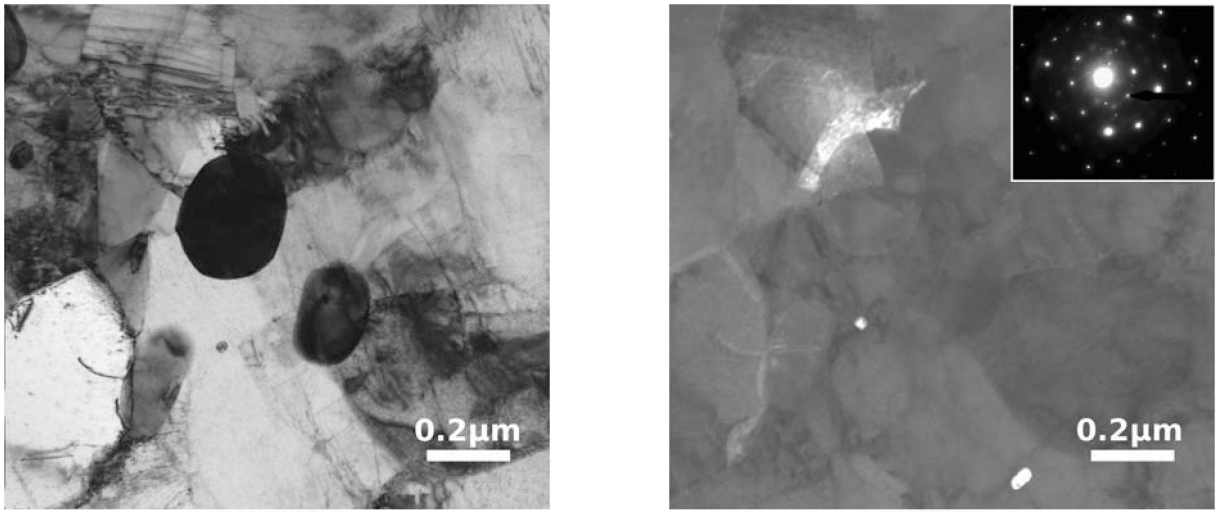

(a) (b)

Fig. 64: (a) showes a BF images of HT-9 ferritic steel after the irradiation with 300 ℃ and (b) illustrates the DF image togehter with the ED-pattern where the reflex pointed on are coming from the carbides appearing bright in the DF image at Mag 31 kx.

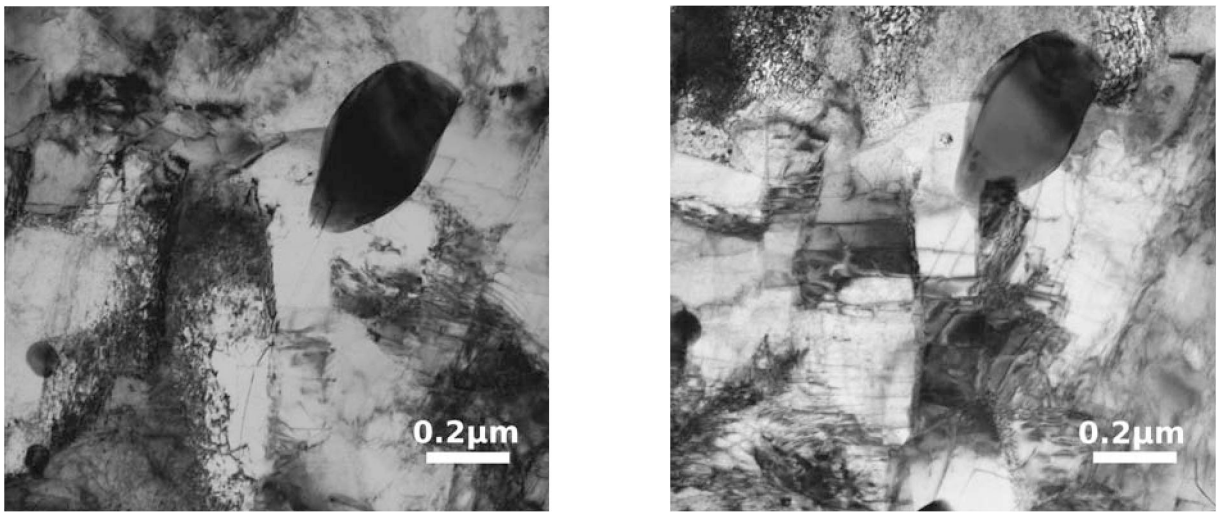

(a) (b)

Fig. 65: Both images were taken at Mag 31 kx but at different tilting angles to determine the thickness of the foil of HT-9 ferritic steel after the irradiation with 300 °C. In (a) the tilting angel was 0° and in (b) the images was taken at +3°. Beside the thickness also the dislocation density was evaluated from both images.

4.1.8 Discussion of the proton irradiation at 300 °C of the conventional materials

The hardness increased of 17 % for the HT-9-ferritic steel and 7 % for the HT-9-tempered martensitic steel respectively whereas the stopping peak region showed an hardness increase of 25-30 % while no difference in pile up formation around the nano indents in the stopping peak region was found. The hardness measurements performed on the proton irradiation at 300 °C showed that with higher irradiation temperature less hardening occured. The fact that the room temperature experiments were performed at 1.5 dpa while the higher temperature experiments were performed at 1 dpa might also play a small role in the strong decrease in radiation induced hardening observed at the higher temperature experiments. But it has been shown in the literature that the hardness difference between 1 and 1.5 dpa is minimal since above 0.5 dpa a gradual increase in hardness is observed [15]. The characterisation by using TEM was performed only on the HT-9 ferritic steel after the proton irradiation at 300 °C but showed in a depth of about 6 μm, where the stopping region of the protons is expected some black spot damage as well as it was found after the proton irradiation at RT. The evaluation of the dislocation density of HT-9 ferritic steel after the irradiation with protons at 300 °C showed a slightly decrease in dislocation density compared to the evaluation of the pre irradiated and the at RT irradiated HT-9 ferritic sample.
For the RT irradiation with protons it was found that the increase in hardness correlates with an increase in dislocation density the same correlation was not found due to the irradiation at 300 °C but it appears that at higher irradiation temperature a strong hardness decrease occurs which results in an addiational decrease in dislocation density but to confirm the evaluated dislocation density further measurments of the thickness and dislocation density at different places of the foil are necessary.

4.1.9 Proton irradiation at 550 °C

After the 550 °C irradiation with protons only on the HT-9 tempered martensitic sample nanoindentation and TEM characterisation was performed. At the 550 °C irradiation temperature only a small hardness increase was found in the irradiated region of the HT-9 tempered martensitic sample as shown in Fig 66 . A 3 % hardness increase was found and no difference in pile up formation around the nano indents in the stopping peak region was found. There was no post AFM examination performed on the 500 °C irradiated HT-9 tempered martensitic sample because the change in hardness was very small.

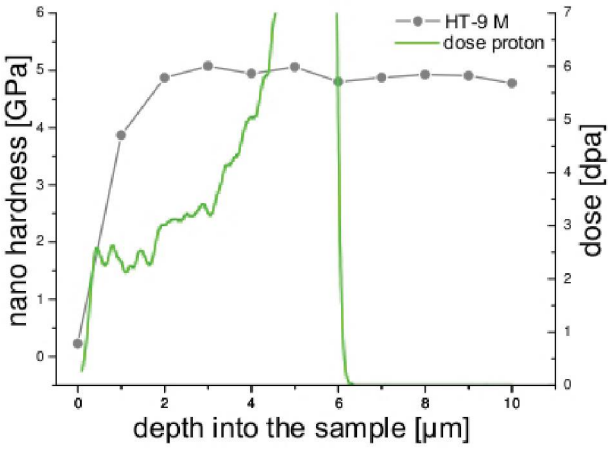

(a)

Fig. 66: (a) The hardness versus depth graph performed on HT-9 tempered martensitic after the irradiation at 550 °C.

Results obtained by TEM after the proton irradiation at 550 °C of HT-9 tempered martensitic steel.

After the 550 °C was completed and the nanoindentation was performed only a single FIB foil of the HT-9 tempererd martensitic sample was prepared and a TEM characterisation done. The BF images in Fig 67 and Fig 68 show an overview of the FIB foil of the HT-9 tempered martensitic microstructure after the 550 °C irradiation.

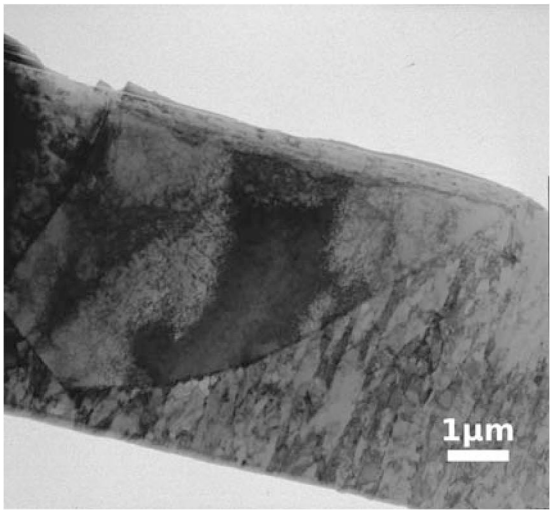

(a)

Fig. 67: The BF image taken at Mag 4400 x gives an overview of microstructure of HT-9 tempered martensitic after the proton irradiation at 550 °C. The irradiation direction is marked with an arrow.

The images in Fig 69 taken at higher magnification (Mag 52 kx) are showing black spot

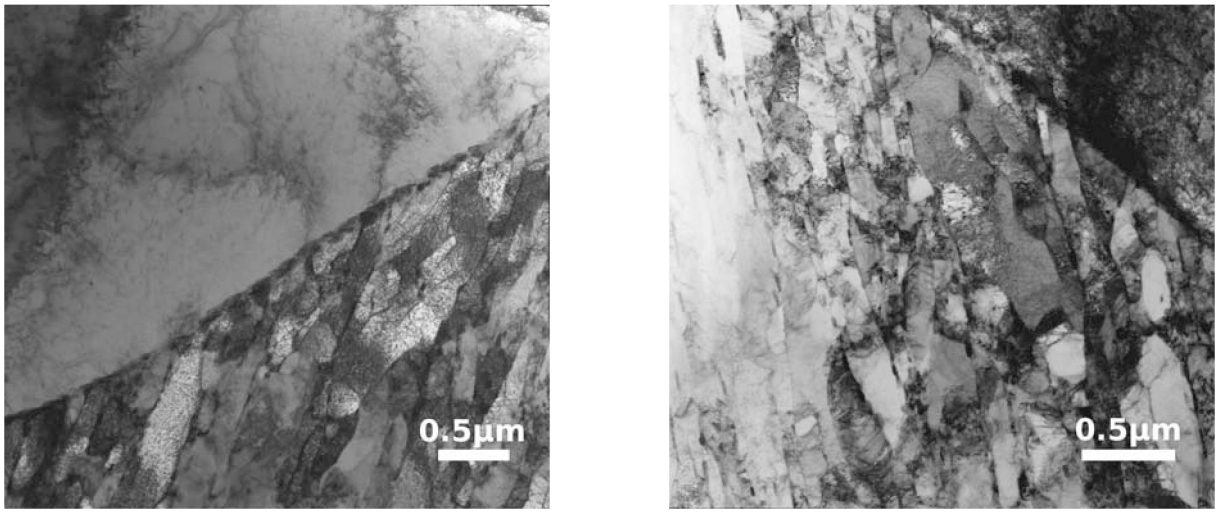

(a) (b)

Fig. 68: The BF images (a) and (b) show an overview of the microstructure of HT-9 tempered martensitic steel irradiated at 550 °C and taken at (a) Mag 10,5kx and (b) Mag 13,5 kx.

damage caused by irradiation with protons at 550 °C of the HT-9 tempered martensitic steel. The black dots appearing in both images are taken from the region of the foil in about 6 μm depth where the most damage caused by irradiation was expected. This damage has to be from the irradiation as the appearance of damage is the same and as it occurred at all three irradiation temperatures (RT, 300 °C and 550 °C) in the same depth where the concentration of the damage is expected.

In both figure, Fig 70 and Fig 71, the left images are taken in BF mode at Mag 52 kx and the right image is taken in DF mode also at Mag 52 kx of a certain spot in the diffraction pattern which corresponds to the carbides seen in this area of the foil so that they appear bright in the DF image.

The thickness of the HT-9 tempered martensitic foil after the 550 °C irradiation was measured from the images shown in Fig 72 and leads to a thickness of about 194 nm after the evaluation of the lenght of the dislocations at $+8°$ and $+14°$.

The images in Fig 73, Fig 74, Fig 75 and Fig 76 are taken at various magnifications and showing a significant damage caused by the irradiation. In the images in Fig 73 as well as in the left image in Fig 74 are so called birds eyes visible which are form a disloacation loop of vacancy arrangements after collapse due to the irradiation and temperature [15].

The image in Fig 75 of HT-9 tempered martensitic steel after the irradiation with 550 °C leads to a projected length R_p of 4,12 * 10^{-5} m which results in a dislocation densitiy ρ of approximatily 3,02 * 10^{14} m^{-2}.

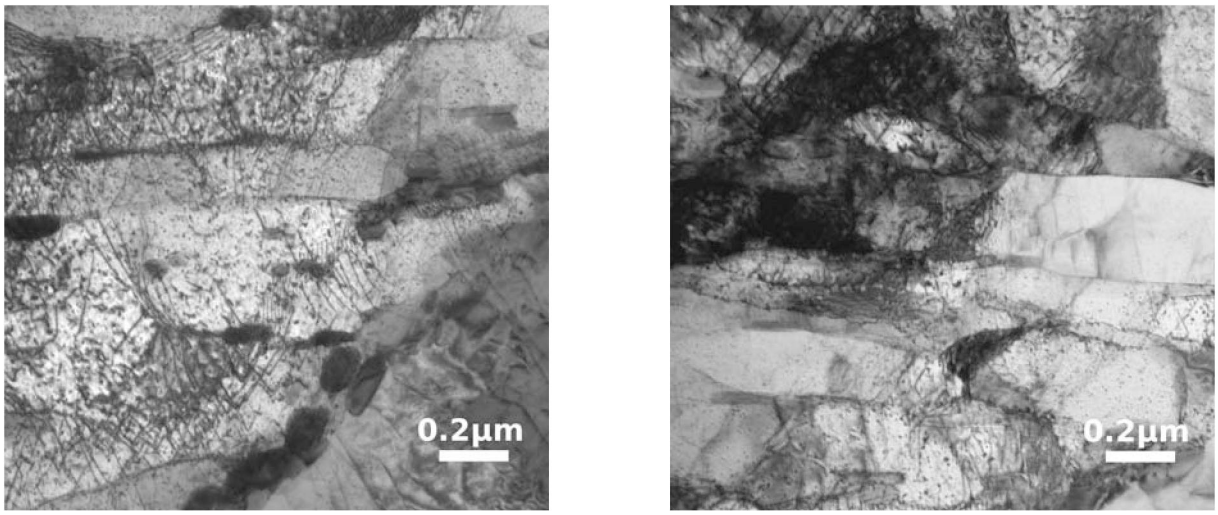

(a) (b)

Fig. 69: The BF images (a) and (b) give an overview of the microstructure of HT-9 tempered martensitic steel irradiated at 550 °C and taken at (a) Mag 52 kx and (b) Mag 52 kx. It illustrates the occurance of the black spot damage.

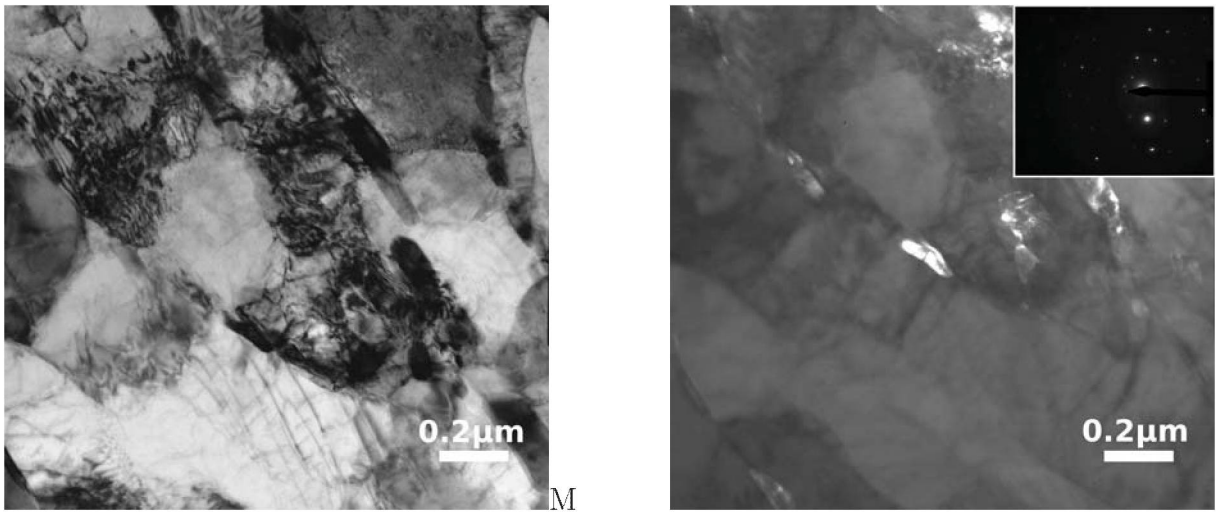

M

(a) (b)

Fig. 70: (a) showes a BF images of HT-9 tempered martensitic steel after the proton irradiation at 550 °C and in (b) the DF image togehter with the ED-pattern placed in the upper right corner where the carbides are occurring bright in the DF image are are coming from the reflex which is pointed in the ED-pattern. Both images are taken at Mag 31 kx.

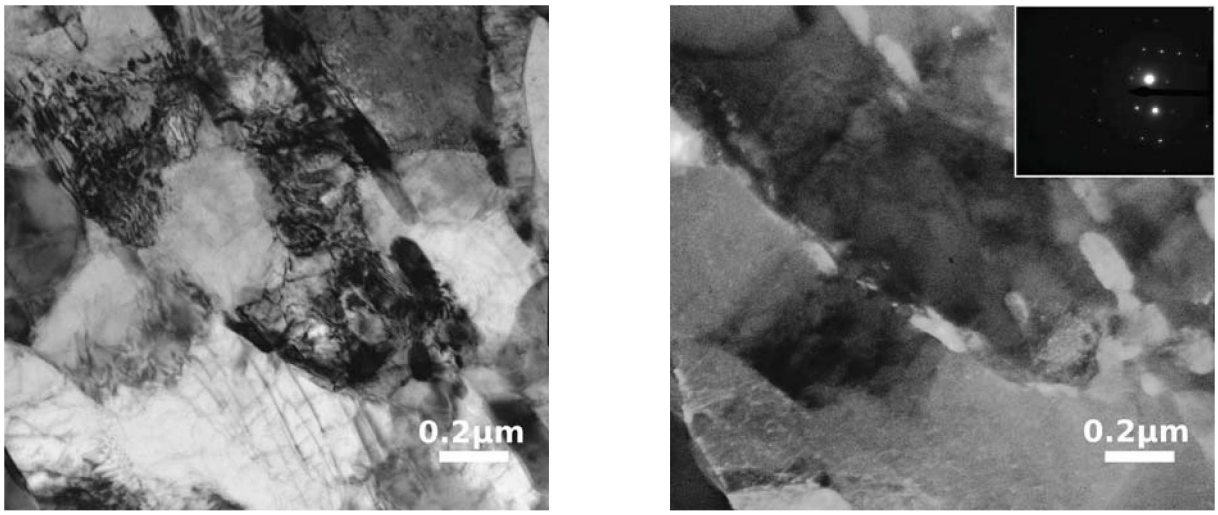

(a) (b)

Fig. 71: (a) showes a BF images of HT-9 tempered martensitic steel after the proton irradiation at 550 °C and in (b) is the DF image togehter with the ED-pattern placed in the upper right corner where the carbides are occurring bright in the DF image are are coming from the reflex which is pointed in the ED-pattern. Both images are taken at Mag 52 kx.

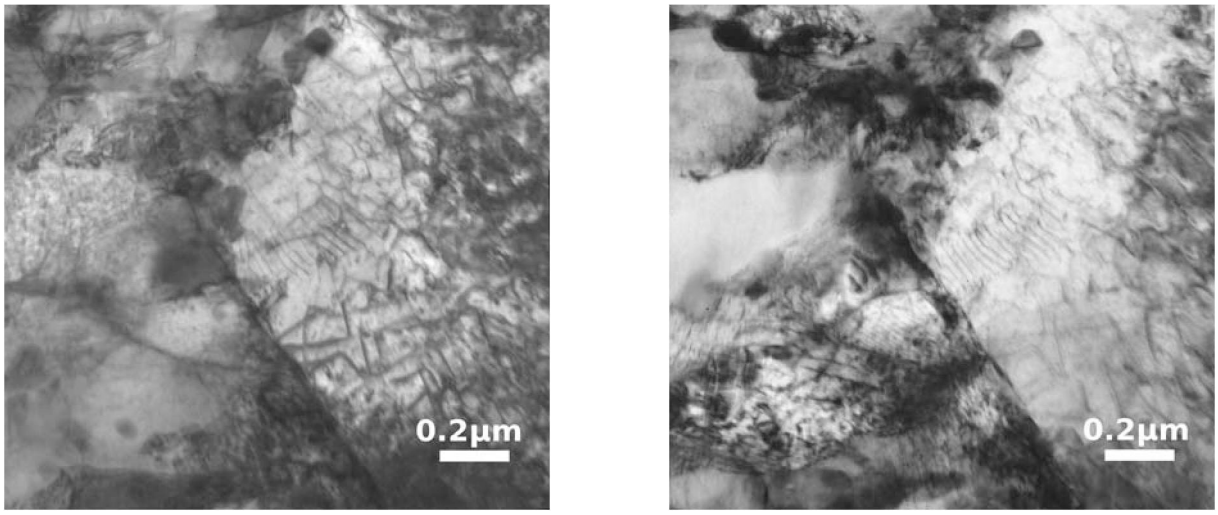

(a) (b)

Fig. 72: Both TEM images of the HT-9 tempered martensitic steel after the 550 °C irradiation were taken at Mag 31 kx but at different tilting angles to determine the thickness of the foil. In (a) the tilting angel was +8° and in (b) the images was taken at +14°.

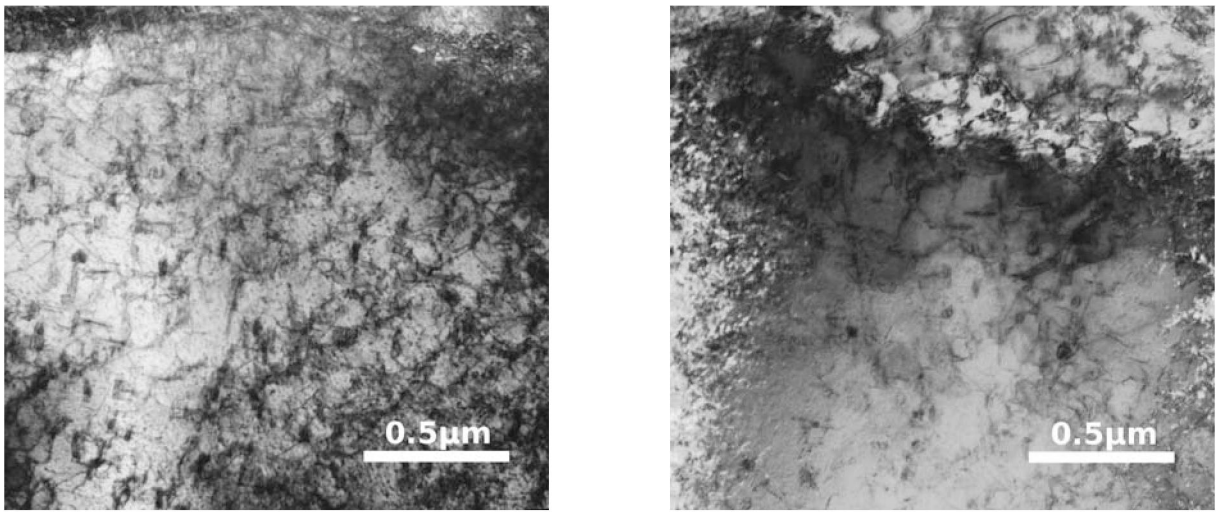

(a) (b)

Fig. 73: The BF images (a) and (b) show an overview of the microstructure of HT-9 tempered martensitic steel after the proton irradiation at 550 ℃and is an illustration of the formed bird eyes during the irradiation. Image (a) was taken at Mag 21 kx and (b) at Mag 21 kx.

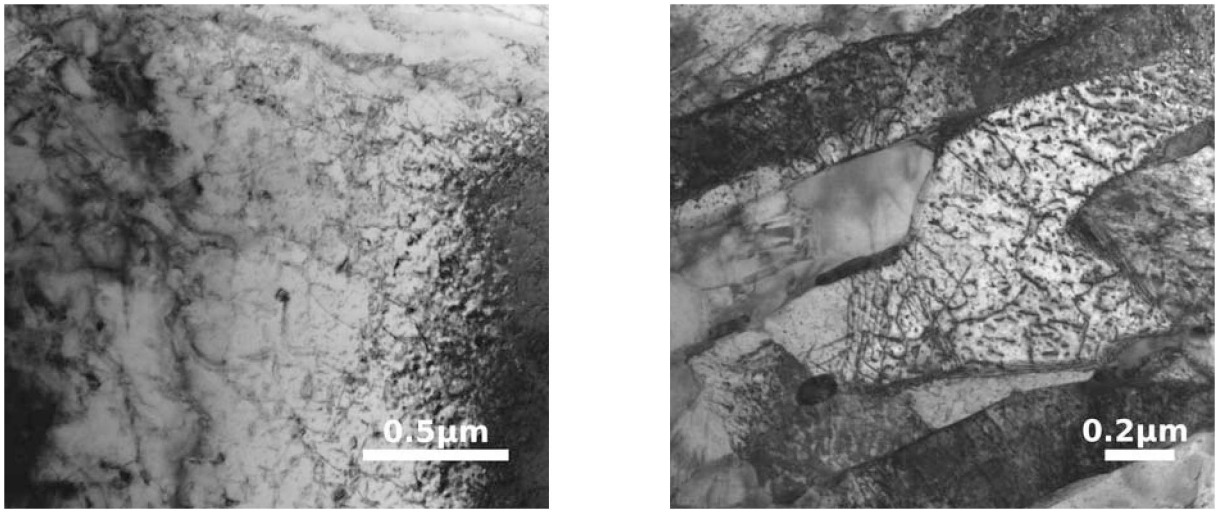

(a) (b)

Fig. 74: The BF images (a) and (b) show an overview of the microstructure of HT-9 tempered martensitic steel after the proton irradiation at 550 ℃. Image (a) was taken at Mag 21 kx and (b) at Mag 52 kx.

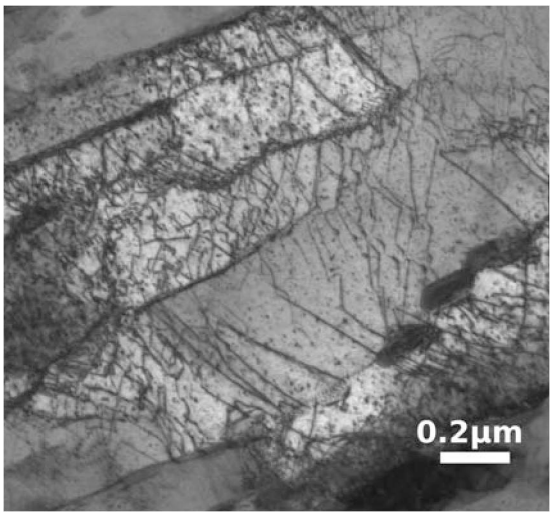

(a)

Fig. 75: The BF image is taken at Mag 52 kx and shows an overview of the microstructure of HT-9 tempered martensitic steel irradiated at 550 °C and was used to evaluate the dislocation density of the foil.

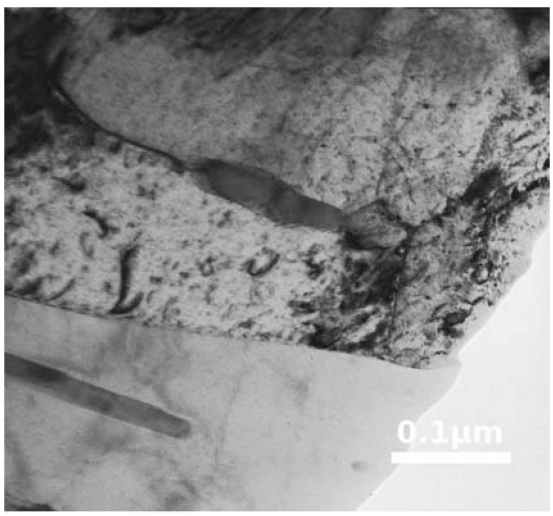

(a)

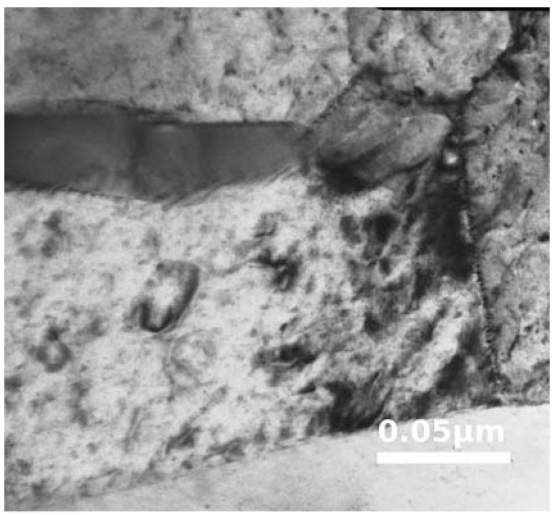

(b)

Fig. 76: The BF images (a) and (b) show the microstructure of HT-9 tempered martensitic steel after the irradiation at 550 °C. Image taken at (a) Mag 89 kx and (b) Mag 200 kx.

4.1.10 Discussion of the proton irradiation at 550 °C of the conventional materials

The hardness measurements performed on the proton irradiation at 550 °C showed that with higher irradiation temperature less hardening occurs. Also no cracking and no disappearance of the pile up around the nano indents was found as it occurred due to the Helium implantation. The fact that the room temperature experiments were performed at 1.5 dpa while the higher temperature experiments were performed at 1 dpa might also play a small role in the strong decrease in radiation induced hardening observed at the higher temperature experiments. But it has been shown in the literature that the hardness difference between 1 and 1.5 dpa is minimal since above 0.5 dpa a gradual increase in mechanical properties is observed. The characterisation by using TEM was performed only on the HT-9 tempered martensitic steel after the proton irradiation at 550 °C but showed in a depth of about 6 μm where the stopping region of the protons is expected black spot damage. The evaluation of the dislocation density of HT-9 tempered martensitic steel after the irradiation with protons at 550 °C showed an increase in dislocation density ($\rho = 3.02 * 10^{14}$ m^{-2}) compared to the dislocation densitiy evaluated from the pre irradiated (ρ = 2,87 * 10^{14} m^{-2}) HT-9 tempered martensitic sample but also a slightly decrease compared to the HT-9 tempered martensitic sample after the proton irradiation at RT (ρ = 3,04 * 10^{14} m^{-2}). It appears that at higher irradiation temperatures a strong hardness decrease occurs caused by recovery effects at elevated temperature such as the recombination of radiation induced defects.

4.2 MA956 and MA957

4.2.1 Pre Irradiation

Results obtained by Microhardness

The microhardness measurements were performed only on the pre irradiated samples by using a Buehler Micromet 5100 series(version 2.10) together with the Buehler OmniMet MHT software which measures the Vickers imprint optically. A series of 5 imprints each with a force of 200g, 500g and 1000g on each material was taken and measured at a magnification of 500x to determine the microhardess of HV0.2, HV0.5 and HV1. The given values are the avarage of 5 indents. For MA956 the microhardness is between 259-268 as shown in Table 7.

The microhardness data for MA957, are listed in in Table 8 and the average value of 5 indents is between 346- 360.

Table 7: Microhardness of MA956

force	1.result	2.result	3.result	4.result	5.result	average value
200g	265,5	269,0	266,6	269,0	267,8	HV0.2 = 267,6
500g	265,5	259,7	263,3	259,0	259,0	HV0.5 = 261,3
1000g	261,7	259,7	257,2	262,2	252,7	HV1 = 258,7

Table 8: Microhardness of MA957

force	1.result	2.result	3.result	4.result	5.result	average value
200g	345,3	347,7	344,6	345,3	348,5	HV0.2 = 346,3
500g	351,0	356,7	355,6	355,6	355,6	HV0.5 = 354,9
1000g	359,2	366,7	357,4	355,6	359,2	HV1 = 359,6

Results obtained by TEM of the pre irradiated MA956.

The BF images shown in Fig 77 and Fig 78 are taken at several magnifications and do show the microstructure of the pre irradiated MA956.

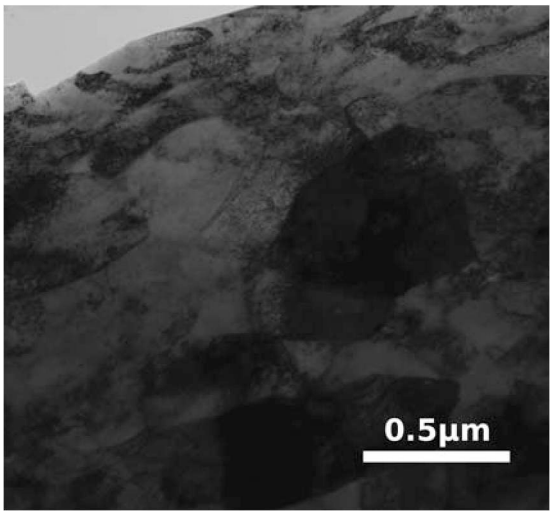

(a)

Fig. 77: The BF image shows an overview of the microstructure of the pre irradiated MA956 taken at Mag 21kx.

In the images shown in Fig 81 the ODS particle are distributed in the matrix and do appear as dark spots espacially in the right image (b).

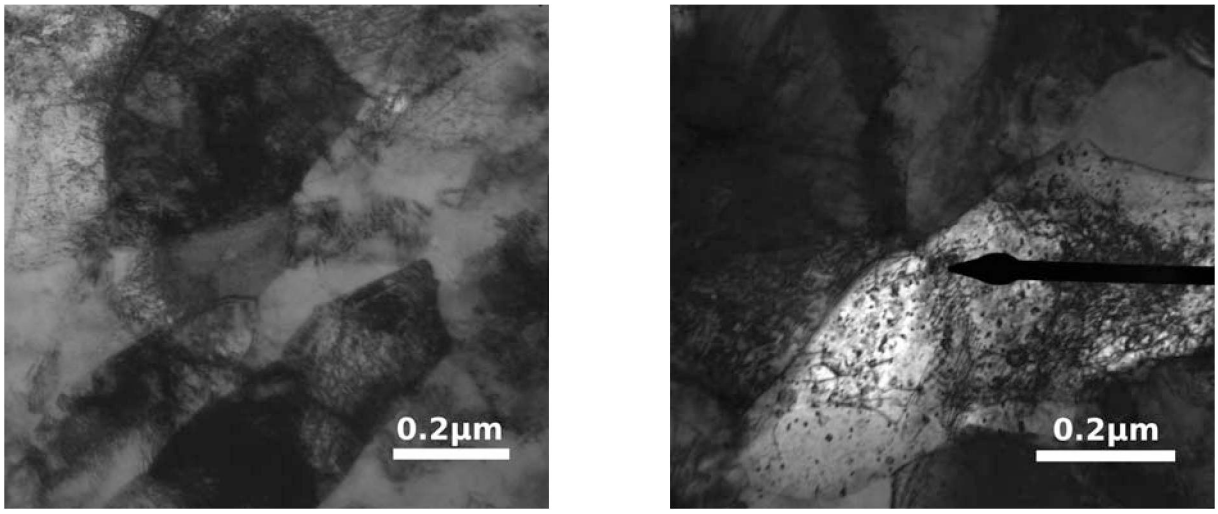

(a) (b)

Fig. 78: The BF images (a) and (b) show an overview of the microstructure of the pre irradiated MA956 taken at (a) Mag 31kx and (b) Mag 52 kx.

The nanosized ODS particles are distributed in the matrix and are shown in Fig 79 in the right image (DF image) where they appear bright.

The thickness of the MA956 foil was measured from the images shown in Fig 80 and lead to a thickness of about 162 nm after evaluating the lenght of the dislocations at 0° and +13°.

From the BF image illustrated in Fig 81 taken at a Mag 52 kx from the pre-irradiated MA956 the total projected length R_p is 2,38 * 10^{-5} m which results in a dislocation densitiy ρ of approximatily 2,09 * 10^{14} m^{-2}.

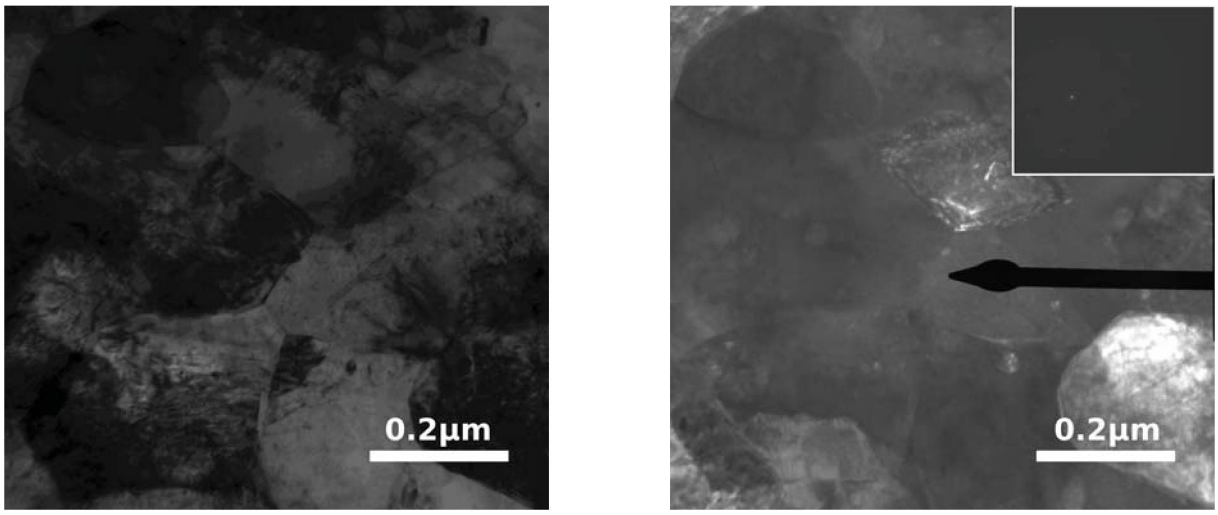

(a) (b)

Fig. 79: (a) showes a BF image and in (b) the DF image togehter with the ED-pattern taken at Mag 52 kx of MA956 where the reflex pointed on are coming from an ODS particle which appear bright in the DF image.

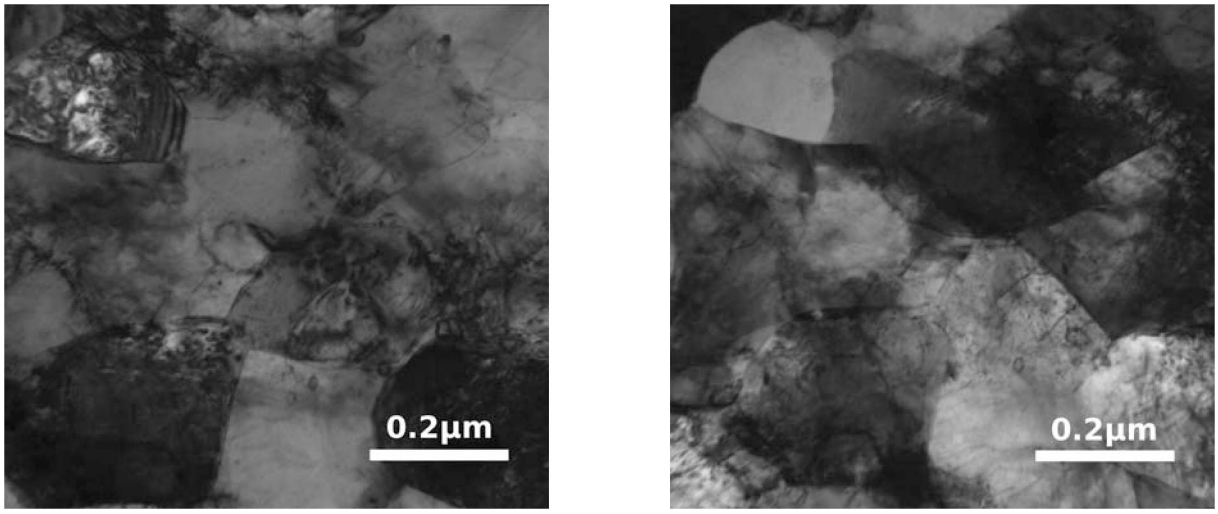

(a) (b)

Fig. 80: Both TEM images of MA956 were taken at Mag 52 kx but at different tilting angles to determine the thickness of the foil. In (a) the tilting angel was 0° and in (b) the images was taken at +13°.

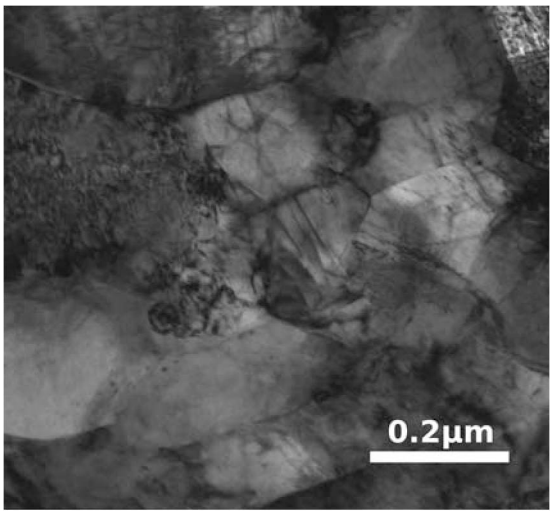

(a)

Fig. 81: The image was taken at Mag 52 kx and show dislocations in two beam condition.

Results obtained by TEM of the pre irradiated MA957

In Fig 82 the TEM image shows the ODS particles with an average size of 20 to 50 nm at a low magnification.

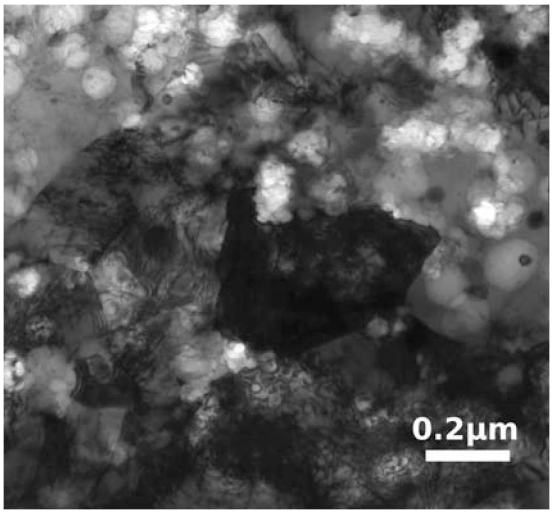

(a)

Fig. 82: The BF image gives an overview of the microstructure of MA957 at Mag 31kx and shows the nanosized ODS partical distributed.

In the ED-pattern shown in Fig 83 and Fig 84 the reflexes pointed on are coming from an ODS particle, they are distributed in the matrix and do appear bright in DF the images.

The thickness of the MA957 foil was measured from the images shown in Fig 85 and lead to a thickness of 182 nm after evaluating the lenght of the dislocations.

Close to the area where the thickness measurment was performed the image in Fig 86 was taken and shows dislocations in two beam condition from which the dislocation density was calculated by using the equation (15) in chapter 3. The resultant total projected length R_p is 3,22 * 10^{-5} m which leads to a dislocation densitiy ρ of approximatily 2,51 * 10^{14} m^{-2}.

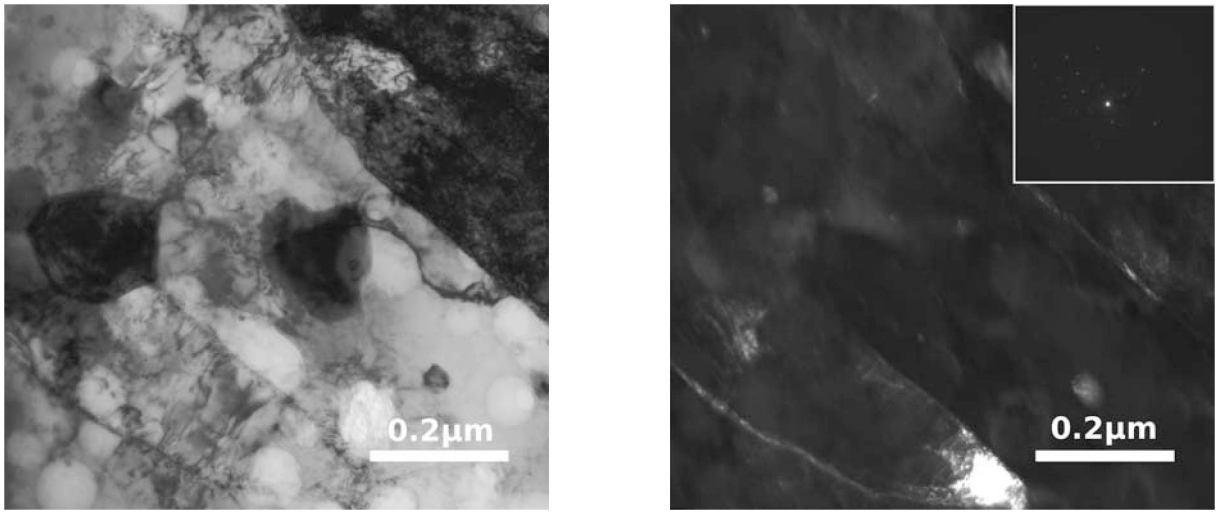

(a) (b)

Fig. 83: (a) showes a BF images and in (b) the DF image togehter with the ED-pattern where some reflexes are coming from the bright shining carbides at Mag 52 kx.

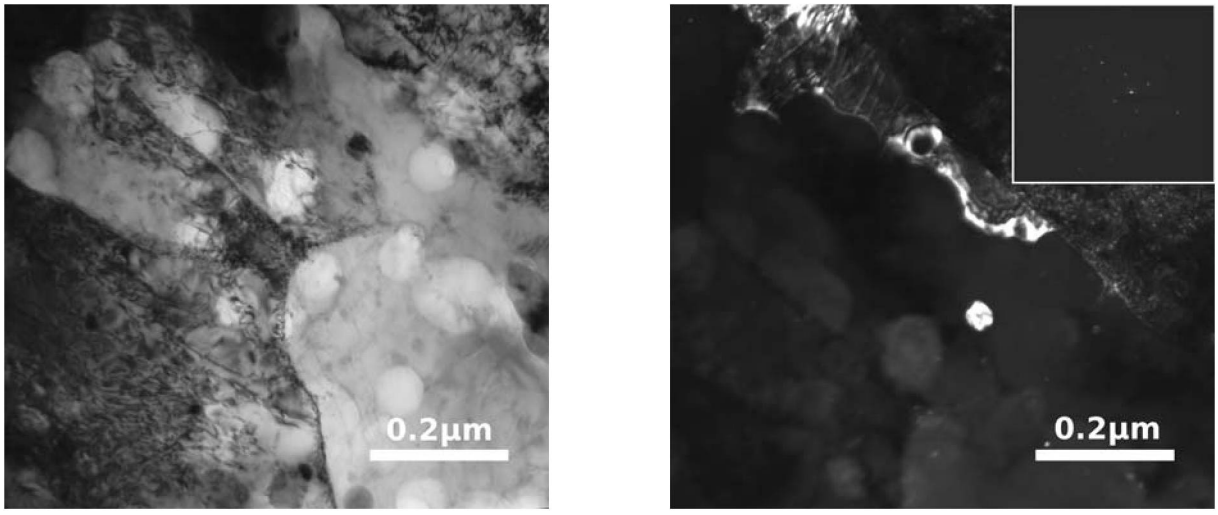

(a) (b)

Fig. 84: (a) showes a BF images of MA957 and in (b) the DF image togehter with the ED-pattern where some reflexes are coming from the bright shining carbides at Mag 52 kx.

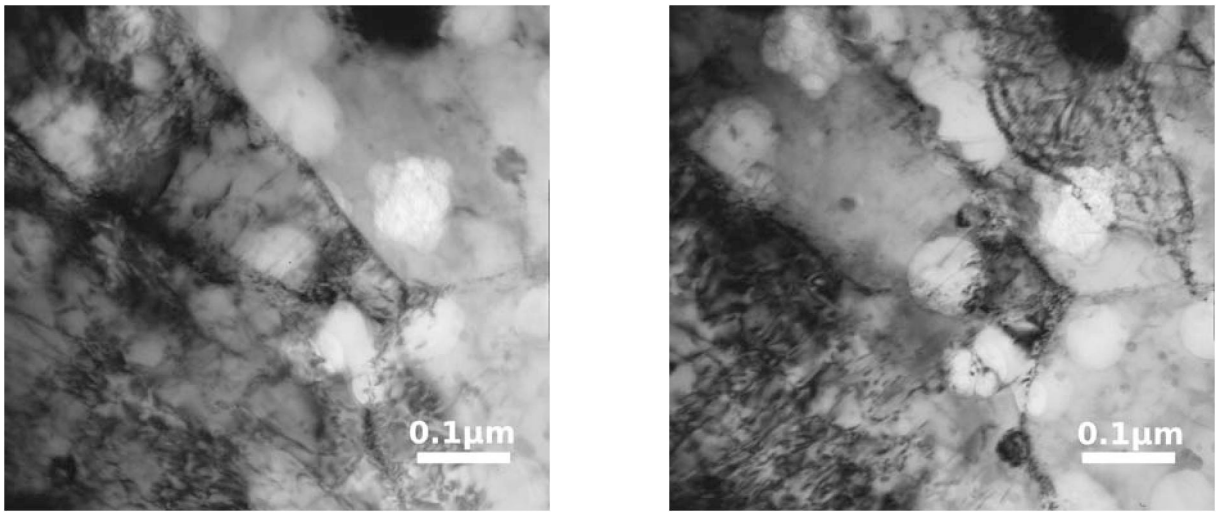

(a) (b)

Fig. 85: Both images of MA957 were taken at Mag 69 kx but at different tilting angles to determine the thickness of the foil. In (a) the tilting angel was -2° and in (b) the images was taken at -13°.

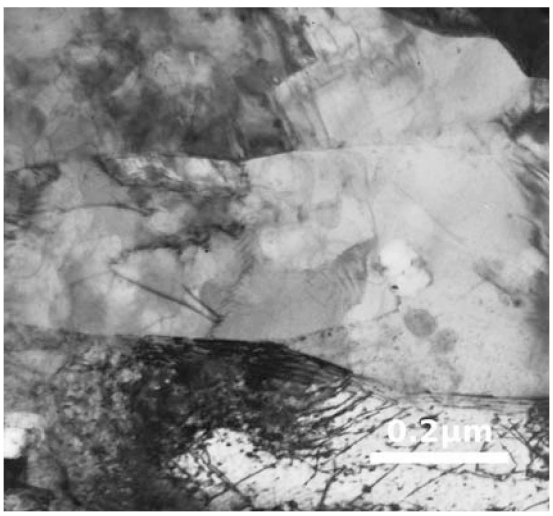

(a)

Fig. 86: The BF image of MA957 taken at Mag 52 kx shows dislocations in two beam condition from which the dislocation density was evaluated.

4.2.2 Discussion of the pre irradiated advanced materials

TEM characterisation of the pre irradiated advanced materials showed their microstructure where the nanosized ODS particles are randomly distributed in the matrix. The effect of those 20-50 nm ODS particles results in a significant higher microhardness of HV0.2 = 267 for MA956 and HV0.2 = 346 for MA957 compared to the microhardness of the HT-9 steels of HV0.2 = 198 for HT-9 ferritic or of HV0.2 = 255 for HT-9 tempered martensitic steel. Beside the high value in hardness the dislocation density ρ of 2,09 * 10^{14} m^{-2} for MA956 and 2,51 * 10^{14} m^{-2} for MA957 is high as well. The implantation with Helium at room temperature (RT) and the irradiation with protons at RT, 300 °C and 550 °C will reveal if an additional increase in hardness and dislocation densitiy due to the radiation damage will occur.

4.2.3 Helium implantation at room temperature

After the room temperature irradiation on MA965 and MA957 was completed, the nanoindentation on those samples was performed. It was found that due to the high He implantation in the ion stopping range the samples showed significant blistering. The 3 dpa region of the samples did not show a significant hardening as shown in Fig 90 and Fig 91.

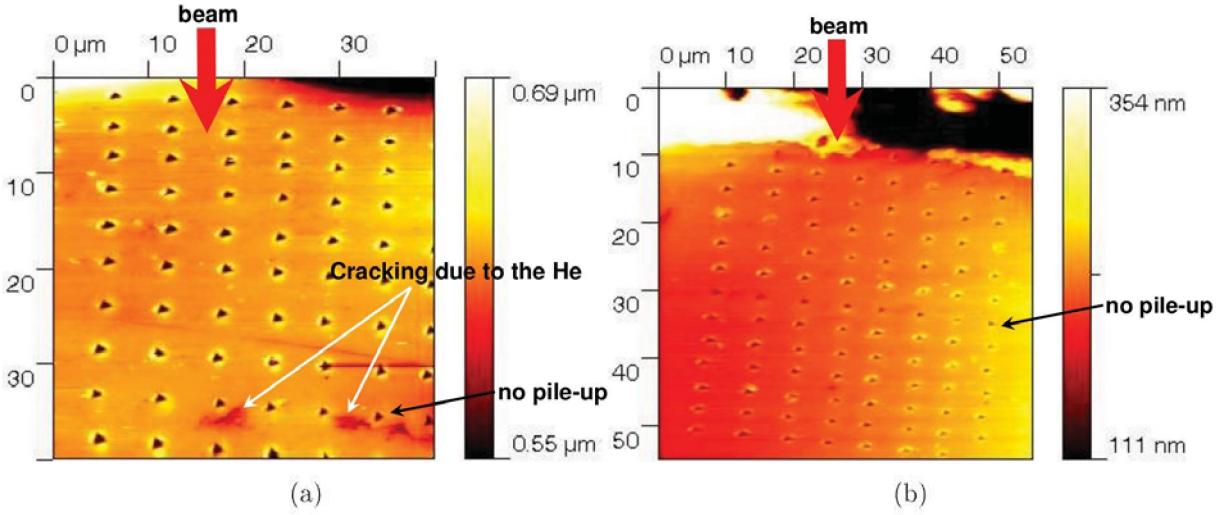

Fig. 87: (a) The image illustrates the array of indents performed on MA956. (b) Nanohardness performed on MA957 after the implantation with Helium at RT.

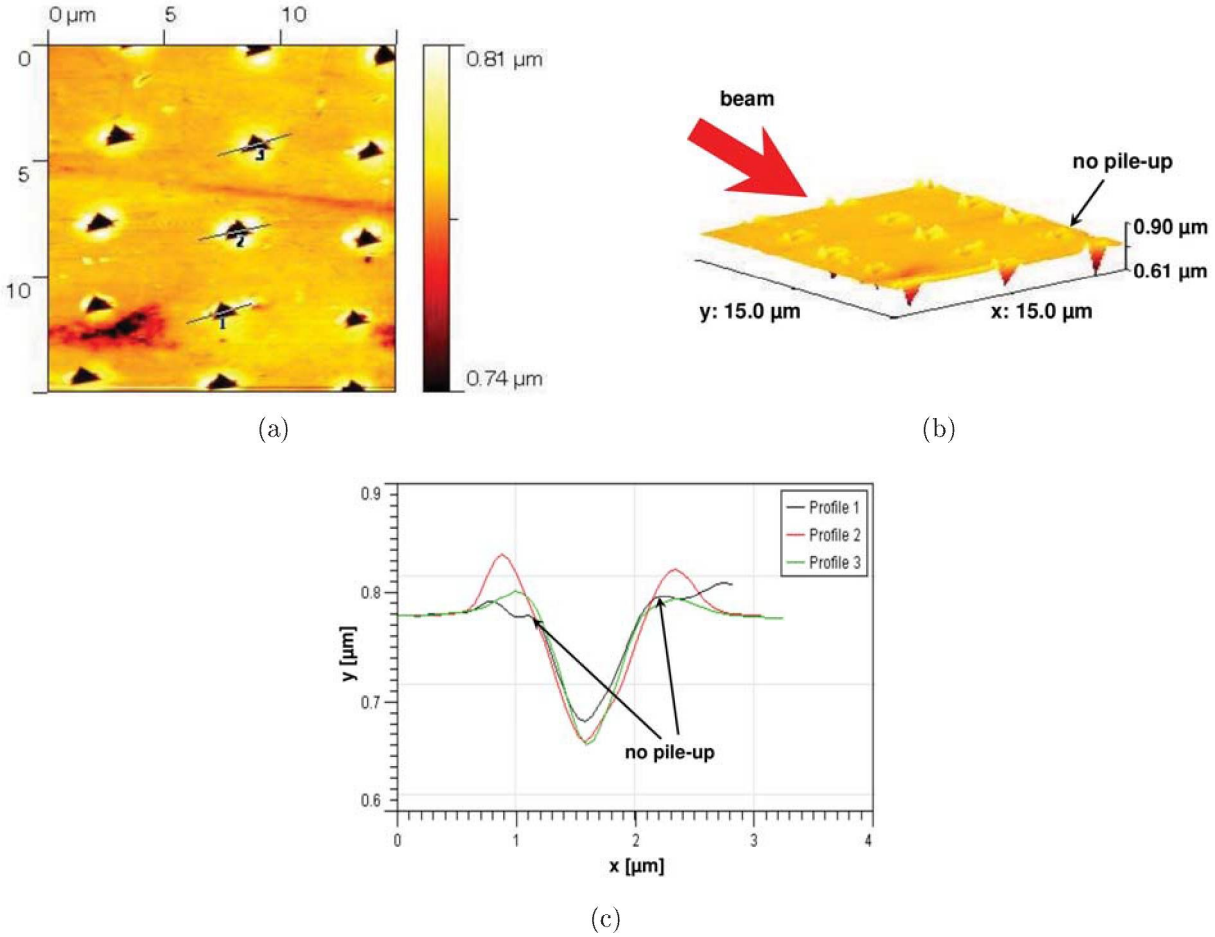

Fig. 88: In image (a) an array of three nanoindents performed on MA956 after the implantation with Helium at RT is shown. (b) The isometric projection developed from the array in image (a). (c) Depth profil of the indents determined from the isometric projection in (a).

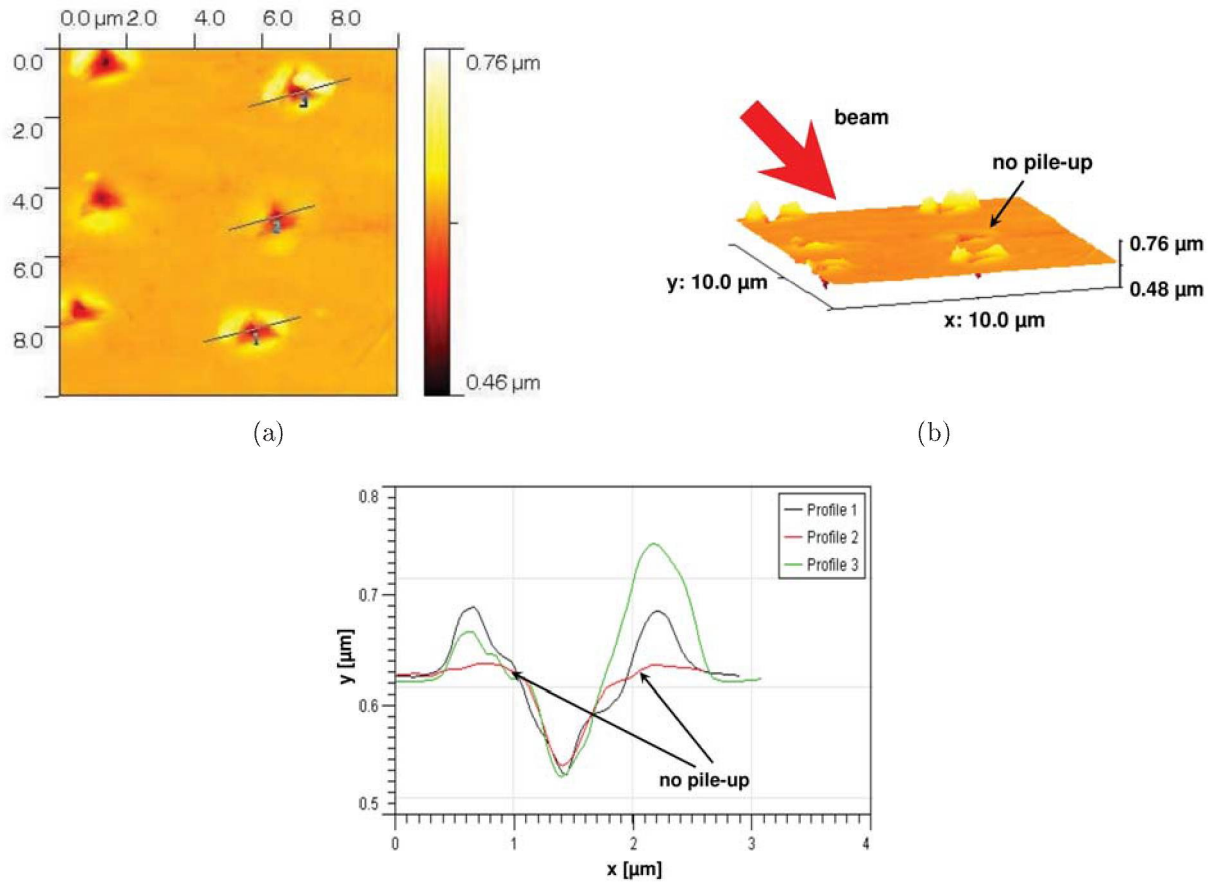

Fig. 89: In image (a) an array of three nanoindents performed on MA957 after the implantation with Helium at RT is is shown. (b) The isometric projection developed from the array in image (a). (c) Depth profil of the indents determined from the AFM image in (a).

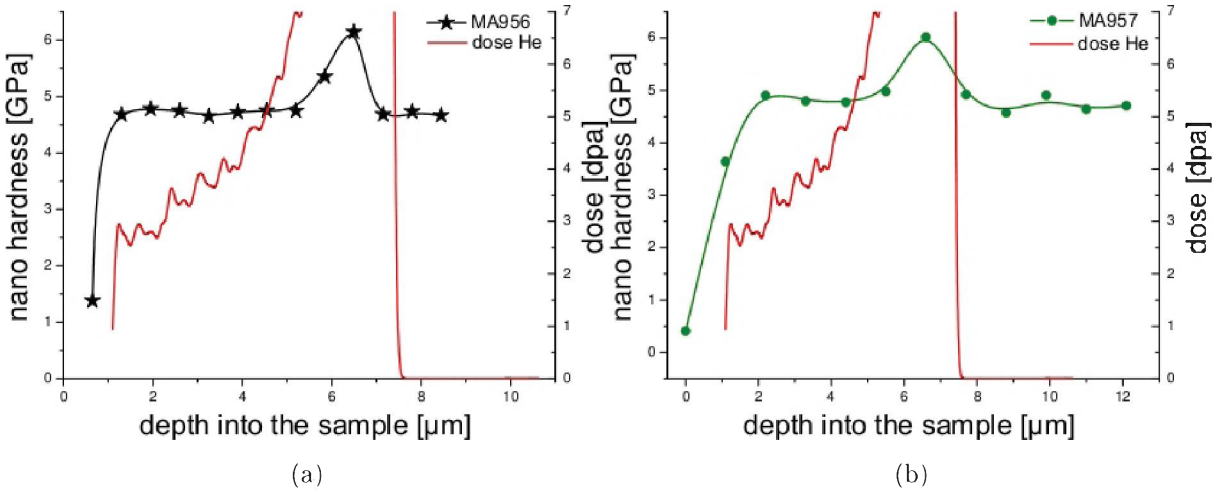

Fig. 90: (a) The hardness vs depth graph of MA956 (a) and MA957 (b) shows no increase in hardness after the He implantation at RT.

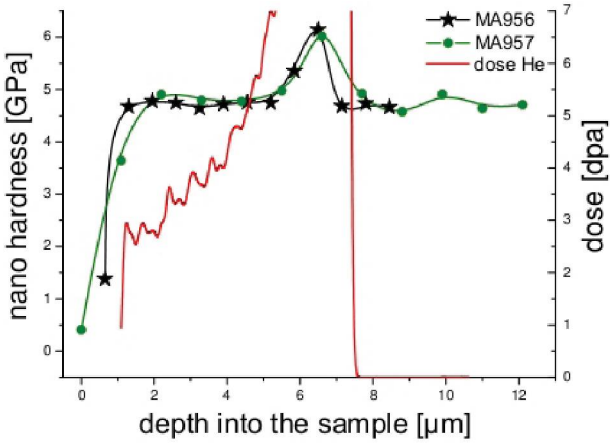

(a)

Fig. 91: Hardness vs depth graph of MA956 and MA957 and dose profile of the He implantation.

4.2.4 Discussion of the Helium implantation at RT of the advanced materials

After the Helium implantation was completed only a characterisation by using nanoindentation and AFM was performed, therefore no results from TEM are available to discuss. The implantation of MA956 and MA957 with Helium ions at RT did not show a significant hardening of the 3 dpa region according to a 3 % hardness increase for the HT-9 tempered martensitic steel and a 7 % increase for the HT-9 ferritic steel. It was found that due to the high He implantation in the ion stopping region the samples showed significant blistering just as it was investigated in the conventional materials. The nano indents which were placed in a non cracked area in that region showed no pile-up surrounding as well as it was found after the AFM measurement on the conventional materials. We assume that the Helium ions remain in the stopping region of the sample which increases the number of defects in the region while the protons are small enough to diffuse out of the material so that only the dpa effect in that region remains. The irradiation with protons will reveal if the cracking and the absence of pile-up surrounding at the indents is due to the Helium or the radiation damage.

4.2.5 Proton irradiation at room temperature

After the room temperature irradiation with protons of the MA956 and MA957 samples was completed, the nanoindentation on those samples was performed. It was not found any blistering we have seen in the samples due to the He implantation in the ion stopping region and there were no significant hardness increasing at the 3 dpa region of the samples. A significant difference between He implantation and proton irradiation was that we only could see a sink in effect at the He implanted samples, however not on the proton irradiated samples. The depths of the indents were determined with an isometric projection and a depth profile through the indents where we could not measure the disappearance of a pile up at the stopping peak of the protons. The post indentation AFM revealed that no difference in pile up could be detected between the stopping region and bulk material.

The hardness data obtained of MA956 (a) and MA957 (b) after the room temperature irradiation are shown in Fig 95 in comparison to the hardness data obtained after He implantation.

After the irradiation at room temperature was completed FIB foil of MA956 and MA957 were prepared and a characterisation by using TEM performed.

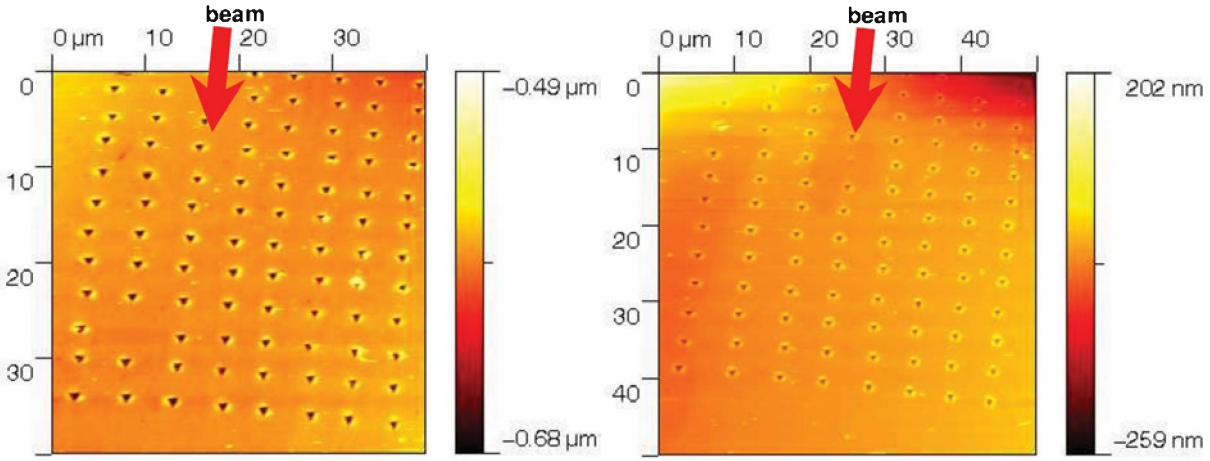

(a) (b)

Fig. 92: (a) The image illustrates the array of indents performed on MA956 after the proton irradiation at RT. (b) Nanohardness performed on MA957 after the proton irradiation at RT.

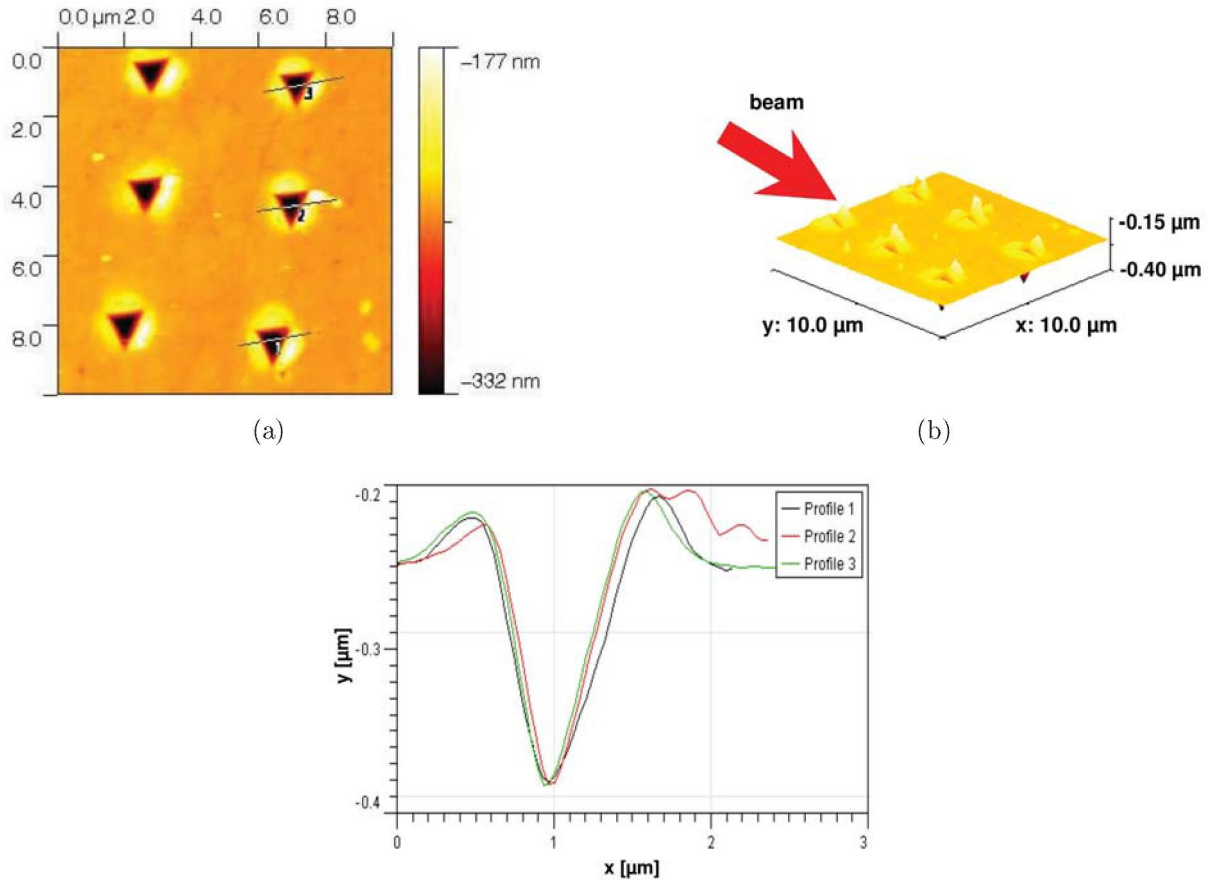

(a) (b)

(c)

Fig. 93: In image (a) an array of three nanoindents performed on MA956 after the proton irradiation at RT is shown. (b) The isometric projection developed from the array in image (a). (c) Depth profil of the indents determined from the AFM image in (a).

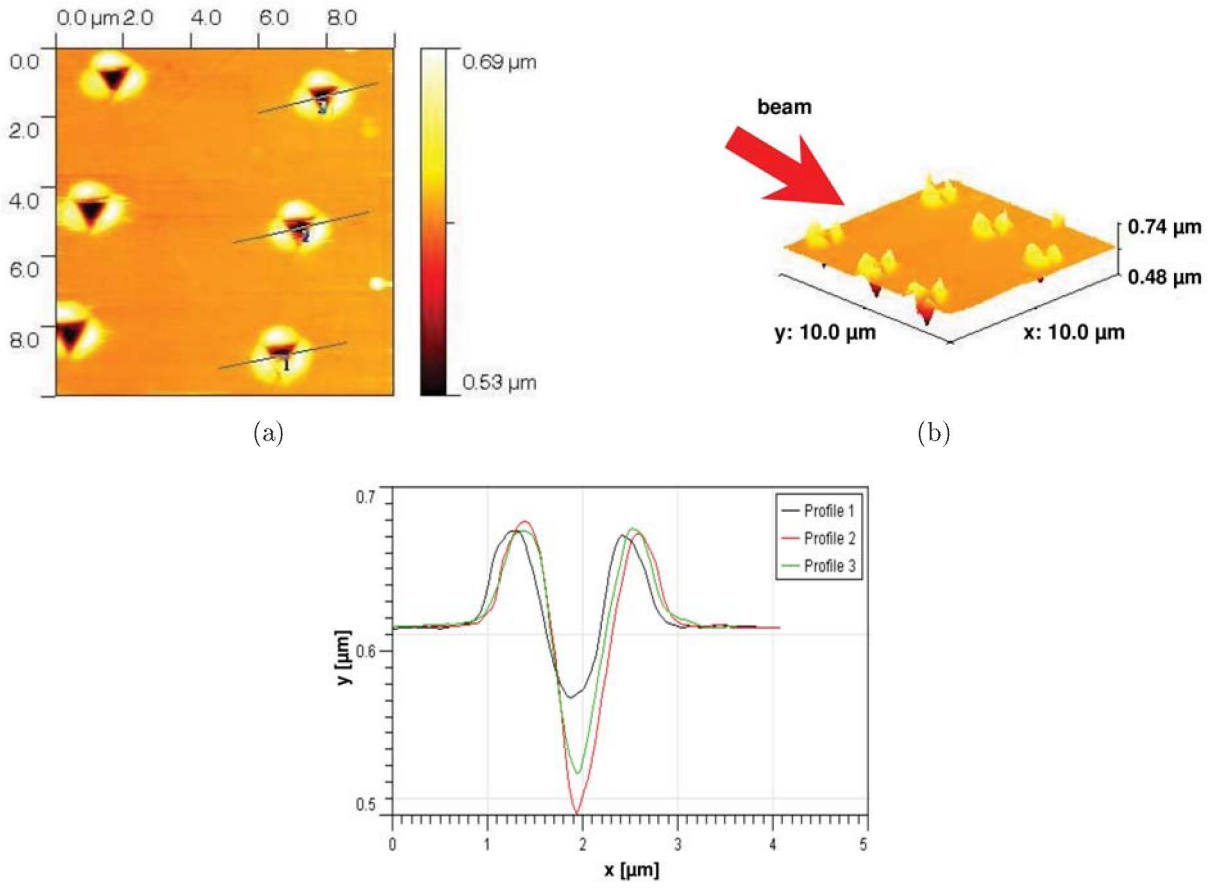

(a) (b)

(c)

Fig. 94: In image (a) an array of three nanoindents performed on MA957 after the proton irradiation at RT is shown. (b) The isometric projection developed from the array in image (a). (c) Depth profil of the indents determined from the AFM image in (a).

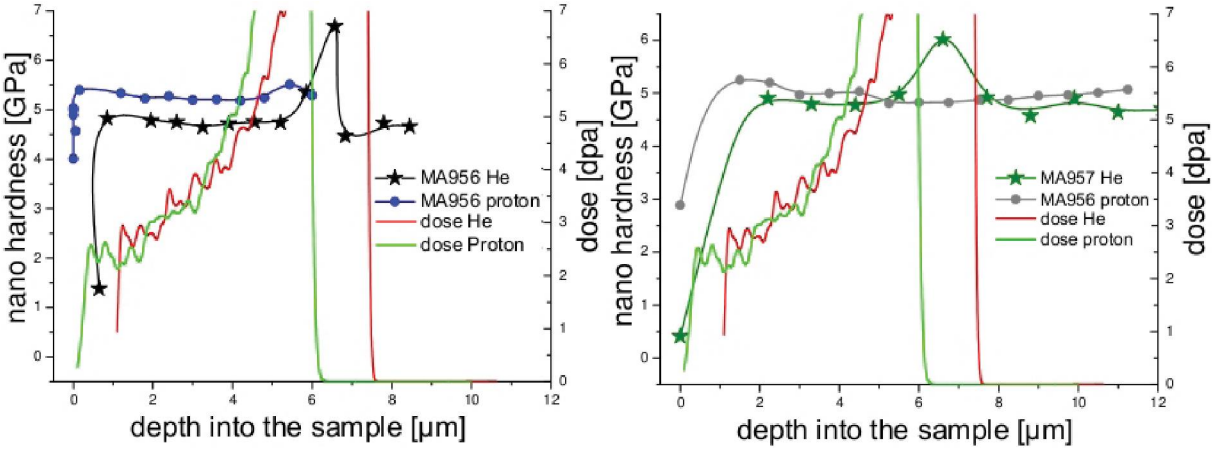

(a) (b)

Fig. 95: (a)Hardness vs depth graph of MA956 after the He implantion and the proton irradiation at RT.(b) Hardness vs depth graph of MA957 after the He implantion and the RT irradiation with protons.

Results obtained by TEM after the RT irradiation of MA956

In the TEM overview image of the FIB foil shown in Fig 96, is beside some blackspot damage which is visible in a depth of about 6 μm where the most irradiation damage is expected also the microstructure of MA956 seen after the irradiation with protons at RT.

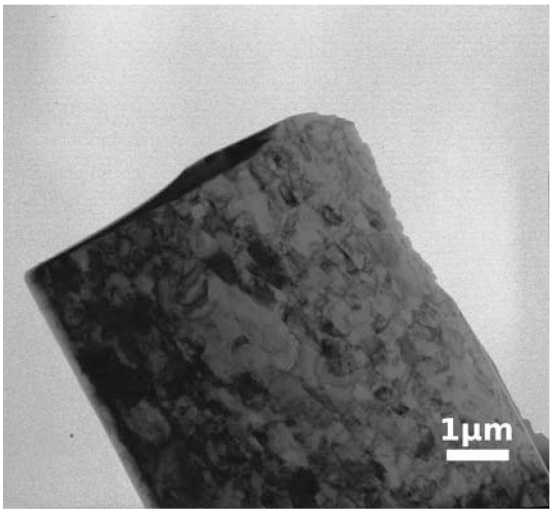

(a)

Fig. 96: The BF image shows an overview of the microstructure of MA956 after the proton irradiation at RT taken at Mag 4400 x.

In Fig 97 the ED pattern in the upper right corner of the BF image in (a) is showing a zone achses of MA956, the zone achses was slightly tilt to get additional reflexes showing in the ED pattern in the right upper corner showing in (b) therefor one of the additional reflexes are lead to the DF image in (b).

The thickness of the MA956 foil was measured twice from the images shown in Fig 98 and Fig 99 and lead to an average thickness value of about 173 nm after the evaluation of the lenght of the dislocations.

The BF image taken at Mag 42 kx in Fig 100 shows the damage caused by irradiation in detail and was used to evaluate the thickness of the MA956 foil after the RT irradiation. Thus the total projected length R_p is 3,86 * 10^{-5} m which results in a dislocation densitiy R_p of approximatily 3,17 * 10^{14} m^{-2}.

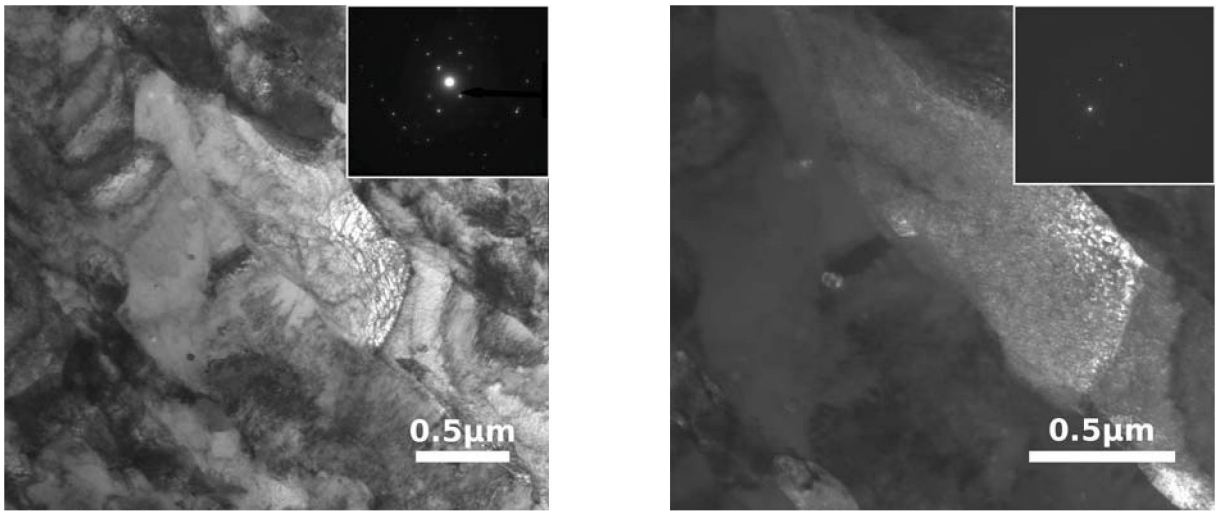

(a) (b)

Fig. 97: (a) showes a BF images of MA956 after the proton irradiation at RT and in (b) the DF image togehter with the ED-pattern where the pointed reflex leads to a bright appearance of a ODS particle together with a grain of the matrix. The images were taken at (a) Mag 13,5 kx and (b) Mag 21 kx.

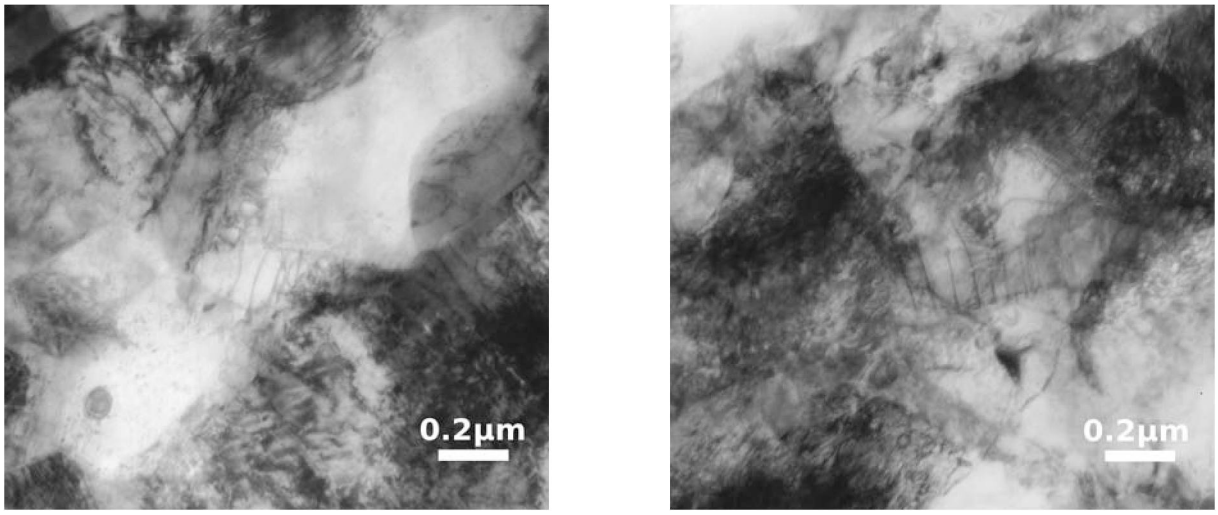

(a) (b)

Fig. 98: Both images were taken at Mag 69 kx of MA956 after the proton irradiation at RT but at different tilting angles to determine the thickness of the foil. In (a) the tilting angel was 0° and in (b) the images was taken at +10°.

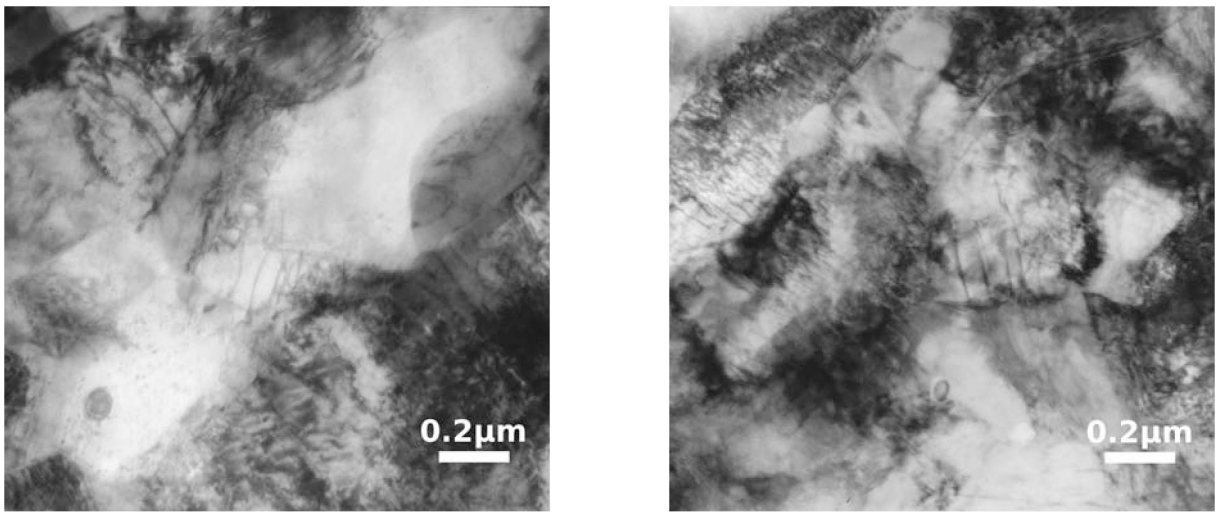

(a) (b)

Fig. 99: Both images were taken at 69 kx of MA956 after the proton irradiation at RT but at different tilting angles to determine the thickness of the foil. In (a) the tilting angel was 0° and in (b) the images was taken at -4°.

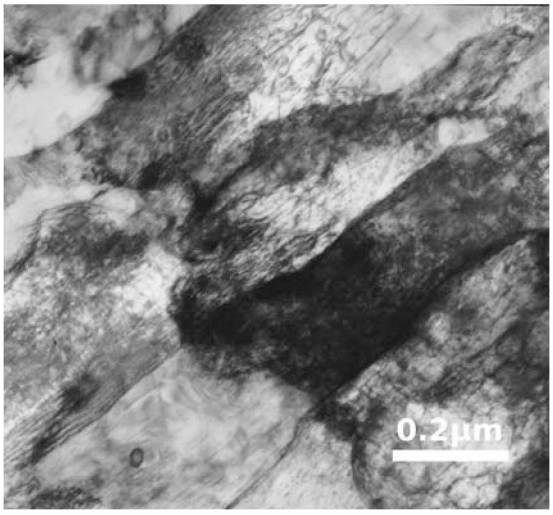

(a)

Fig. 100: The BF image shows beside the microstructure of MA956 after the proton irradiation at RT taken at Mag 42 kx some blackspot damage caused by the irradiation. The image was taken to evaluate the dislocation density of MA956 after the RT irradiation.

Results obtained by TEM after the RT irradiation of MA957

The image taken at Mag 4400 x in Fig 101 shows an overview of the FIB foil of MA957 after the irradiation with protons at room temperature.

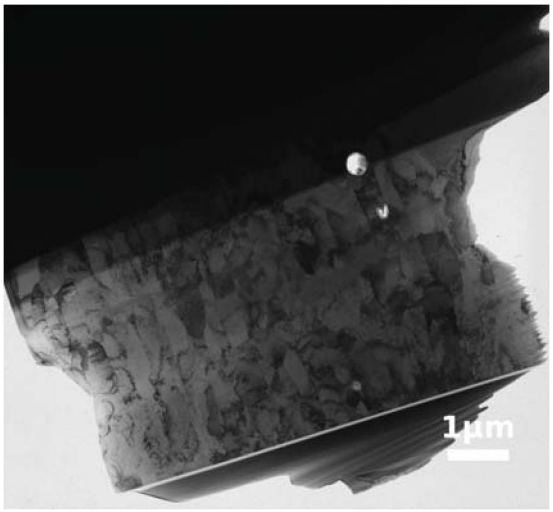

(a)

Fig. 101: The BF image taken at Mag 4400 x gives an overview of the microstructure of MA957 after the proton irradiation at RT.

The BF images in Fig 102 and Fig 103 of MA957 show the 20- 50 nm ODS particles as well as some black spot damage caused by the irradiation with protons at RT.

In the ED-pattern shown Fig 104, Fig 105 and Fig 106 the reflexes pointed on are coming from a gain of the matrix an some ODS particles which are fulfill the condition by Bragg so they appear bright in the DF images (b) which corresponds to the BF image shown in (a).

The thickness of the MA957 foil was measured from the images shown in Fig 107 and lead to a thickness of 208 nm after the lenght of the dislocations was evaluated.

Fig 108 illustrates the BF image taken at Mag 89 kx which was used to calculate the total projected length R_p is 1,83 * 10^{-5} m and furthermore the dislocation densitiy R_p of approximatily 4,06 * 10^{14} m^{-2} of the MA957 foil after the RT irradiation.

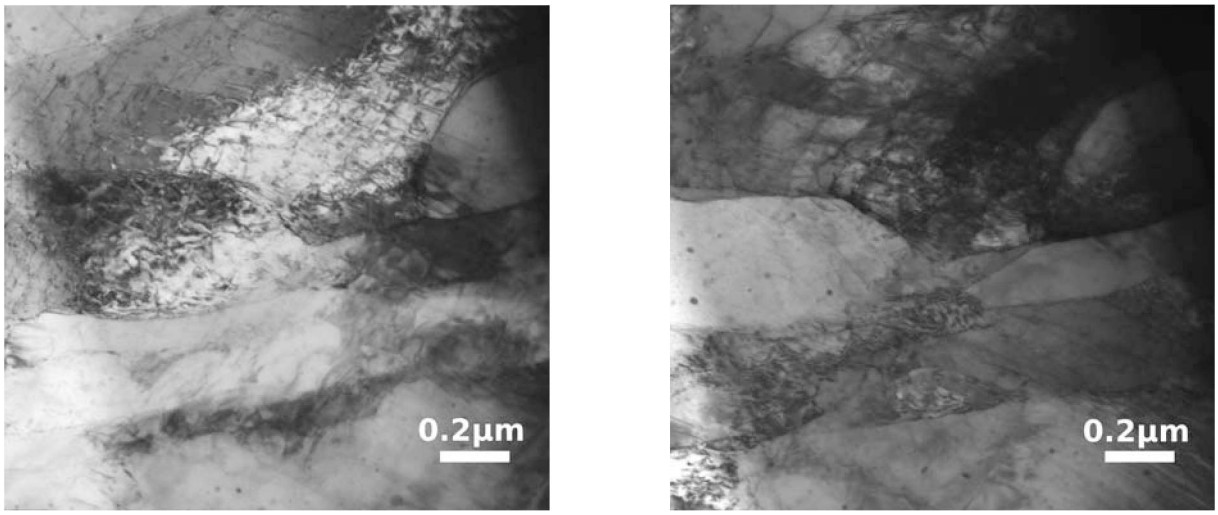

(a) (b)

Fig. 102: The BF images (a) and (b) shows an overview of the microstructure of MA957 after the proton irradiation at RT. The image in (a) was taken at Mag 4400 x and (b) at Mag 52 kx.

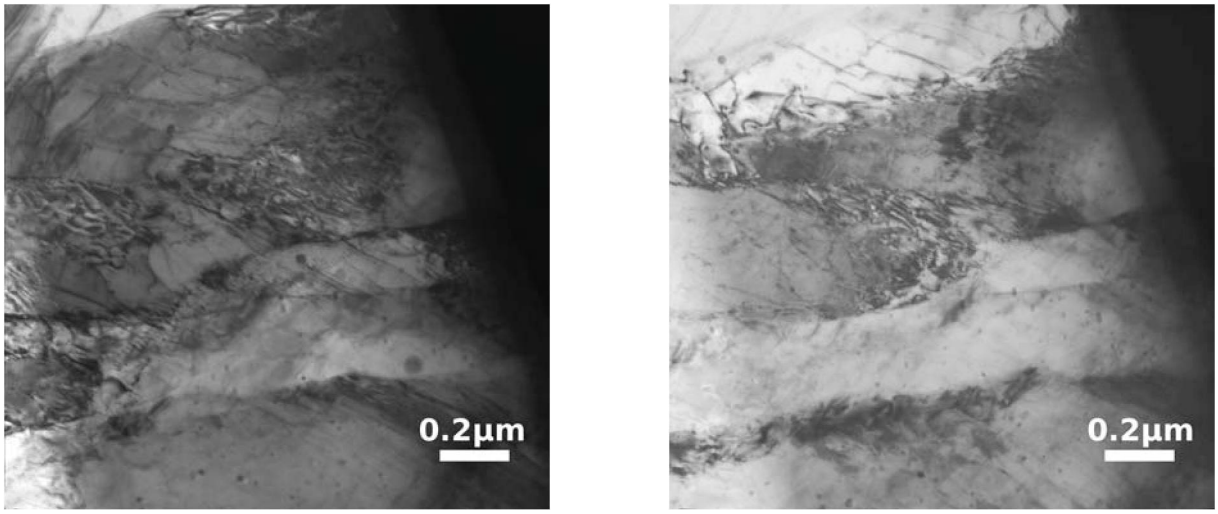

(a) (b)

Fig. 103: The BF images (a) and (b) show an overview of the microstructure of MA957 after the proton irradiation at RT. Both images were taken at Mag 52 kx and do show the nanosized ODS particles randomly distributed in the matrix.

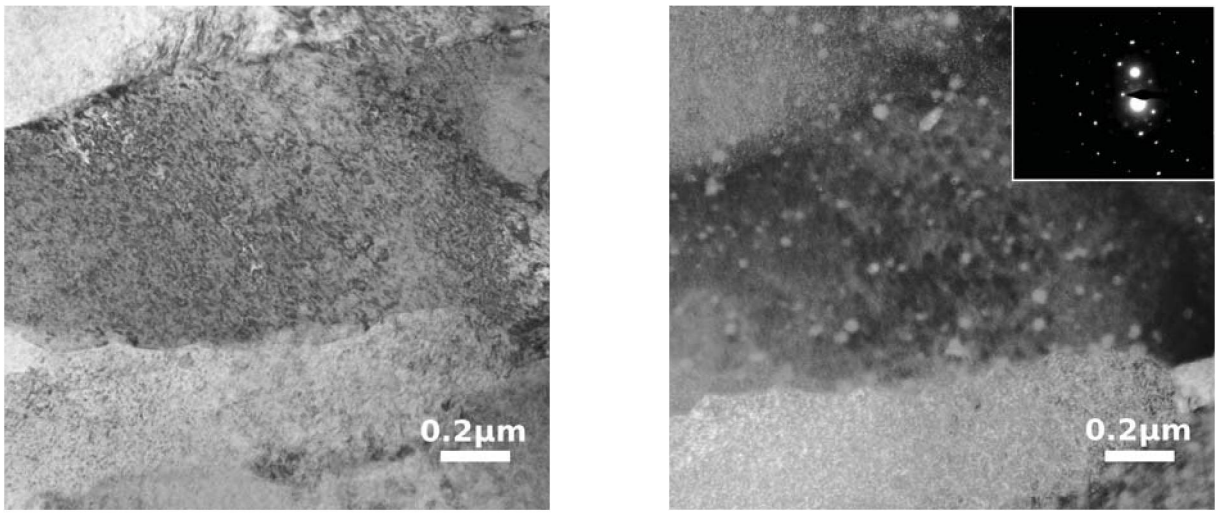

(a) (b)

Fig. 104: (a) showes a BF images of MA957 after the proton irradiation at RT and in (b) the DF image togehter with the ED-pattern where the pointed reflex leads to a bright appearance of a grain in the matrix. Both images were taken at Mag 52 kx.

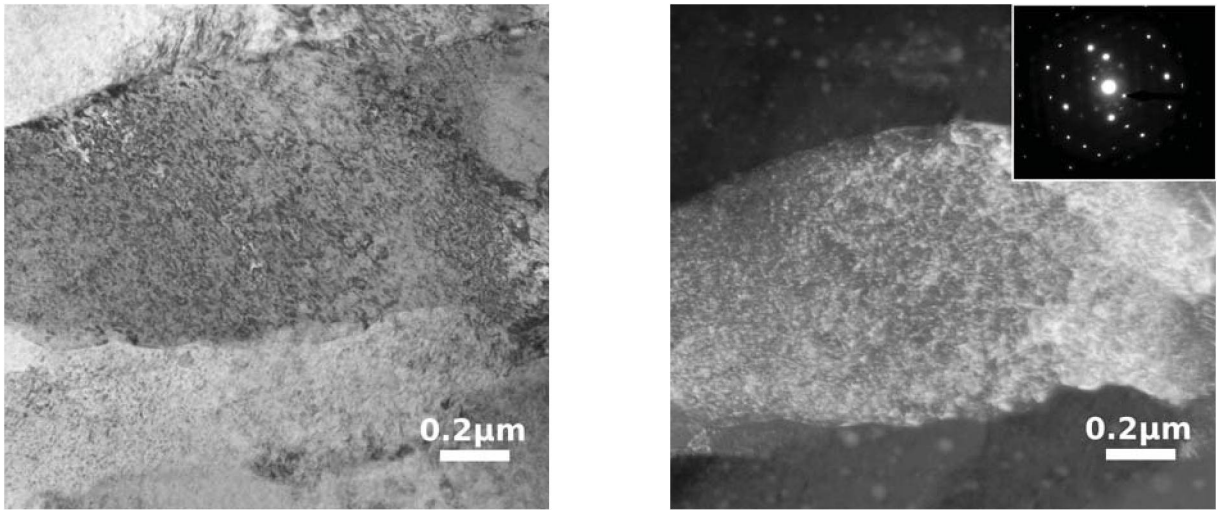

(a) (b)

Fig. 105: (a) showes a BF images of MA957 after the proton irradiation at RT and in (b) the DF image togehter with the ED-pattern where the pointed reflex leads to a bright appearance of another grain of the matrix. Both images were taken at Mag 52 kx.

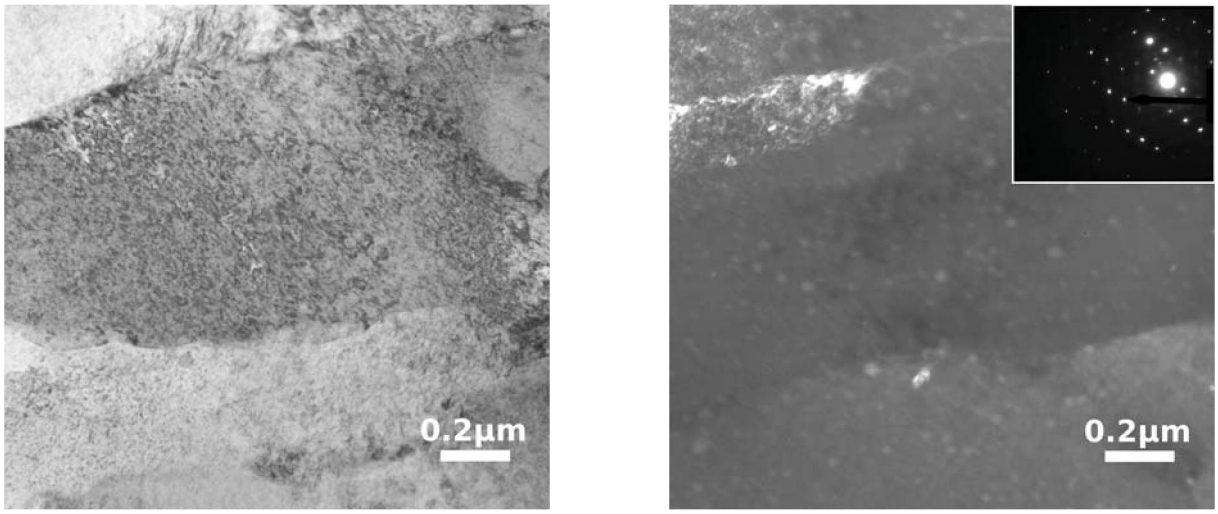

(a) (b)

Fig. 106: (a) showes a BF images of MA957 after the proton irradiation at RT and in (b) the DF image togehter with the ED-pattern where the pointed reflex leads to a bright appearance of some ODS particles. Both images were taken at Mag 52 kx.

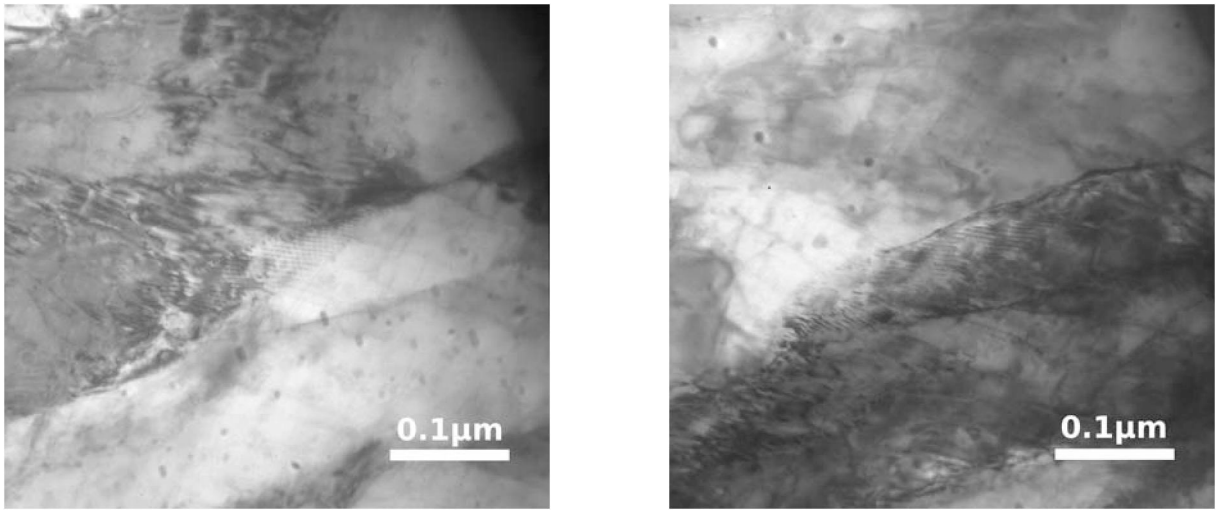

(a) (b)

Fig. 107: Both images of MA957 after the proton irradiation at RT were taken at Mag 89 kx but at different tilting angles to determine the thickness of the foil. In (a) the tilting angel was 0° and in (b) the images was taken at +8°.

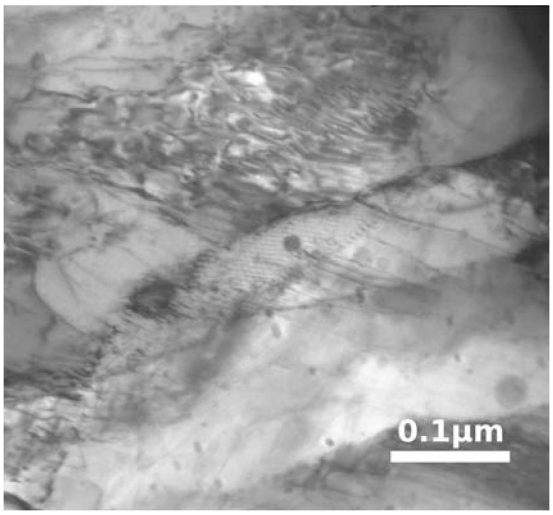

(a)

Fig. 108: The image of MA957 after the proton irradiation at RT was taken at Mag 89 kx and was used to determine the dislocation density of the foil from the dislocation shown in two beam condition.

4.2.6 Discussion of the proton irradiation at RT of the advanced materials

After the room temperature irradiation with protons of the MA956 and MA957 samples was completed, the post indentation AFM revealed that no difference in pile up could be detected between the stopping region and the bulk material. A significant difference between the He implantation and the proton irradiation was that we only could see a sink in effect at the He implanted samples. There was no blistering found in the proton irradiated samples as we have found in the samples where the He ions stop and no pile up around the nano indents in that particular row of indenst was seen due to the He implantation in the ion stopping region. No significant hardness increasing at the 3 dpa region of the samples was found same as we have evaluated at the post indentation after the Helium implantation of MA956 and MA957. After the TEM examination it was found that black spot damage occurred in MA956 as well as in MA957 in a depth of about 6 μm where the stopping region of the protons is expected. The evaluation of the dislocation density of MA956 and MA957 after the irradiation with protons at RT showed an increase in dislocation density compared to the value obtained from the pre irradiated sample. The dislocation density of the pre irradiated MA956 is ρ = 2,09 * 10^{14} m^{-2} and after the irradiation with protons at RT ρ = 3,17 * 10^{14} m^{-2}. The dislocation density of the pre-irradiated MA957 is ρ = 2,51 * 10^{14} m^{-2} and after the irradiation with protons at RT ρ = 4,06 * 10^{14} m^{-2}. For the RT irradiation with protons it was found that there was no increase in hardness measured by nanoindentation but an increase in dislocation density for both advanced materials compared to the data obtained of the pre irradiated samples. As for those dispersoid materials a strong increase in hardness mainly is coming from the fine grain which will be stabilized by the nanosized particles at elevated temperature. It will be assumed that an increase in dislocation density have no distinct effect in hardening even more an effect in an increase in defect density caused by irradiation. Additional thickness measurments are necessary and therefore additional evaluations of the dislocation density of different areas of the foil to verify the gained results.

4.2.7 Proton irradiation at 300 °C

In this study the advanced materials (MA956 and MA957) were irradiated up to 300 °C and showed also in this temperature range their superior radiation tolerance as presented through nanohardness measurments in Fig. 112. With AFM examination performed on both samples no difference in pile up was detected between the stopping region and the bulk material as shown in Fig. 109 to Fig. 111.

The hardness data obtained of MA956 and MA957 after the irradiation at 300 °C

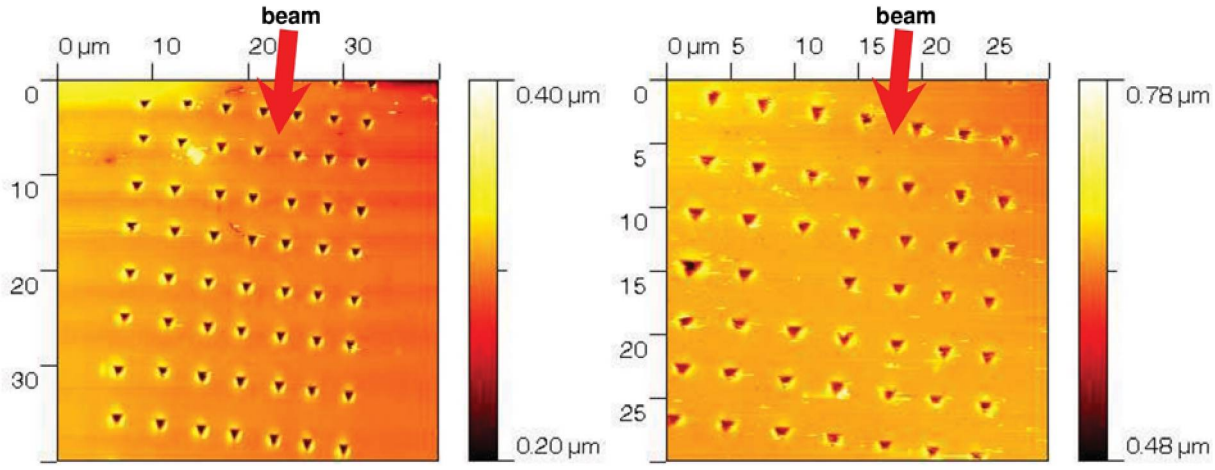

Fig. 109: (a) The image illustrates the array of indents performed on MA956 after proton irradiation at 300 °C. (b) Nanohardness performed on MA957 after proton irradiation at 300 °C.

are illustrated in Fig 112 and do not show any significant hardness increase due to the irradiation with protons as there was shown due to the Helium implantation.

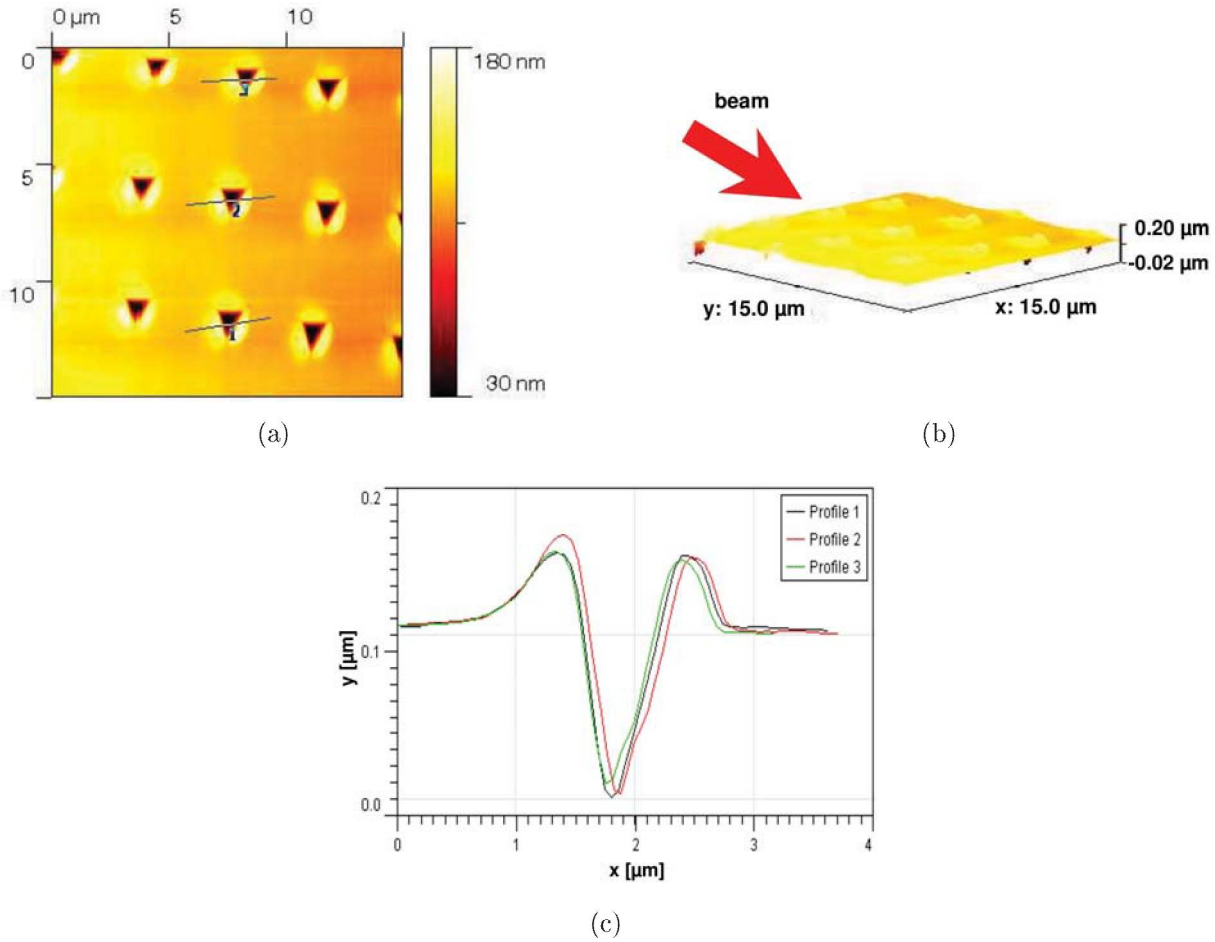

Fig. 110: In image (a) an array of three nanoindents performed on MA956 after proton irradiation at 300 ℃ is shown. (b) The isometric projection developed from the array in image (a). (c) Depth profil of the indents determined from the AFM image in (a).

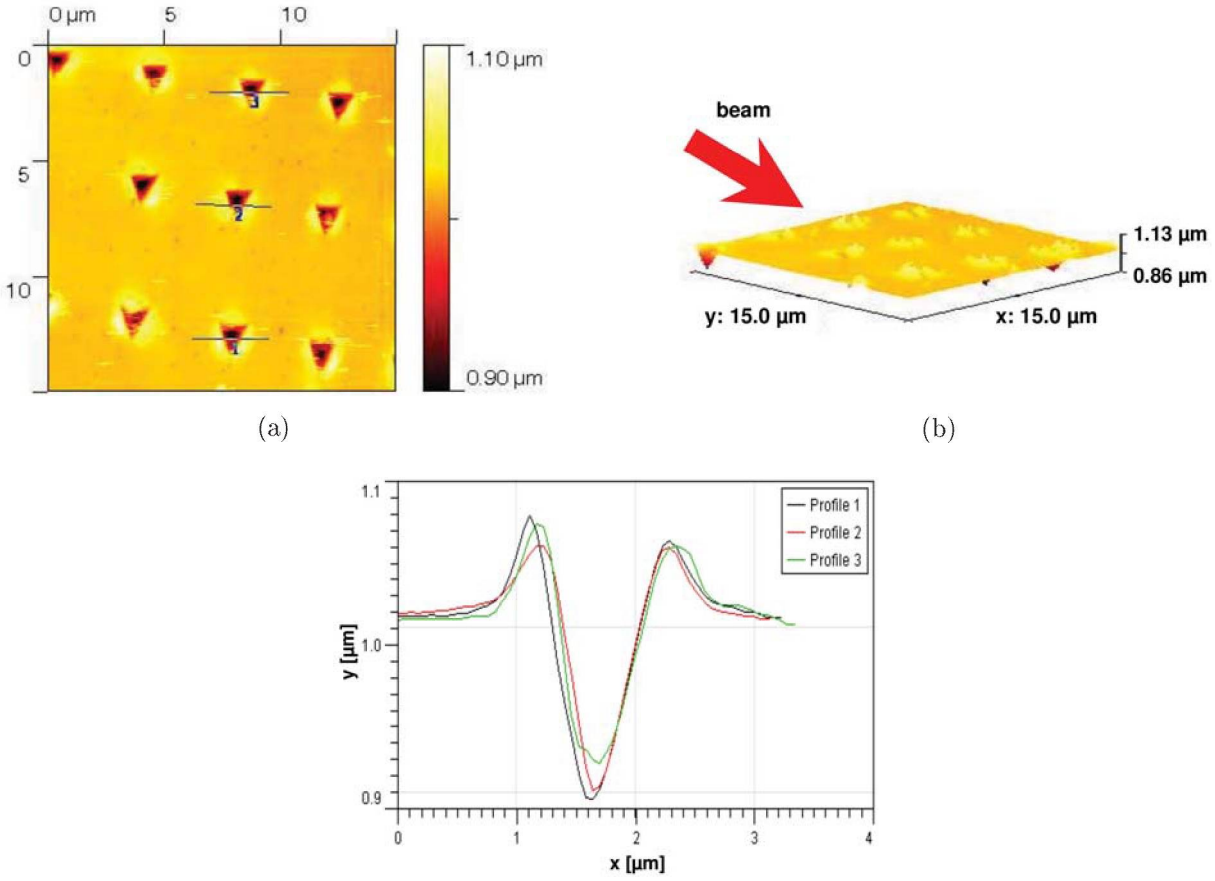

(a) (b)

(c)

Fig. 111: In image (a) an array of three nanoindents performed on MA957 after proton irradiation at 300 ℃ is shown. (b) The isometric projection developed from the array in image (a). (c) Depth profil of the indents determined from the AFM image in (a).

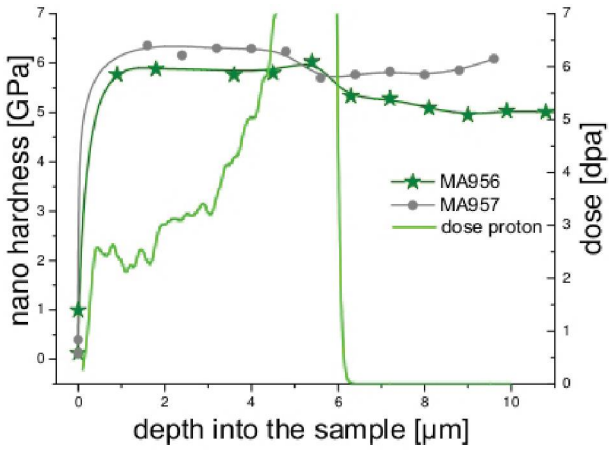

(a)

Fig. 112: (a)Hardness vs depth graph of MA956 and in (b) of MA957 after the irradiation at 300 ℃ with protons.

Results obtained by TEM after the irradiation at 300 °C of MA957.
The images in Fig. 113 and Fig. 114 are showing an overview of the FIB foil and some black spot damage in a depth of about 6 μm, where the stopping region of the protons is expected, caused by the irradiation with protons.

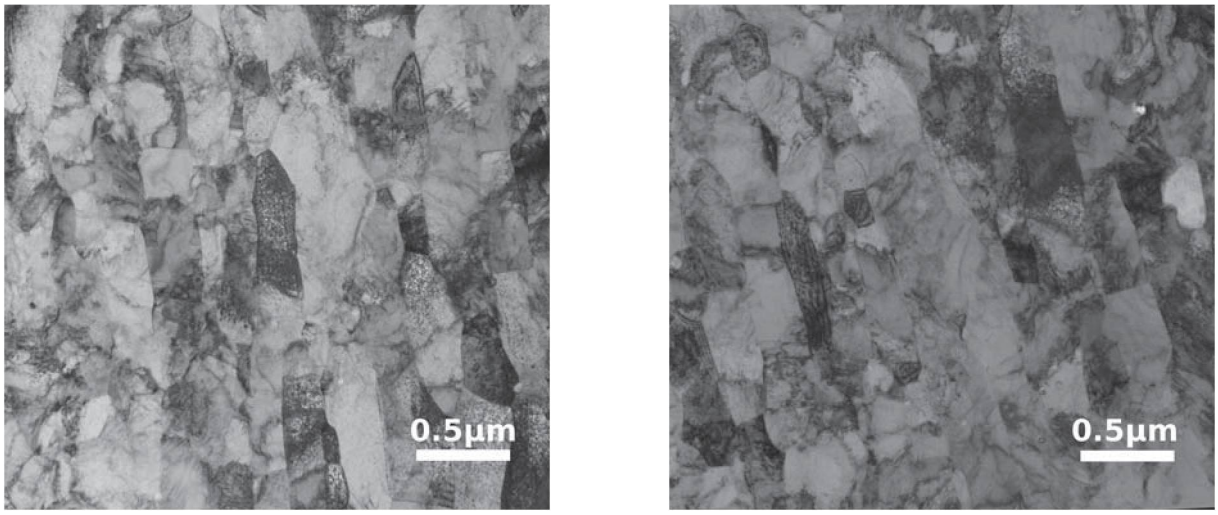

(a) (b)

Fig. 113: The BF images (a) and (b) show an overview of the microstructure of MA957 after proton irradiation at 300 °C, they are taken at Mag 13,5 kx.

To determine the thickness of the MA957 foil after the 300 °C irradiation the lenght of the same dislocations appering at different tilting angels was measured. This leads to the thickness of around 158 nm after two different measurments, first the pair at 0° and +17° as shown in Fig 115 and second the pair +2° and +20° in Fig 116.

From the BF image shown in Fig 117 the total projected length R_p of 2,42 * 10^{-5} m was calculated and therefore the dislocation density of approximatily 2,18 * 10^{14} m^{-2} for the MA957 sample after the irradiation with Protons at 300°C.

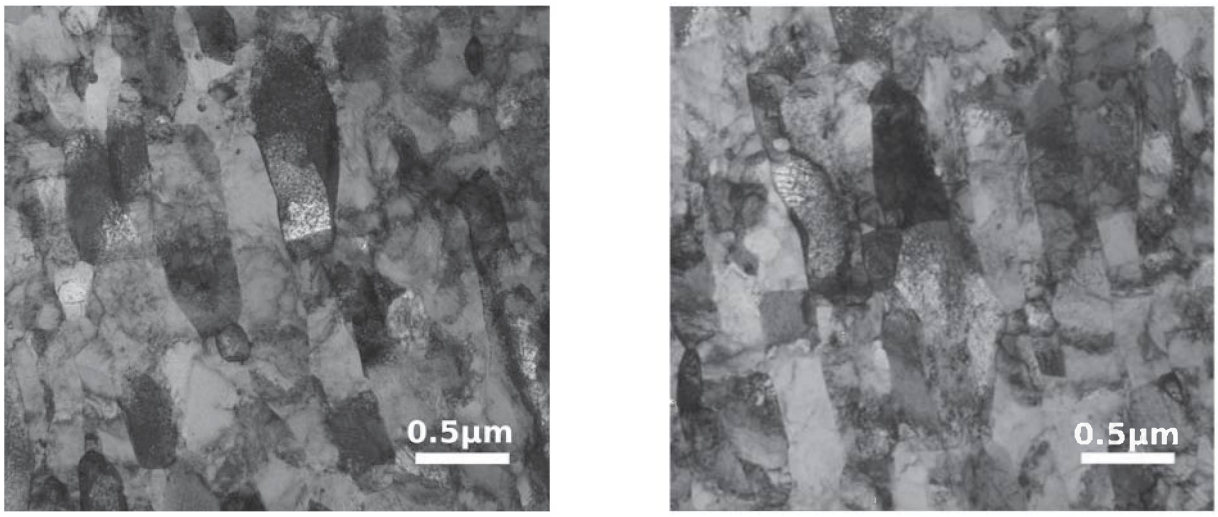

(a) (b)

Fig. 114: The BF images (a) and (b) taken at Mag 13,5 kx show an overview of the microstructure of MA957 after proton irradiation at 300 °C.

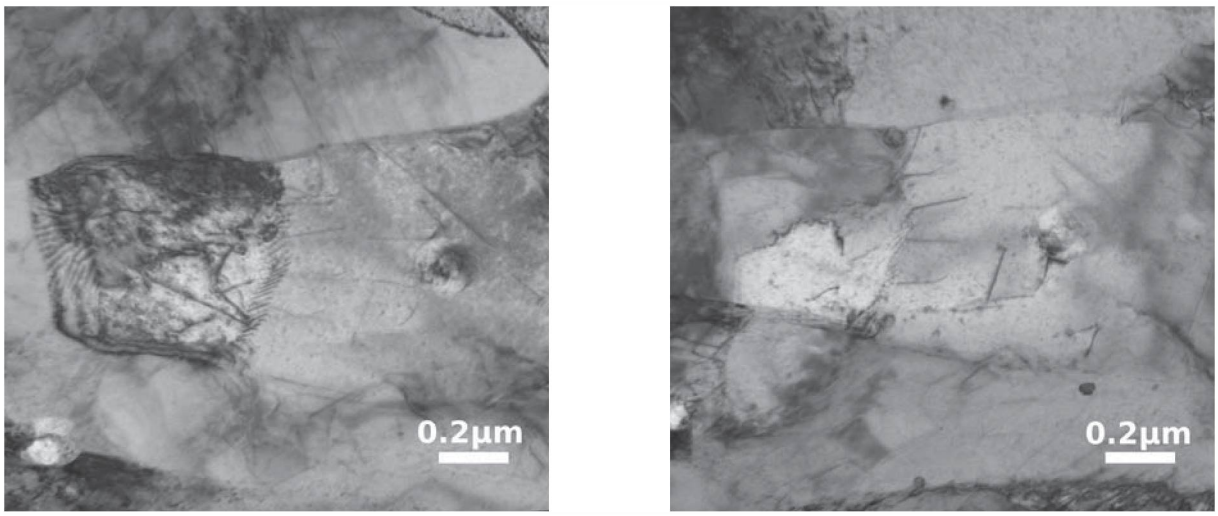

(a) (b)

Fig. 115: Both images were taken at Mag 52 kx of the MA957 sample after the proton irradiation at 300 °C but at different tilting angles to determine the thickness of the foil. In (a) the tilting angel was 0° and in (b) the images was taken at +17°.

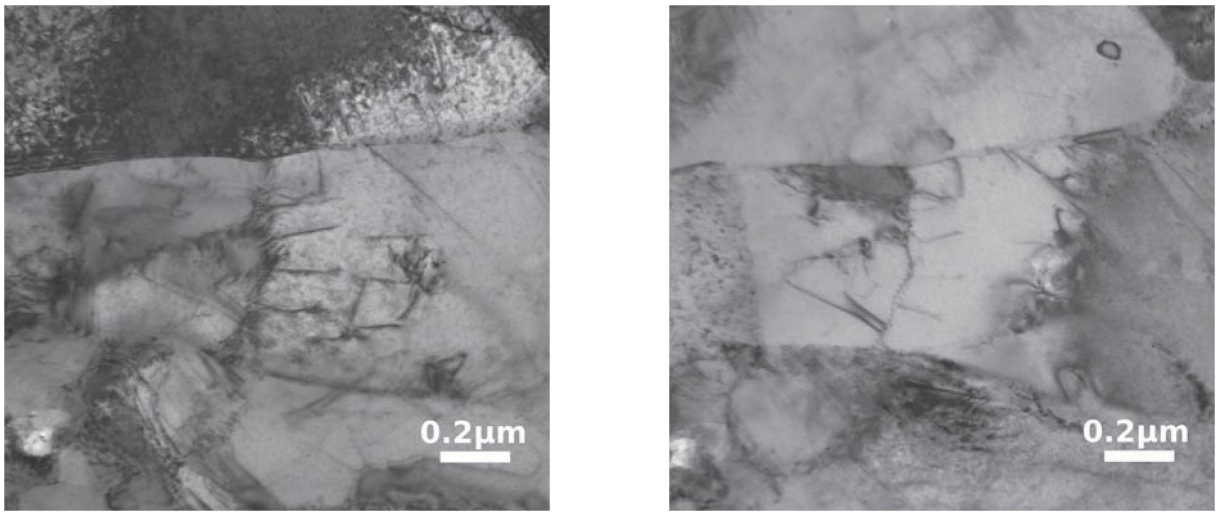

(a) (b)

Fig. 116: Both images of MA957 after proton irradiation at 300 °C were taken at Mag 52 kx but at different tilting angles to determine the thickness of the foil. In (a) the tilting angel was +2° and in (b) the images was taken at +20°.

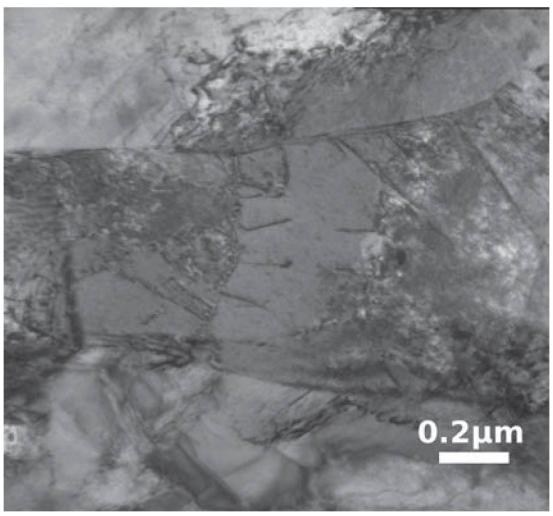

(a)

Fig. 117: Shows the BF image of MA957 after the irradiation at 300 °C taken at Mag 52 kx from which the dislocation density was evaluated.

4.2.8 Discussion of the proton irradiation at 300 °C for the advanced materials

The advanced materials (MA956 and MA957) were irradiated up to 300 °C and showed also in this temperature range their superior radiation tolerance. On both dispersoid strengthened mateials no hardness increase was evaluated by nanohardness after the irradiation at 300 °C just as at the irradiation with protons at RT. With AFM examination performed on both samples no difference in pile up behavior was detected or any occurrence of cracking at the stopping region as it was found after the Helium implantation. The characterisation by using TEM was performed only on the MA957 sample after the proton irradiation at 300 °C but showed in a depth of about 6 μm, where the stopping region of the protons is expected some black spot damage as well as it was found after the proton irradiation at RT. The evaluation of the dislocation density of MA957 of the pre irradiated sample was ρ = 2,51 * 10^{14} m^{-2}, after the irradiation with protons at RT a dislocation density ρ of 4,06 * 10^{14} m^{-2} was measured and after the proton irradiation at 300 °C ρ = 2,18 * 10^{14} m^{-2}. The decrease in dislocation density from the value obtained after the RT irradiation to the value gained after the 300 °C measurment can be explained as there are recovery effects taking place because of the elevated temperature and therefore the damage caused by irradiation is not as severe as it is expected at room temperature and proven through the tremendous increase in dislocation density after the RT experiment. Additional thickness measurments and therefore additional evaluations of the dislocation density of different areas of the foil would have been necessary to verify the gained results.

4.2.9 Proton irradiation at 550 °C

In this study the advanced materials (MA956 and MA957) were irradiated up to 550 °C but there were no post nanonindentation, AFM measurments or TEM performed. Thus no results are to evaluate and no discussion is to accomplish.

5 Conclusion

TEM characterisation of the pre irradiated conventional materials showed the microstructural change from HT-9 ferritic steel where the carbides are arranged at the grain boundaries to HT-9 tempered martensitic steel where due to the tempering process these carbides were enlongated and arranged along the martensite lath. The transformation from a ferritic in a martensitic structure leads to an increase in microhardness from HV0.2 = 198 in HT-9 ferritic steel to HV0.2 = 255 in HT-9 tempered martensitic steel as the fine microstructure is acting as barrier for dislocations. Therefor an increase in hardness correlates with an increase in dislocation density ρ from 2,37 * 10^{14} m^{-2} in HT-9 ferritic steel to 2,87 * 10^{14} m^{-2} in HT-9 tempered martensitic steel.

The characterisation by using TEM of the pre irradiated advanced materials showed their microstructure in which the nanosized ODS particles were distributed in the matrix. The effect of those 20-50 nm ODS particles results in a significant higher microhardness of HV0.2 = 267 for MA956 and HV0.2 = 346 for MA957 compared to the microhardness of the conventional steels as those dispersoide particles are acting as additional barrier for dislocations beside the fine grain of the matrix. The dislocation density of the advanced materials in the pre irradaited condition is ρ = 2,09 * 10^{14} m^{-2} for MA956 and 2,51 * 10^{14} m^{-2} for MA957.

The TEM investigation of the proton irradiated samples showed a damage similar to black spot damage in a depth of about 6 μm where the stopping region of the protons is expected. The evaluation of the dislocation density of HT-9 ferritic steel after the irradiation with protons at RT showed an increase in density compared to the dislocation densitiy evaluated from the pre irradiated sample. The at 300 °C irradiated sample of HT-9 ferritic steel showed a strong decrease in dislocation density compared to the pre irradiated condition. The at 550 °C irradated sample of HT-9 tempered martensitic steel has a higher dislocation density than the pre irradiated sample and is about the same compared to the dislocation density evaluated of the at RT irradiated sample. The irradiation with protons showed that at higher irradiation temperatures a strong hardness decrease for the conventional materials occured caused by recovery effects at elevated temperature. For the HT-9 tempered martensitic steel the hardness decrease was stronger as for the ferritic steel due to the fact that the martensitic microstructure has a high density of interfaces which act as recombination sites for radiation induced defects. Therefore it should be a more radiation tolerant material as the HT-9 ferritic steel.

For the RT irradiation with protons it was found that there was no increase in hardness measured by nanoindentation but an increase in dislocation density for both advanced materials compared to the data obtained of the pre irradiated samples. The decrease in dislocation density measured of MA957 after the 300 °C irradiation compared to the value obtained of the pre irradiated and the RT irradiated condition can be explained by a very high density of interfaces caused by those dispersoid particles which act as recombination sites for radiation induced defects and recovery effects which starting to take place because of the elevated temperature. Therefore the damage caused by irradiation at 300 °C is not as severe as it is expected at room temperature where a strong increase in dislocation density was evaluated. In this study the advanced materials (MA956 and MA957) were irradiated up to 550 °C and results obtained from the irradiation up to 300 °C were they showed also in this temperature range their superior radiation tolerance as presented through nanohardness measurments and the evaluation of dislocation density.

As shown previously nanoindentation in combination with ion beam irradiation can be used to measure radiation induced hardness increase. It was found that the HT-9 tempered martensitic steel harden less with dose and temperature than the HT-9 ferritic steel. A clear relation of hardness and irradiation temperature was shown for the conventional materials. It was found that the ODS alloys MA956 and MA957 did not show any hardness increase due to irradiation under any of those conditions. After the He implantation of all investigated materials was completed and nanoindentation and AFM was performed it was found that the region where the He ions stop significant cracking occurred and no pile up around the nano indents in that particular row of indenst was found while the region around the proton stopping region at all irradiation condition showed neither. It will be assumed that the Helium ions remain in the stopping region of the sample which increases the number of defects in the region while the protons are small enough to diffuse out of the material so that only the dpa effect in that region remains.

It appears that between an irradiation temperature range of 300 °C to 550 °C a strong hardness decrease occurs. The fact that the room temperature experiments were performed at 1.5 dpa while the higher temperature experiments were performed at 1 dpa might also play a role in the strong decrease in radiation induced hardenss at the high temperature experiments. In the literature it was found that in reactor experiments with a lower dose rate the transition temperature in radiation induced hardness increase is between 410-430°C. It is known that irradiations with low dose rate can be compared to irradiations with high dose rate by considering a shift to higher temperatures for the low

dose rate experiment [15]. To compare low dose rate data to high dose rate the faster experiment has to be performed at a higher temperature than the slower experiment. It has been shown in the literature that the hardness difference between 1 and 1.5 dpa is small because above 0.5 dpa the changes in mechanical properties is rather gradually [15]. However, to confirm that the main influence from this effect is from the higher temperature and not from lower dose either a high dose-high temperature experiment or a low dose-low temperature experiments need to be performed. Additional evaluations of the dislocation density of different areas of the foil would be needed to confirm the gained results for all irradiation conditions.

The advanced materials did not show an increase in nanohardness compared to the conventional materials under any of those conditions. Therefore, a need to develop techniques to produce these ODS alloys with conventional steel processing technologies as the previous results indicate superior radiation resistance at elevated temperature, exists.

6 summary

Materials testing in a nuclear reactor or spallation source are time consuming and costly activities whereas ion beam accelerator experiments have the advantage of allowing fast and inexpensive materials irradiations without activating the sample by inducing a very high dose rate in a short time compared to neutron experiments. However they do not allow large beam penetration depth which limits the materials testing after irradiation as there are small scale materials testing techniques would be needed. Thus nanoindentation in combination with ion beam irradiation can be used to measure radiation induced hardness increase.

The aim of this work was to compare and evaluate irradiation damage in conventional and advanced materials for nuclear application. For this purpose the response of ODS alloys and conventional materials were evaluated using ion beam irradiation at various temperature. Considering all the different irradiation temperatures (room temperature, 300 °C, 550 °C), doses at the stopping peak and particles (He and protons) it was found that there is clearly a hardness change due to ion irradiation for the conventional materials but there was not found any change in hardness for the advanced materials at any of those conditions.
The conventional materials showed that there is a clear relation of hardness and irradiation temperature. HT-9 tempered martensitic steel harden less with dose and temperature than the HT-9 ferritic steel as there is a higher density of interfaces in HT-9 tempered martensitic steel.

AFM measurments were performed after the nanoindentation and showed that the region where the He ions stop significant cracking and no pile up around the indents occurred in that particular row but it was not found at any of the proton irradiated samples. Which leads to the conclusion that the Helium ions remain in the stopping region of the sample which increases the number of defects in the region while the protons are small enough to diffuse out of the material so that only the dpa effect in that region remains.

The TEM characterisation of the pre irradiated conventional and advanced materials showed their specific microstructure and the dislocation density of all four materials was about the same value in this state. For the proton irradiation conditions it was found that damage similar to black spot occurred in all investigated materials in a depth of about 6 μm where the stopping region of the protons is expected. A tremendous increase in dis-

location density was eveluated for the advanced materials compared to the data obtained of the pre irradiated samples but no increase in hardness was measured by nanoindentation. It will be assumend that those dispersoid particles do pin the dislocations and stop their mobility therefore it has no distinct effect in hardening but even more an effect in an increase in defect density caused by the irradiation. At the 300 °C irradiation of the advanced materials the damage caused by irradiation was not as severe as it was at the room temperature irradiation as there are recovery effects taken place at elevated temperature.

For the conventional materials as well as for the advanced materials additional experiments has to be performed in order to draw final conclusions and to compare low dose rate data to high dose rate.

Virtually there are no large scale processing techniques available to produce those ODS alloys therefore a need exists to develop all kind of machining and welding abilities as the previous results indicate superior radiation resistance at elevated temperature.

Bibliography

[1] Yuan Xu. Summary report of the 2nd princeton-china forum on energy, environment & economic policies. In *Summary-Report-of-the-2nd-Princeton-China-EEE-Forum*, 2009.

[2] J. Spider, L. Langlois, and B. Hamilton. "greenhouse gas emissions of electricity generation chains-assessing the difference". *IAEA Bulletin*, 42:2, 2000.

[3] IEA. Nuclear power. *IEA Energy Technology Essentials*, 4, 2007.

[4] GNEP. `www.scidacreview.org/0803/images/nuclear02.jpg`. *Published by IOP Publishing in association with Oak Ridge National Laboratory, for the US Department of Energy, Office of Science. Copyright 2008 by IOP.*, 2008.

[5] James H. Salinger and Audeen W. Fentimen. *Radioactive Waste Management*. Taylor and Francis New York, 2002.

[6] Peter Dyck and Martin J. Crijns. Rising needs - management of spent fuel at nuclear power plants. *IAEA Bulletin*, 2008.

[7] Paul A. Tipler. *Physik 3.korrigierter Nachdruck*. Spektrum Akademischer Verlag Heidelberg/Berlin, 2000.

[8] Detlef Filges and Frank Goldenbaum. *Handbook of Spallation Research - Theory, Experiments and Applications, 1.Auflage*. WILEY-VCH, 2009.

[9] Paul Scherrer Institut PSI. `http://psi.web.psi.ch/forschung/benutzerlabor_sinq.shtml`. 2009.

[10] R. Schöneberg and A. Schumacher, M.and Flammersfeld. Zerfall des Kobalt 56. *Zeitschrift für Physik A Hadrons and Nuclei*, 192(3):305–312, 1966.

[11] R.L. Klueh. Elevated temperature ferritic and martensitic steels and their application to future nuclear reactors. *International Materials Reviews*, 50(3), 2005.

[12] Guenter Gottstein. *Physikalische Grundlagen der Materialkunde*. Springer Verlag Berlin Heidelberg, 2001.

[13] Albert G. Guy. *Metallkunde für Ingenieure*. Akademische Verlagsgesellschaft Frankfurt am Main, 1970.

[14] Herbert Schumann. *Metallographie*. Deutscher Verlag für Grundstoffindustrie Stuttgart, 1991.

[15] Gary S. Was. *Fundamentals of Radiation Materials Science*. Springer Verlag Berlin Heidelberg, 2007.

[16] L.K. Mansur. Theory and experimental background on dimensional changes in irradiated alloys. *Journal of Nuclear Materials*, 216(C):97–123, 1994.

[17] J.F. Ziegler, J.P. Biersack, and U. Littmark. *The Stopping and Range of Ions in Solids*. Pergamon, New York, 1985.

[18] D.S. Gelles. Microstructural examination of commercial ferritic alloys at 200 dpa. *Journal of Nuclear Materials*, 233-237:293–298, 1996.

[19] R.L. Klueh and A.T. Nelson. Ferritic/martensitic steels for next-generation reactors. *Journal of Nuclear Materials*, 371:37–52, 2007.

[20] K. Borodianskiy, A. Basov, A. Gedanken, and M. Zinigrad. Mechanical alloying of cu-al_2o_3 nanoparticles. *MMT-2008*, 2:141–144, 2008.

[21] M. Klimiankou, R. Lindau, A. Moeslang, and J. Schroeder. Tem study of pm 2000 steel. *Powder Metallurgy*, 48(3), 2005.

[22] E Arzt and Wilkinson. Threshold stresses for dislocation climb over hard particles: The effect of an attractive interaction. *Acta Metallurgica*, 34(10):1893–1898, 1986.

[23] Ralf Bürgel. *Handbuch Hochtemperatur Werkstofftechnik*. Friedrich Vieweg und Sohn GmbH,Verlag, Braunschweig, 1998.

[24] Ion Beam Materials Laboratory. `http://www.lanl.gov/organization/profiles/mst_profile.shtml`. *Materials Science and Technology Division Facility Focus*, 2006.

[25] P. Hosemann, C. Vieh, R.R. Greco, S. Kabra, Cappiello M.J. Valdez, J.A., and S.A. Maloy. Nanoindentation on ion irradiated steels. *Journal of Nuclear Materials*, 389(1):25–29, 2009.

[26] W.C. Oliver and G.M. Pharr. Measurement of hardness and elastic modulus by instrumented indentation: Advances in understanding and refinements to methodology. *Journal of Materials Research*, 19(1), 2004.

|27| W.C. Oliver and G.M. Pharr. Improved technique for determining hardness and elastic modulus using load and displacement sensing indentation experiments. *Journal of Materials Research*, 7(7):1564–1580, 1992.

|28| William D. Nix and Huajian Gao. Indentation size effects in crystalline materials : A law for strain gradient plasticity. *Journal of the Mechanics and Physics of Solids*, 46(3):41 I–425, 1998.

|29| G. Binning. Atomic force microscope and method for imaging surfaces with atomic resolution. (US Patent No.4,724,318), 1986.

|30| G. Binning, C. F. Quate, and C. Gerber. Atomic force microscopy. *Physical Review Letters*, 56:930–933, 1986.

|31| F. J. Giessibl. Advances in atomic force microscopy. *Reviews of Modern Physics*, 75:949–983, 2003.

|32| Richard C. Brundle, Charles A. Evans Jr., and Shaun Wilson. *Encyclopedia of materials characterization.* Butxetworch-Heinemann, a division of Reed Publishing CUSA) Inc, 1992.

|33| Yasufumi Yabuuchi, Sayoko Tametou, Tetsuyuki Okano, Sachilko Inazato, Shoji Sadayama, Yoh Yamamoto, Koji Iwasaki, and Yasuhiko Sugiyama. A sudy of the damage on fib-prepared tem samples of alxga1-xas. *Journal of Electron Microscopy*, 53(5):471–477, 2004.

|34| S. Lipp, L. Frey, C. Lehrer, B. Frank, E. Demm, and H. Ryssel. Investigation on topology of structures milled and etched by focused ion beam. *Journal of Vacuum Science and Technology*, B14:3996–3990, 1996.

|35| N.I. Kato, N. Miura, and N. Tsutsui. A plasma-polymerized protective film for transmission electron microscopy specimen preparation by focused ion beam etching. *Journal of Vacuum Science and Technology*, A16:1127–1130, 1998.

|36| N.I. Kato, Y. Kohno, and H. Saka. Side-wall damage in a transmission electron microscopy specimen of crystalline Si prepared by focused ion beam etching. *Journal of Vacuum Science and Technology*, A17:1201–1204, 1999.

|37| Manfred von Heimendahl. *Einfuehrung in die Elektronenmikroskopie.* Friedrich Vieweg und Sohn GmbH,Verlag, Braunschweig, 1970.

|38| Marc De Graef. *Introduction to Conventional Transmission Electron Microscopy.* Cambrige University Press, 2003.

[39] Frank Krumeich. *Properties of Electrons, their Interactions with Matter and Applications in Electron Microscopy.* Laboratory of Inorganic Chemistry, ETH Zurich, HCI-H111, CH-8093 Zurich.

[40] P. Staron. *Vorlesungsscript: Einführung in die Nutzung von Streumethoden in der Werkstoffforschung.* Helmholtz Gemeinschaft.

[41] David B. Williams and Barry C. Carter. *Transmission Electron Microscopy: A Textbook for Materials Science I-IV.* Plenum Press New York and London, 1996.

[42] J.E. Bailey and P.B. Hirsch. The dislocation distribution, flow stress, and stored energy in cold-worked polycrystalline silver. *Philosophical Magazine*, 5(53):485 – 497, 1960.

[43] R. K. Ham. The determination of dislocation densities in thin films. *C.S.I.R.O., Division of Tribophysics, University of Melbourne*, pages 1183–1184, 1961.

[44] Image Processing and Analysis in Java ImageJ. `http://rsbweb.nih.gov/ij/`. 1.43.

[45] R. M. Pothapragada, R. A. Mirshams, and Suman Vadlakonda. Effect of pile-up in nanoindentation of micro and nano crystalline ni using fem. *Materials Research Society*, 880(BB7.9.1), 2005.

[46] Gwyddion. `http://gwyddion.net/`. 2.9.